Measurements of Strong Correlations in the Transport of Light through Strongly Scattering Materials

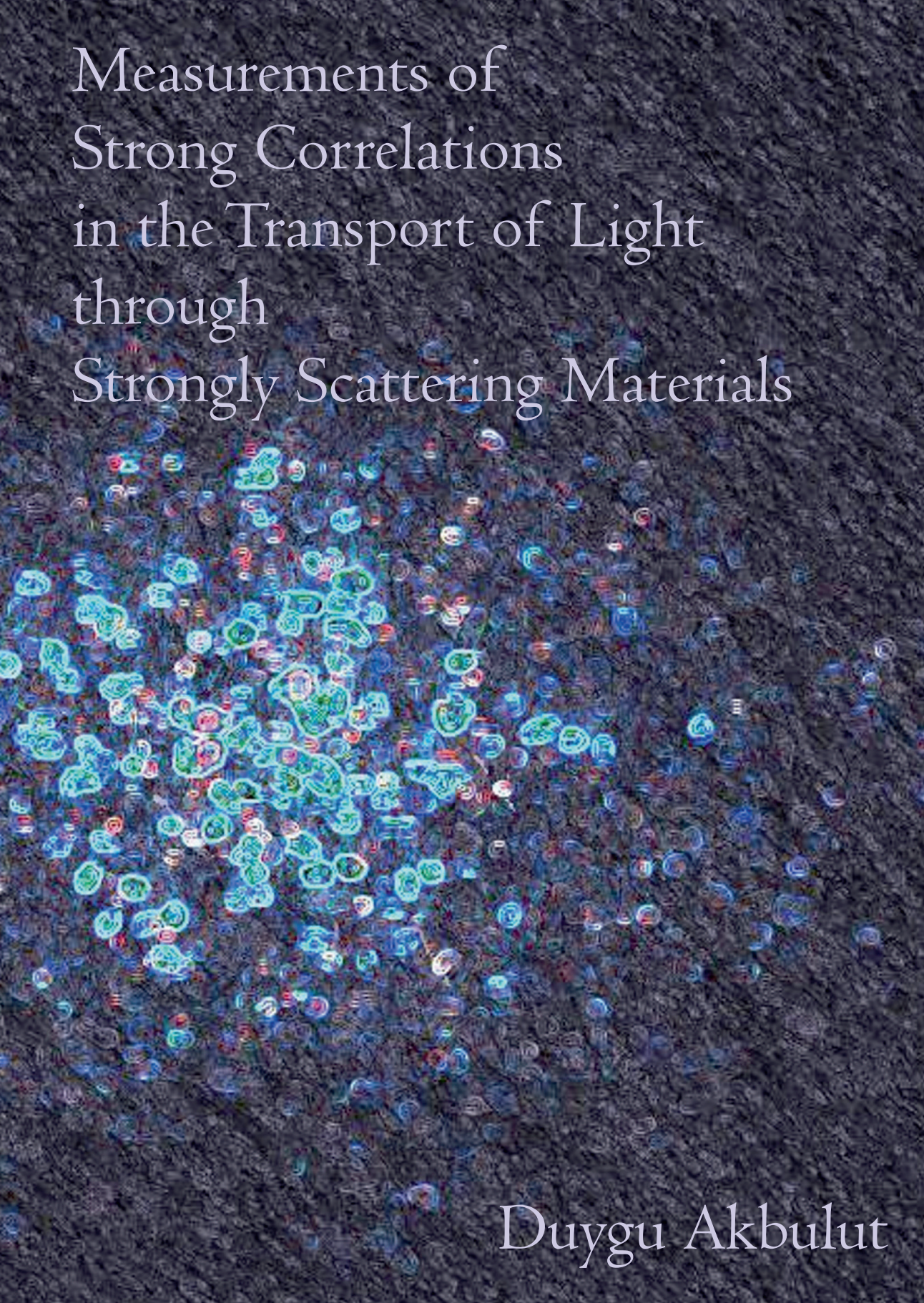

Duygu Akbulut

MEASUREMENTS of STRONG CORRELATIONS in the TRANSPORT of LIGHT through STRONGLY SCATTERING MATERIALS

Meten van sterke correlaties
in het transport van licht
door
sterk verstrooiende materialen

Promotiecommissie

Promotores	Prof. Dr. A.P. Mosk
	Prof. Dr. W.L. Vos
Overige leden	Prof. Dr. J.F. de Boer
	Prof. Dr. K.-J. Boller
	Prof. Dr. A. Lagendijk
	Dr. O.L. Muskens
	Prof. Dr. H.-J. Stöckmann

The work described in this thesis is financially supported by the stichting FOM which is financially supported by the 'Nederlandse Organisatie voor Wetenschappelijk Onderzoek' (NWO). Additional funding is provided by STW, ERC, ANP and Mesa+.

It was carried out at the
Complex Photonic Systems Group,
Department of Science and Technology
and MESA+ Institute for Nanotechnology,
University of Twente, P.O. Box 217,
7500 AE Enschede, The Netherlands.

This thesis can be downloaded from
http://www.wavefrontshaping.com

ISBN: 978-94-6108-491-0

MEASUREMENTS of STRONG CORRELATIONS in the TRANSPORT of LIGHT through STRONGLY SCATTERING MATERIALS

PROEFSCHRIFT

ter verkrijging van
de graad van doctor aan de Universiteit Twente,
op gezag van de rector magnificus,
prof. dr. H. Brinksma,
volgens besluit van het College voor Promoties
in het openbaar te verdedigen
op donderdag 5 september 2013 om 16.45 uur

door

Duygu Akbulut

geboren op 10 januari 1986
te Istanbul, Turkije

Dit proefschrift is goedgekeurd door:

Prof. Dr. A.P. Mosk en Prof. Dr. W.L. Vos

Contents

CHAPTER 1
Introduction

Light is indispensable in our lives. It is crucial for life as we know on Earth, as many biological processes such as photosynthesis depend on interaction of light with matter [1]. It is very important for us humans, as much of our perception about our environment is made possible with light, through vision [2]. We, human beings have always thrived to understand nature and modify it for our own needs. Light has not skipped our interest. Since ancient civilizations, we developed theories about light and made devices to manipulate it [3].

Most media in nature are examples of disordered media, *e.g.* milk, clouds, leaves of plants, human skin, blood. Disorder is also intrinsic in man-made structures. Despite the effort of fabricating high quality devices intended for certain functionalities, disorder often cannot be avoided and can hinder the device's performance [4–9]. Recently, many researchers are interested in making use of disorder in devices rather than trying to avoid it [10–15].

Disorder is commonly encountered in nature and technology, hence it is a very interesting subject of study in physics. Fascinating fundamental concepts of light transport through disordered media are strongly related to possible technological applications.

In this thesis, we study light transport through random photonic media. In general, we are interested in understanding and controlling light transport through such media. In particular, we focus our attention on measuring and studying the optical transmission matrices of such media. Different types of samples are studied in this thesis; what they have in common is that they scatter light multiple times, which is introduced in Section 1.1. We make an introduction to transmission matrices in Section 1.2. Finally, widely used powerful methods are described to control light transport through random photonic media in Section 1.3. In Section 1.4, we give an overview of the contents of this thesis.

1.1. Multiple scattering

Multiple scattering occurs in a medium when light that enters the medium gets scattered by more than one scatterer before exiting the medium [16–18]. The white color of milk, white paint, clouds is caused by multiple scattering by wavelength-scale particles. Moreover, the white color indicates that there is no absorption of visible light in the multiple scattering examples that are provided.

In order to decide whether there is multiple light scattering in a certain medium,

one needs to know how far the light travels before it undergoes a scattering event and the length, L of the medium. The mean distance between two scattering events is known as the "scattering mean free path" l_s [19]. So, multiple scattering occurs when $l_s < L$. In the case of isotropic scattering, the direction of the incident wave is randomized after traveling a distance l_s in a scattering medium. However, not all scattering events are isotropic, so that the direction of the incident wave may not be randomized after it traverses a distance l_s in the scattering medium. The length traversed by light, after which the initial direction is randomized is known as the transport mean free path, l_{tr}. For isotropic scattering,

$$l_{\mathrm{tr}} = l_s, \tag{1.1}$$

whereas in general for anisotropic scattering [19],

$$l_{\mathrm{tr}} = \frac{l_s}{1 - \langle \cos\theta \rangle}. \tag{1.2}$$

Here, θ is the angle between the wavevector incident to the scatterer and the wavevector of the scattered light, $\langle . \rangle$ indicates averaging over all angles, θ. If the scattering is isotropic $\langle \cos\theta \rangle = 0$. If the scattering is completely in the forward direction, $\langle \cos\theta \rangle = 1$, in which case the direction of incident light is never randomized in the medium. The transport mean free path and scattering mean free path for anisotropic scattering are depicted in Fig 1.1. The light is shown to undergo many small angle scattering events which occur on average l_s apart. In many cases, this can be viewed as equivalent to a smaller number of isotropic scattering events that are l_{tr} apart, where $l_{\mathrm{tr}} > l_s$. When $l_s \leq l_{\mathrm{tr}} < L$, light performs a random walk in the scattering medium and is well described by diffusion theory, apart from the interference effects.

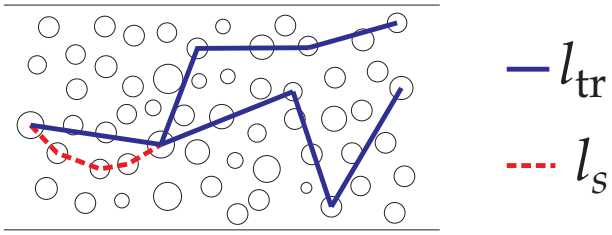

Figure 1.1.: Scattering and transport mean free path for anisotropic scattering. Blue solid line: a trajectory scattered over a large angle after each transport mean free path l_{tr}, red dashed line: a trajectory undergoing small angle scattering after each scattering mean free path, l_s.

1.2. Optical transmission matrices

The relation between fields incident on and transmitted through a random photonic medium is well-described by a transmission operator. In a mathematical

description, incident and transmitted fields are represented in certain basis sets. In turn, the relation between these idealized incident and transmitted fields is represented by a transmission matrix. Knowledge of the transmission matrix is of paramount importance in terms of applications as it allows one to manipulate the transmitted fields through a random photonic medium [20, 21].

Moreover, transmission matrices contain very interesting physics arising from energy conservation [22]. The light transport can be visualized as taking place via transmission eigenchannels of a random photonic medium. According to theory, light transport mostly takes place through a small number of open transmission eigenchannels that completely transmit light, introducing correlations between the elements of the transmission matrices [22–26]. In order to visualize these correlations, one can think of a randomly generated field incident on a random photonic medium. In a simplified picture, such a field couples to a collection of transmission eigenchannels that are either completely transmitting (open transmission eigenchannels) or completely reflecting (closed transmission eigenchannels) [26]. Light transmitted through the medium is a linear superposition of fields transmitted through the open transmission eigenchannels. When the number of open transmission eigenchannels is small, the transmitted light has a low degree of freedom as compared to the incident light, showing that the transmitted fields (likewise, the transmission matrix elements) are correlated. A simple everyday example can be given using a thick piece of paper. When we hold this paper and look at the light reflected from it, we see that it looks bright white. When we hold this paper to light, though, we see that it is dim. Hence, this paper reflects more light than it transmits. The interesting and counter-intuitive prediction of the theory is that the low transmission through paper is not due to many transmission eigenchannels with low transmission but is due to few transmission eigenchannels with high transmission.

Observing individual open transmission eigenchannels in an optical experiment was our ultimate goal when we started the study of transmission matrices. However, it turned out to be very difficult. The difficulties are arising from both experimental imperfections and the intrinsic difficulties arising from working with samples having a slab geometry, where it is physically impossible to perfectly address transmission eigenchannels.

Even though individual open transmission eigenchannels cannot be observed, we observed correlations between the fields transmitted through strongly scattering materials, which is indicative of correlations between the transmission matrix elements. Since we measure partial transmission matrices, we do not expect to reproduce the theoretical predictions made by assuming a full transmission matrix. However, our experimental results are in agreement with a newly developed analytical theory for partial transmission matrices [27].

A full transmission matrix can give complete information on light transport through a random photonic medium. Retrieving complete information from a partial transmission matrix measurement is possible, but the retrieval process is very unstable due to reduced signal to noise ratio in an actual experiment [28]. In recent work by Shi *et al.*, universal mesoscopic transport phenomena were studied in quasi-1D disordered microwave waveguides by measuring and investigating

the transmission matrices of these waveguides [29, 30]. In our experiments, we observed correlations in partial transmission matrices of 3D samples, indicating that sample information is retained in the measured matrices. We demonstrate the first ever retrieval of the scattering strength of the sample using optical transmission matrix measurements.

1.3. Control of light transport through random photonic media

Since the fields incident on and transmitted through a random photonic medium are related by the transmission operator of the medium, the transmitted field is modified if the incident field is modified. In a paper by Freund [31], it was envisioned that this principle can be used to obtain optical elements from scattering samples. However, active control of the fields incident on the scattering sample was not proposed in this paper.

Active control of transmitted fields through random photonic media is made possible by wavefront shaping, as was first demonstrated in our group at the University of Twente by Vellekoop and Mosk [32]. In the method described in Ref. [32], a single target outgoing channel is selected and its intensity is used as a feedback signal to an algorithm that modifies the phase of the fields incident on the sample. In this way, the intensity in the selected outgoing free mode is maximized by shaping the incident wavefront.

Knowledge of the *partial* transmission matrix also allows one to manipulate the light transport through disordered media. This method was first demonstrated by Popoff *et al.* [20]; part of the optical transmission matrix of a disordered sample was measured and the knowledge of the transmission matrix was used to focus light behind a disordered medium. This method has been adopted in other work to send an image through a disordered medium [33], to employ the disordered medium in order to increase the resolution of an otherwise low resolution imaging system [34] and enhance the transmission through a disordered system [35]. The studies mentioned were conducted using monochromatic light. It is possible to also measure a wavelength dependent transmission matrix and obtain optical or microwave time reversal [36]. In recent work, optics is merged with acoustics to measure a photo-acoustic transmission matrix, which can have biomedical applications [37].

Control of light transport through random photonic media has attracted a lot of attention both from a fundamental and an application-based point of view and has become a growing field [14]. Such control eventually allows for a selective coupling of light to individual open transmission eigenchannels and can enable experimental study of such channels, experimental studies in this direction are described in [35, 38]. It can provide control over absorption, emission and random lasers where there is absorption and gain inside the disordered medium [39–43]. It opens up many prospects for imaging through opaque tissue and with an extremely high resolution [12, 44, 45]. Merging control over light transport with acoustics, it is possible to increase the resolution of ultrasound imaging. With

the active control of fields incident on a disordered medium, it is possible to use the disordered medium as a reconfigurable optical element. In the recent years, several optical functionalities have been demonstrated by using disordered media, including a lens [12, 32], a polarizer [46], a dynamic waveplate [47], a spectral filter [48] and a beamsplitter [49].

1.4. Outline of this thesis

This thesis is organized as follows:

In **Chapter 2**, we introduce basic physical concepts that are widely used to study light transport through random photonic media and are also employed in the further chapters of this thesis.

In **Chapter 3**, we present a study where we focus light through a random photonic medium using binary amplitude modulation. The conventional implementation of wavefront shaping is by modulating the phase of the incident wavefront. In this chapter, we describe how to perform wavefront shaping by selectively removing a portion of light incident on the disordered medium. The method is demonstrated using both a liquid crystal amplitude and phase modulation spatial light modulator as well as using a digital micromirror device inside a commercial projector. It is the first demonstration of using a MEMS-based device for focusing light through disordered media. Moreover, by using a commercial projector for wavefront shaping we show that wavefront shaping does not *per se* require expensive equipment and in principle can easily be implemented as a tabletop student experiment.

In **Chapter 4**, we give a detailed description of the experimental and data analysis procedure for transmission matrix measurements. In this chapter, we also provide a detailed analysis of effects of noise on the transmission matrix experiments.

In **Chapter 5**, we describe transmission matrix measurements of strongly scattering random photonic GaP nanowire ensembles. The samples used in this section are among the strongest scattering materials reported for visible light. We observe correlations in the measured transmission matrices. Observation of these correlations is indicative of strong scattering of these materials and indicates that the physical information on light transport through the sample is not lost. Moreover, we describe a numerical model that we developed to interpret our findings and which reproduces the experimental results. We also used this numerical model to estimate the scattering strength of the sample under study. This is a first successful demonstration of the use of transmission matrices for retrieving optical properties of scattering media. The retrieved scattering strength is found to be consistent with the previously reported parameters.

In **Chapter 6**, we describe the transmission matrix measurements of strongly scattering random photonic media of ZnO nanoparticles in air. These samples are less strongly scattering than samples studied in Chapter 5, however, are still among the most strongly scattering materials used in the optical wavelength regime. The samples used in this chapter enable very good optical access and in

turn enable measurement of a large part of the transmission matrix. Measuring a large portion of the transmission matrix along with the strong scattering of ZnO nanoparticle medium makes it possible to observe strong correlations in the transmission matrices of these samples. In this chapter, we compare our experimental findings to numerical and analytical models and observe very good agreement.

In **Chapter 7**, we report on speckle intensity statistics of waves transmitted through random photonic media of ZnO nanoparticles in air. The samples are the same samples as used in Chapter 6. We observed deviations from Rayleigh statistics. This is a first observation of such deviations in isotropic light-scattering samples and is indicative of the strong scattering of ZnO nanoparticle layers, supporting the results of Chapter 6.

In **Chapter 8**, we provide a summary of the thesis.

Bibliography

[1] K. H. Nealson and P. G. Conrad, *Life: past, present and future*, Phil. Trans. R. Soc. Lond. B **354**, 1923 (1999). — p.3.

[2] J. Erichsen and J. Woodhouse, in *Machine vision handbook*, edited by B. Batchelor (Springer Reference (www.springerreference.com). Springer-Verlag Berlin Heidelberg, 2012. DOI: 10.1007/SpringerReference_318221, 2012). — p.3.

[3] M. Born and E. Wolf, *Principles of optics* (Cambridge University Press, 2003). — p.3.

[4] A. F. Koenderink and W. L. Vos, *Light exiting from real photonic band gap crystals is diffuse and strongly directional*, Phys. Rev. Lett. **91**, 213902 (2003). — p.3.

[5] D. K. Armani, T. J. Kippenberg, S. M. Spillane, and K. J. Vahala, *Ultra-high-Q toroid microcavity on a chip*, Nature **421**, 925 (2003). — p.3.

[6] A. F. Koenderink, A. Lagendijk, and W. L. Vos, *Optical extinction due to intrinsic structural variations of photonic crystals*, Phys. Rev. B **72**, 153102 (2005). — p.3.

[7] S. Hughes, L. Ramunno, J. F. Young, and J. E. Sipe, *Extrinsic optical scattering loss in photonic crystal waveguides: role of fabrication disorder and photon group velocity*, Phys. Rev. Lett. **94**, 033903 (2005). — p.3.

[8] M. V. Gorkunov, S. A. Gredeskul, I. V. Shadrivov, and Y. S. Kivshar, *Effect of microscopic disorder on magnetic properties of metamaterials*, Phys. Rev. E **73**, 056605 (2006). — p.3.

[9] J. Gollub, T. Hand, S. Sajuyigbe, S. Mendonca, S. Cummer, and D. R. Smith, *Characterizing the effects of disorder in metamaterial structures*, Appl. Phys. Lett. **91**, 162907 (2007). — p.3.

[10] G. Lerosey, J. de Rosny, A. Tourin, and M. Fink, *Focusing beyond the diffraction limit with far-field time reversal*, Science **315**, 1120 (2007). — p.3.

[11] L. Sapienza, H. Thyrrestrup, S. Stobbe, P. David Garcia, S. Smolka, and

P. Lodahl, *Cavity quantum electrodynamics with Anderson-localized modes*, Science **327**, 1352 (2010). — p.3.

[12] E. G. van Putten, D. Akbulut, J. Bertolotti, W. L. Vos, A. Lagendijk, and A. P. Mosk, *Scattering lens resolves sub-100 nm structures with visible light*, Phys. Rev. Lett. **106**, 193905 (2011). — p.3, 6, 7.

[13] O. Katz, E. Small, Y. Bromberg, and Y. Silberberg, *Focusing and compression of ultrashort pulses through scattering media*, Nat. Photon. **5**, 372 (2011). — p.3.

[14] A. P. Mosk, A. Lagendijk, G. Lerosey, and M. Fink, *Controlling waves in space and time for imaging and focusing in complex media*, Nat. Photon. **6**, 283 (2012). — p.3, 6.

[15] D. S. Wiersma, *Disordered photonics*, Nat. Photon. **7**, 188 (2013). — p.3.

[16] H. C. van de Hulst, *Light scattering by small particles* (Dover Publications, Inc., 1981). — p.3.

[17] C. F. Bohren and D. R. Huffman, *Absorption and scattering of light by small particles* (John Wiley and Sons, Inc., 1983). — p.3.

[18] A. Lagendijk and B. A. van Tiggelen, *Resonant multiple scattering of light*, Phys. Rep. **270**, 143 (1996). — p.3.

[19] M. C. W. van Rossum and T. M. Nieuwenhuizen, *Multiple scattering of classical waves : microscopy , mesoscopy , and diffusion*, Rev. Mod. Phys. **71**, 313 (1999). — p.4.

[20] S. M. Popoff, G. Lerosey, R. Carminati, M. Fink, A. C. Boccara, and S. Gigan, *Measuring the transmission matrix in optics: An approach to the study and control of light propagation in disordered media*, Phys. Rev. Lett. **104**, 100601 (2010). — p.5, 6.

[21] E. G. van Putten and A. P. Mosk, *The information age in optics: Measuring the transmission matrix*, Physics **3**, (2010). — p.5.

[22] C. W. J. Beenakker, *Random-matrix theory of quantum transport*, Rev. Mod. Phys. **69**, 731 (1997). — p.5.

[23] O. N. Dorokhov, *Transmission coefficient and the localization length of an electron in N bound disordered chains*, JETP Lett. **36**, 318 (1982). — p.5.

[24] O. N. Dorokhov, *On the coexistence of localized and extended electronic states in the metallic phase*, Solid State Commun. **51**, 381 (1984). — p.5.

[25] P. A. Mello, P. Pereyra, and N. Kumar, *Macroscopic approach to multichannel disordered conductors*, Ann. of Phys. **181**, 290 (1988). — p.5.

[26] J. B. Pendry, A. MacKinnon, and A. B. Pretre, *Maximal fluctuations – a new phenomenon in disordered systems*, Physica A **168**, 400 (1990). — p.5.

[27] A. Goetschy and A. D. Stone, *Filtering random matrices: The effect of imperfect channel control in multiple-scattering*, Phys. Rev. Lett. **111**, 063901 (2013). — p.5.

[28] *Private communication with Raj Rao Nadakuditi* — p.5.

[29] Z. Shi and A. Z. Genack, *Transmission eigenvalues and the bare conductance in the crossover to Anderson localization*, Phys. Rev. Lett. **108**, 043901 (2012). — p.6.

[30] Z. Shi, J. Wang, and A. Z. Genack, *Microwave "optical" conductance*, arXiv **1303.1133**, (2013). — p.6.

[31] I. Freund, *Looking through walls and around corners*, Physica A **168**, 49 (1990). — p.6.
[32] I. M. Vellekoop and A. P. Mosk, *Focusing coherent light through opaque strongly scattering media*, Opt. Lett. **32**, 2309 (2007). — p.6, 7.
[33] S. Popoff, G. Lerosey, M. Fink, A. C. Boccara, and S. Gigan, *Image transmission through an opaque material*, Nat. Commun. **1**, 1 (2010). — p.6.
[34] Y. Choi, T. D. Yang, C. Fang-Yen, P. Kang, K. J. Lee, R. R. Dasari, M. S. Feld, and W. Choi, *Overcoming the diffraction limit using multiple light scattering in a highly disordered medium*, Phys. Rev. Lett. **107**, 023902 (2011). — p.6.
[35] M. Kim, Y. Choi, C. Yoon, W. Choi, J. Kim, Q.-H. Park, and W. Choi, *Maximal energy transport through disordered media with the implementation of transmission eigenchannels*, Nat. Photon. **6**, 581 (2012). — p.6.
[36] Z. Shi, M. Davy, J. Wang, and A. Z. Genack, *Focusing through random media in space and time: a transmission matrix approach*, Opt. Lett. **38**, 2714 (2013). — p.6.
[37] T. Chaigne, O. Katz, A. C. Boccara, M. Fink, E. Bossy, and S. Gigan, *Controlling light in scattering media noninvasively using the photo-acoustic transmission-matrix*, arXiv **1305.6246**, 1 (2013). — p.6.
[38] I. M. Vellekoop and A. P. Mosk, *Universal optimal transmission of light through disordered materials*, Phys. Rev. Lett. **101**, 120601 (2008). — p.6.
[39] Y. D. Chong and A. D. Stone, *Hidden black: coherent enhancement of absorption in strongly scattering media*, Phys. Rev. Lett. **107**, 163901 (2011). — p.6.
[40] W. Wan, Y. Chong, L. Ge, H. Noh, A. D. Stone, and H. Cao, *Time-reversed lasing and interferometric control of absorption*, Science **331**, 889 (2011). — p.6.
[41] M. Leonetti and C. López, *Active subnanometer spectral control of a random laser*, Appl. Phys. Lett. **102**, 071105 (2013). — p.6.
[42] T. Hisch, M. Liertzer, D. Pogany, F. Mintert, and S. Rotter, *Pump-controlled directional light emission from random lasers*, arXiv **1303.5292**, 1 (2013). — p.6.
[43] N. Bachelard, S. Gigan, X. Noblin, and P. Sebbah, *Turning a random laser into a tunable singlemode laser by active pump shaping*, arXiv **1303.1398**, 1 (2013). — p.6.
[44] E. G. van Putten, *Disorder-enhanced imaging with spatially controlled light*, Ph.D. thesis, University of Twente, 2011. — p.6.
[45] J. Bertolotti, E. G. van Putten, C. Blum, A. Lagendijk, W. L. Vos, and A. P. Mosk, *Non-invasive imaging through opaque scattering layers*, Nature **491**, 232 (2012). — p.6.
[46] Y. Guan, O. Katz, E. Small, J. Zhou, and Y. Silberberg, *Polarization control of multiply-scattered light through random media by wavefront shaping*, Opt. Lett. **37**, 4663 (2012). — p.7.
[47] J.-H. Park, C. Park, H. Yu, Y.-H. Cho, and Y. K. Park, *Dynamic active wave plate using random nanoparticles*, Opt. Express **20**, 17010 (2012). — p.7.
[48] J.-H. Park, C. Park, H. Yu, Y.-H. Cho, and Y. K. Park, *Active spectral*

filtering through turbid media, Opt. Lett. **37**, 3261 (2012). — p.7.
[49] S. R. Huisman, *Light control with ordered and disordered nanophotonics*, Ph.D. thesis, University of Twente, 2013. — p.7.

CHAPTER 2
Concepts

In this chapter, we review the main concepts of light transport through disordered media. The aim is to provide an understanding of key concepts that are used throughout the thesis. Diffusion theory is described in Section 2.1. Scattering and transmission matrices and the transmission eigenchannels are introduced in Section 2.2. Random matrix theory as an approach to light transport through disordered media is described in Section 2.3. The intensity statistics of the speckle is described in Section 2.4. In Section 2.5, we describe the concept of photonic strength and comment on its relation to observing correlations in a transmission matrix measurement.

2.1. Diffusion

When interference effects are neglected, diffusion theory provides a good description for light propagation in disordered photonic media for the case where $\lambda \ll l_{\mathrm{tr}} \ll L$. The diffuse intensity is described by the diffusion equation [1]

$$\frac{\partial}{\partial t} I(\mathbf{r}, t) = D \nabla^2 I(\mathbf{r}, t). \tag{2.1}$$

Here, $I(\mathbf{r}, t)$ is the diffuse intensity and D is the diffusion constant. When the system is in steady state, the time derivative vanishes and the diffusion equation becomes Laplace's equation

$$D \nabla^2 I(\mathbf{r}) = 0. \tag{2.2}$$

We can also include a source function to get Poisson's equation

$$D \nabla^2 I(\mathbf{r}) + S(\mathbf{r}) = 0, \tag{2.3}$$

where $S(\mathbf{r})$ is the source function. Equation 2.3 can be solved for a delta function source

$$D \nabla^2 g(\mathbf{r}, \mathbf{r_1}) = -\delta(\mathbf{r} - \mathbf{r_1}). \tag{2.4}$$

where $g(\mathbf{r}, \mathbf{r_1})$ is the Green's function. Physically, it represents the diffuse intensity at position $\mathbf{r}$ caused by a point source at position $\mathbf{r_1}$. This solution can be generalized to an arbitrary source using the superposition principle, yielding [2]

$$I(\mathbf{r}) = \int g(\mathbf{r}, \mathbf{r_1}) S(\mathbf{r_1}) d\mathrm{r}_1, \tag{2.5}$$

The integral is taken over all space.

2.1.1. Slab geometry

A sample with a slab geometry extends effectively to infinity in two transversal dimensions x and y, and is finite in the longitudinal z-direction. The samples that are studied in this thesis have a slab geometry. Diffusion in a slab geometry has been widely studied [1, 3–5], and here we recapitulate the essential physics.

In case of a plane wave that is at normal incidence on a sample with a slab geometry, the diffusion equation along the z-direction is

$$D\frac{\partial^2 I(z)}{\partial z^2} + S(z) = 0. \tag{2.6}$$

The diffuse source, $S(z)$ can be taken as a planar source located at an injection depth, $z_{\text{inj}} = l_{\text{tr}}$ away from the boundary of the slab [3, 6], so that

$$D\frac{\partial^2 I(z)}{\partial z^2} + \delta(z - z_{\text{inj}}) = 0. \tag{2.7}$$

In order to obtain the solution to the diffusion equation 2.7, we have to impose boundary conditions. The diffuse source is assumed to be located inside the sample. In this case, at the front and rear surfaces of the sample, incoming fluxes are only due to reflections from the interface [7, 8]. Therefore, the generally adopted boundary conditions are [8]

$$\begin{aligned} J_+ &= \overline{R} J_- \qquad \text{at z = 0} \\ J_- &= \overline{R} J_+ \qquad \text{at z = L,} \end{aligned} \tag{2.8}$$

with J_- and J_+ the flux in $-z$ and $+z$ directions, respectively. $z = 0$ and $z = L$ are the positions of the front and rear surfaces of the sample and $\overline{R}$ is a mean reflection coefficient, defined as [8]

$$\overline{R} = \frac{3C_2 + 2C_1}{3C_2 - 2C_1 + 2}, \tag{2.9}$$

with

$$C_1 \equiv \int_0^{\pi/2} R(\theta)\sin(\theta)\cos(\theta)d\theta, \tag{2.10}$$

and

$$C_2 \equiv \int_{-\pi/2}^{0} R(\theta)\sin(\theta)\cos^2(\theta)d\theta. \tag{2.11}$$

Here, $R(\theta)$ is an angle dependent reflection coefficient,

$$R(\theta) = \frac{R_\perp(\theta) + R_\parallel(\theta)}{2}, \tag{2.12}$$

and $R_\perp(\theta)$, $R_\parallel(\theta)$ are the Fresnel reflection coefficients for light perpendicular and parallel polarized to the plane of incidence, respectively [8, 9].

Using the boundary conditions in Eq. 2.8, the diffuse intensity is found to extrapolate to zero *outside* of the sample, at a certain distance away from the

interface. This distance is known as the extrapolation length z_e. In order to calculate the extrapolation length, one needs to take into account the reflections occurring at the interface of the sample due to the refractive index mismatch between the sample and the surroundings [7, 8]. The extrapolation length z_e is equal to

$$z_e = \frac{2}{3} l_{\mathrm{tr}} \frac{1+\overline{R}}{1-\overline{R}}. \tag{2.13}$$

In the case of a planar source at position z_{inj}, the solution of the diffusion equation is [1, 5, 10],

$$I(z) = \frac{1}{D} \begin{cases} \dfrac{L - z_{\mathrm{inj}} + z_{e2}}{L + z_{e1} + z_{e2}} (z + z_{e1}) & , 0 \le z \le z_{\mathrm{inj}} \\ \dfrac{z_{\mathrm{inj}} + z_{e1}}{L + z_{e1} + z_{e2}} (L + z_{e2} - z) & , z_{\mathrm{inj}} \le z \le L, \end{cases} \tag{2.14}$$

with z_{e1} and z_{e2} are the extrapolation lengths on the front and rear sides of the sample, respectively. The diffuse intensity distribution is shown in Fig. 2.1. The diffuse intensity is maximum at the location of the source $z = z_{\mathrm{inj}}$ and extrapolates linearly to zero at a distance of extrapolation length away from the sample.

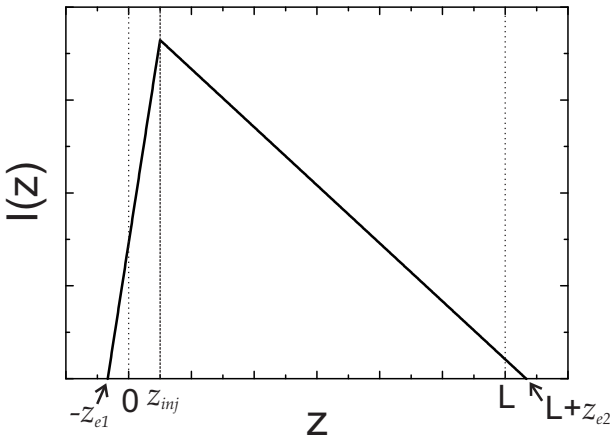

Figure 2.1.: Intensity as a function of position in a slab. The planar diffuse source is at z_{inj}. Physical boundaries of the sample are at $z = 0$ and $z = L$.

The total transmission is the transmitted flux normalized by the incident flux and is given by [10, 11]

$$\langle T \rangle = \frac{z_{\mathrm{inj}} + z_{e1}}{L + z_{e1} + z_{e2}}. \tag{2.15}$$

When a plane wave is normally incident on a slab, $z_{\mathrm{inj}} = l_{\mathrm{tr}}$. In our experiments, we focus the incident light on the front surface of the sample. In this case, many plane waves are incident on the sample, each at an angle θ with the surface

normal [12] and carrying an equal flux normal to the front surface of the sample. Each plane wave travels a transport mean free path l_{tr} in the medium before it becomes diffuse, this corresponds to a distance $l_{\mathrm{tr}}\cos(\theta)$ from the front surface of the sample, where θ is the angle between the propagation direction of the plane wave and the normal to the front surface of the sample. Following [3] we find an effective diffuse source, located at z_{inj} from the front surface of the sample. In the case that θ varies between 0 and θ_{max}, the injection depth is equal to

$$z_{\mathrm{inj}} = \frac{\int_0^{2\pi}\int_0^{\theta_{\mathrm{max}}} l_{\mathrm{tr}}\cos(\theta) I\cos(\theta)\sin(\theta)d\theta d\phi}{\int_0^{2\pi}\int_0^{\theta_{\mathrm{max}}} I\cos(\theta)\sin(\theta)d\theta d\phi} \tag{2.16}$$

For $\theta_{\mathrm{max}} = \pi/2$, $z_{\mathrm{inj}} = \frac{2}{3}l_{\mathrm{tr}}$ is found. In an optical experiment, the range of angles of incidence is limited and θ_{max} is determined by the NA of the objective. In this thesis, NA=0.95 is used in the transmission matrix experiments of ZnO nanoparticles in air, giving θ_{max}=1.25 radians. This angle is even smaller inside the sample due to refraction. The sample consists of two different materials with different refractive indices. In order to find the refractive index of such a sample, it can be modeled as an effective medium with an effective refractive index, n_{eff}, which is a function of the refractive indices of the constituent media and their filling fraction [13]. Modeling the scattering sample by an effective medium is a good approximation when the sample consists of sub-wavelength particles. The effective refractive index, n_{eff}, of a medium consisting of ZnO nanoparticles in air is roughly 1.4 [14, 15], giving rise to θ_{max}=0.75 radians in the sample, and $z_{\mathrm{inj}} = 0.87l_{\mathrm{tr}}$. In the case of transmission matrix experiments performed with the random photonic GaP nanowires we used an objective with NA=0.6. Assuming $n_{\mathrm{eff}} = 2.25$, θ_{max} is found to be 0.27 radians in the sample. In this case, $z_{\mathrm{inj}} = 0.97l_{\mathrm{tr}}$ is obtained, which is hardly different from the usual $z_{\mathrm{inj}} = l_{\mathrm{tr}}$.

2.2. Scattering and transmission matrix

Light transport through scattering media can be modeled using a scattering matrix S that relates fields incident on the sample to the outgoing fields [16]

$$\begin{pmatrix} E^-_{\mathrm{out}} \\ E^+_{\mathrm{out}} \end{pmatrix} = S \begin{pmatrix} E^+_{\mathrm{in}} \\ E^-_{\mathrm{in}} \end{pmatrix}, \tag{2.17}$$

with S the scattering matrix, E^+_{in} and E^-_{in} the fields in free space incident on the sample from left and right, respectively and E^-_{out} and E^+_{out} the outgoing fields in free space on the left and right sides, respectively. The scheme of incident and transmitted fields is shown for a confined, scattering sample in Fig. 2.2. The fields are normalized so that the power they carry is given by their modulus square. Due to the conservation of energy, the S matrix is unitary and due to reciprocity, it is symmetric.

Without the choice of a basis, the S matrix is a linear operator. It is represented as a matrix when a basis is chosen. In order to represent the S matrix of a

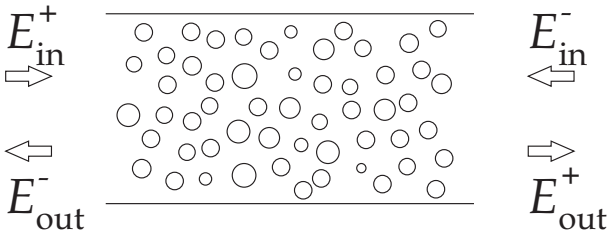

Figure 2.2.: E^+_{in}: field incident on the sample from the left, E^+_{out}: field transmitted through the sample on the right, E^-_{in}: field incident on the sample from the right. E^-_{out}: field transmitted through the sample on the left.

waveguide, one may choose the basis as the TE and TM modes of a waveguide without scatterers. To represent the S matrix for a slab, one can choose the basis as diffraction limited spots on the surface of the sample or plane waves with different angles of incidence on the sample [17]. Unlike the situation in a waveguide, for a slab there is no basis of propagating modes that is both complete and orthogonal. The S matrix is equal to

$$S = \begin{pmatrix} R^{-+} & T^{--} \\ T^{++} & R^{+-} \end{pmatrix}, \tag{2.18}$$

with R^{-+} the reflection matrix on the left side of the sample, R^{+-} the reflection matrix on the right side of the sample, T^{--} the transmission matrix from right to the left and T^{++} the transmission matrix from left to right. In this thesis, only T^{++} is considered. From this point on we represent T^{++} as T and call it the transmission matrix of our sample. We have

$$E^+_{\text{out}} = TE^+_{\text{in}}. \tag{2.19}$$

Using singular value decomposition, the transmission matrix T can be written as a product of three matrices [18]

$$T = U\mathcal{T}V^\dagger. \tag{2.20}$$

Here, the matrices U and $V^\dagger$ are unitary matrices with complex elements and the matrix $\mathcal{T}$ is a diagonal matrix with real, positive elements. The matrix $V^\dagger$ performs a basis transformation between the free modes incident on the sample and the transmission eigenchannels inside the sample. The elements on the diagonal of matrix $\mathcal{T}$ are the singular values, τ_0 of the transmission matrix and represent the eigenchannel transmission coefficients.[1] The distribution of the eigenchannel transmission coefficients is described using random matrix theory. The matrix U performs the basis transformation between the transmission eigenchannels and the outgoing free modes from the sample. Columns of the matrices U and V are the left and right singular vectors of the matrix T.

[1] The singular values having the DMPK distribution are denoted τ_0 as opposed to the notation τ used for rest of the singular values in this thesis. τ represents singular values that are normalized so that $\sqrt{\langle\tau^2\rangle} = 1$.

2.3. Random matrix theory

Random matrix theory (RMT) enables the study of complex structures using a statistical approach. A physical system is modeled using a large and random matrix, where certain probability distributions of the matrix elements and eigenvalues are assumed due to physical symmetries in the system under study.

The history of RMT is described in detail in many reviews [16, 19–21]. Here, we provide a short summary. Random matrix theories were first introduced in mathematical statistics by Wishart in 1928 [22]. RMT started to be used in physics in 1950s and 1960s and the initial motivation was to explain the spacings between the energy levels of slow neutron resonances in nuclear reactions [23–28]. Since then, RMT has been applied to various areas in physics, *e.g.* level statistics of small metal particles, quantum chaos, quantum field theory and wave transport through disordered media [16, 19, 21]. Since 1980s, random matrix theory has been applied to classical and quantum optics [29]. The systems that have been studied experimentally include chaotic cavities [30–34] and disordered media [17, 35, 36].

The distribution of the eigenchannel transmission coefficients through disordered media is described using random matrix theory. This distribution is known as the Dorokhov-Mello-Pereyra-Kumar (DMPK) distribution and its probability density is expressed as [16, 37–39]

$$P(\tau_0^2) = \langle \tau_0^2 \rangle \frac{1}{2\tau_0^2\sqrt{1-\tau_0^2}}. \tag{2.21}$$

Here, $\langle \tau_0^2 \rangle \approx l/L$ is the total transmission through the sample. It is equal to $\langle T \rangle$ given by Eq. 2.15.

The probability density function of the eigenchannel intensity transmission coefficients is shown in Fig. 2.3. This function has two divergencies: at 0 and 1. Since the divergency at 1 is integrable, there is a finite probability of finding transmission eigenchannels close to unity transmission. The divergency at 0 is not integrable, however, the distribution does not start from 0 but it starts from a minimum transmission coefficient $\tau_0^2 \approx \cosh^{-2}(L/l)$. There are a few transmission eigenchannels with transmission coefficients close to unity. They are known as open eigenchannels and the transport mainly takes place via these eigenchannels. Most of the transmission eigenchannels have very low transmission coefficients. They are mainly reflecting and are known as the closed eigenchannels. The probability of having transmission eigenchannels with intermediate transmission coefficients is relatively small.

In order to help visualize the correlations induced by the distribution of eigenchannel transmission coefficients, we present a cartoon in Fig. 2.4. We approximate the transmission eigenchannels to be either completely transmitting (open transmission eigenchannels) or completely reflecting (closed transmission eigenchannels) [40]. In Fig. 2.4, open eigenchannels are represented as simple tubes with unity transmission. The windows placed before and after the tubes indicate the matrices U and V that perform the mapping between the bases of incident and transmitted fields and the transmission eigenchannels of the sample. Each

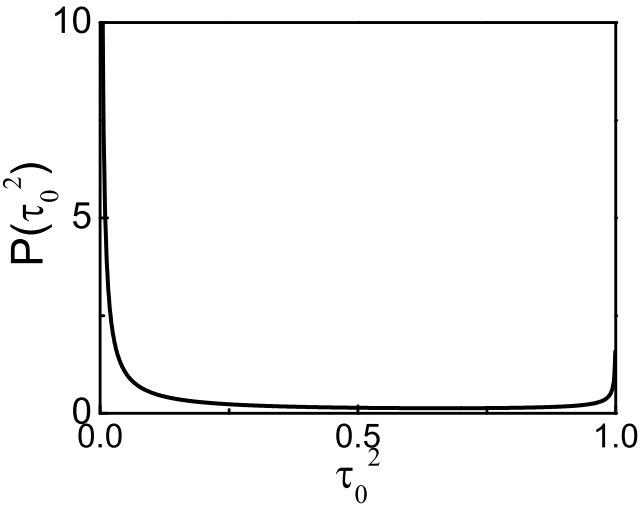

Figure 2.3.: Probability density function of τ_0^2 as obtained from DMPK theory.

speckle pattern, $c_k\phi_k$ on the right side of the sample represents the field transmitted through the k^{th} open eigenchannel. Each ϕ_k is determined by the k^{th} column of the matrix U and each complex number c_k is determined by the k^{th} column of the matrix V along with the incident field E_{in}. In Fig. 2.4 (a) a sample with a single open channel is shown. In this case, the transmitted field $E_{\text{out}} = c_1\phi_1$, independent of the field incident on the sample. On the other hand, if a sample has multiple (N) open transmission eigenchannels, as shown in Fig. 2.4 (b) the transmitted fields will be linear superpositions of N independent speckle fields, $E_{\text{out}} = c_1\phi_1 + c_2\phi_2 + ... + c_N\phi_N$. Whatever field is incident on the sample, the transmitted field can only be a superposition of the fields transmitted through relatively few open eigenchannels.

The cartoon in Fig. 2.4 is helpful for a visualization of the correlations introduced to the transmitted fields by DMPK distribution. A more accurate and detailed description of DMPK theory can be found in the review by Carlo Beenakker [16]. The DMPK theory was originally developed for samples with a waveguide geometry that are confined in the transversal dimensions. In slab samples, the transmission eigenchannels are not well-defined as in the case of waveguide geometry samples. However, the theory by Nazarov [41] and the experimental results of Vellekoop and Mosk [17] indicate that the DMPK theory also applies to slab geometry samples.

A limiting case in random matrix theory is the case of complete absence of correlations. For uncorrelated random matrices, one expects to find the singular values distributed with a probability density known as the Marcenko-Pastur law [42]. This distribution is the limiting singular value distribution when $N \to \infty$ of a γN by N matrix with independent and identically distributed elements and is

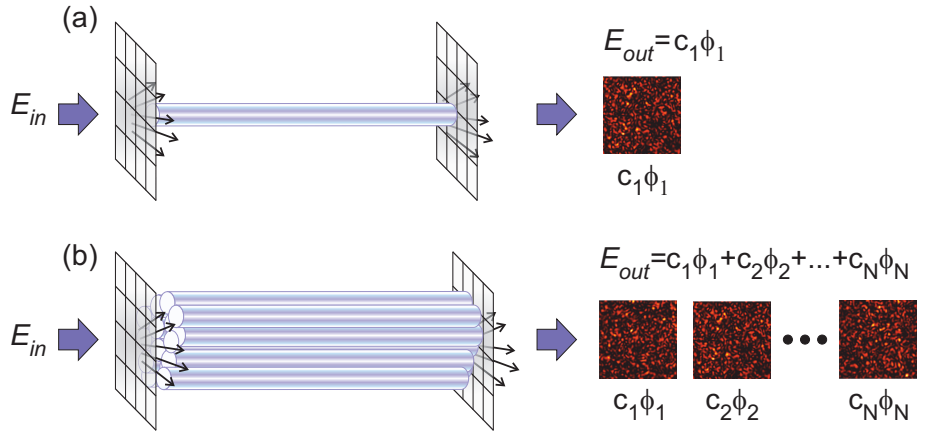

Figure 2.4.: Cartoon of (a) a sample with a single open channel, (b) a sample with N open channels. E_{in}: incident field, E_{out}: transmitted field, $c_k\phi_k$: field transmitted through k^{th} open transmission eigenchannel, tubes: open transmission eigenchannels, tiled windows: mapping between the incident and transmitted fields and the transmission eigenchannels of the sample. Speckle patterns: Orthogonal fields transmitted through the sample.

expressed as [42, 43]

$$P(\tau) = \frac{\gamma\sqrt{\tau^2 - \tau_{\text{min}}^2}\sqrt{\tau_{\text{max}}^2 - \tau^2}}{\pi\tau}, \tag{2.22}$$

with

$$\tau_{\text{min}} = 1 - \sqrt{\frac{1}{\gamma}}, \tag{2.23}$$

and

$$\tau_{\text{max}} = 1 + \sqrt{\frac{1}{\gamma}}. \tag{2.24}$$

Here, τ_{min} is the minimum singular value, τ_{max} is the maximum singular value and γ is the aspect ratio, *i.e.*, ratio of the number of rows to the number of columns of the random uncorrelated matrix. Minimum and maximum singular values as well as the shape of the distribution are highly dependent on γ. $P(\tau)$ versus τ using $\gamma = 1, 2, 4$ and 20 are shown in Fig. 2.5. In the case of $\gamma = 1$, the distribution is also known as the "quarter circle law", as with appropriate scaling it has the shape of a quarter circle. As γ increases, the singular value spectrum becomes narrower and more peaked. In the case when $\gamma \to \infty$, the spectrum becomes a delta function centered at 1.

The Marcenko-Pastur distribution is observed in an experiment when a very small portion of the transmission matrix is measured so that no correlations can be observed. In order to observe the DMPK distribution experimentally, one needs to measure the complete transmission matrix, which is not possible due to experimental limitations. Recently, the intermediate case of measuring a

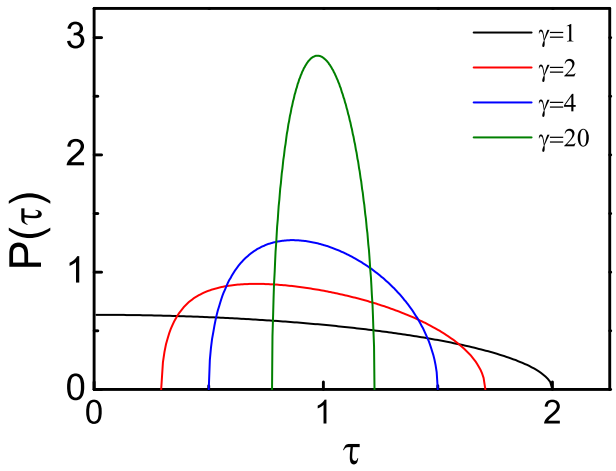

Figure 2.5.: Probability density function of τ as obtained from Marcenko-Pastur theory.

partial transmission matrix, large enough so that its singular value distributions show deviations from Marcenko-Pastur theory, but small enough so that the DMPK distribution is not observed has gathered a lot of attention since many groups around the world have started to measure partial transmission matrices. This intermediate case has recently been studied theoretically by Goetschy and Stone [43].

2.4. Speckle statistics

Temporally coherent light transmitted through a disordered medium displays a speckle pattern consisting of bright and dark regions distributed randomly throughout the field of view. A speckle pattern in transmission is the linear superposition of fields transmitted through the open transmission eigenchannels.

The intensity in the speckle pattern has a certain distribution. This distribution can be deduced by considering the addition of many fields. If these fields are assumed to be independent of each other, the distribution of real and imaginary parts of each individual speckle is Gaussian due to the central limit theorem and the intensity distribution of the speckle has Rayleigh statistics [44]

$$P(I) = \begin{cases} \frac{1}{\langle I \rangle} e^{\frac{-I}{\langle I \rangle}}, & I \geq 0 \\ 0 & \text{otherwise.} \end{cases} \tag{2.25}$$

However, fields transmitted through a disordered medium are not independent. There is a subtle correlation between these fields as they are generated by a small

number of open transmission eigenchannels. These correlations show up in the intensity statistics of the speckle as a deviation from Rayleigh statistics [45–47]. The distribution of the speckle intensity including the correction for correlations in the transmission matrix is equal to [47]

$$P\left(\frac{I}{\langle I\rangle}\right) = e^{\left(\frac{-I}{\langle I\rangle}\right)}\left\{1+\frac{1}{3g}\left[\left(\frac{I}{\langle I\rangle}\right)^2 - 4\left(\frac{I}{\langle I\rangle}\right)+2\right]\right\}. \tag{2.26}$$

Here, g is the dimensionless conductance and in a waveguide geometry it is given by [1]

$$g = \sum_{a,b} T_{ab}, \tag{2.27}$$

with T_{ab} the flux transmission coefficient from incident channel a to outgoing channel b. When g is very large, the distribution given in Eq. 2.26 reduces to the Rayleigh distribution.

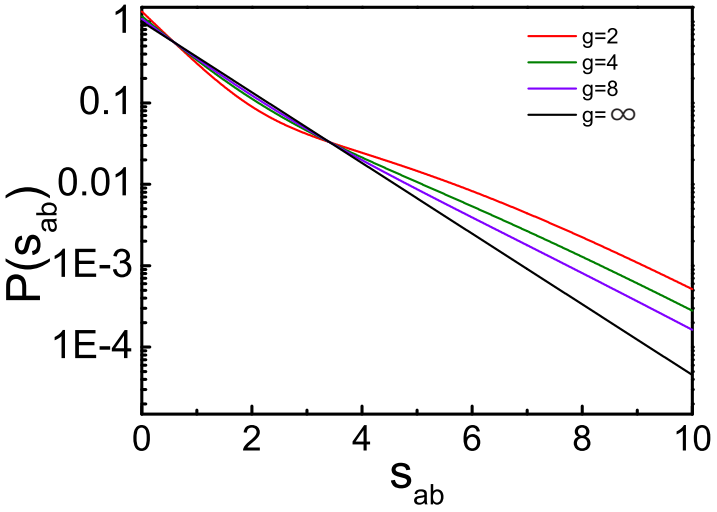

Figure 2.6.: Distribution of the normalized speckle intensity, $s_{ab} = T_{ab}/\langle T_{ab}\rangle = I/\langle I\rangle$ from [47].

In Fig. 2.6, the normalized intensity distribution of speckle as obtained from Eq. 2.26 is shown for $g = 2, 4, 8$ and ∞. The case of $g = \infty$ is equivalent to Rayleigh statistics, showing an exponentially decreasing probability for the intensity speckle. As g is decreased, the distributions of the speckle intensity deviate from Rayleigh statistics. The deviation from the Rayleigh statistics is more prominent for small g as compared to large g. In other words, when there are few open channels in the system, it is easier to observe deviations from Rayleigh statistics.

2.5. Photonic strength

The photonic strength S is a measure to describe how strongly light interacts with a complex photonic medium. For very high S photonic bandgap behaviour is expected to occur in periodic media and Anderson localization is expected to occur in random photonic media [48].

The photonic strength S is defined as the ratio of the polarizability α of an average scatterer in a complex medium to the average volume per scatterer V [48–50]

$$S = \frac{4\pi\alpha}{V}. \tag{2.28}$$

For periodic media, the photonic strength can be rewritten as [48, 50]

$$S = \frac{|\Delta\epsilon|}{\bar{\epsilon}}|f(\Delta\mathbf{k})|, \tag{2.29}$$

where $\Delta\epsilon$ is the difference in the dielectric constant, $\epsilon_2 - \epsilon_1$ of the constituent materials in the complex medium, $\bar{\epsilon}$ is the volume-averaged dielectric constant, and $f(\Delta\mathbf{k})$ is the medium's structure factor evaluated at a dominant scattering vector $\Delta\mathbf{k}$. This expression illustrates that a high dielectric contrast is favorable for strongly photonic media as well as a low average dielectric constant (or average refractive index).

For random photonic media, the photonic strength is [51]

$$S = \frac{1}{kl_{\mathrm{tr}}}, \tag{2.30}$$

where k is the wavevector of light in the medium and l_{tr} is the transport mean free path. Eq. 2.30 holds for the diffusive regime.

The photonic strength for the samples used in this thesis are in the range $0.13 < S < 0.27$ for random photonic GaP nanowire ensemble, calculated using previously reported l_{tr} [52] along with estimated effective refractive index n_{eff} values and $0.08 < S < 0.16$ for random photonic ZnO nanoparticle medium, calculated from previously reported material parameters l_{tr} and n_{eff} [14]. Whereas there is not a clearly defined threshold above which we can call a sample strongly scattering, $S > 0.2$ is considered to be a very high photonic strength, indicating very strong scattering. The photonic strengths calculated for our samples indicate that they are in this range and hence strongly scattering.

To relate the photonic strength S to the correlations in the transmission matrix measurements, we now make a simple derivation. We estimate the number of open transmission eigenchannels in a medium as

$$N_{\mathrm{open}} = \frac{2\pi A n_{\mathrm{eff}}^2}{\lambda^2}\frac{l_{\mathrm{tr}}}{L}, \tag{2.31}$$

with L the thickness of the sample and A the area over which the transmission matrix is measured. We write the number of transmission eigenchannels that can ideally be excited using a numerical aperture NA as N_{in}

$$N_{\mathrm{in}} = \frac{2\pi A(\mathrm{NA})^2}{\lambda^2}. \tag{2.32}$$

A is the probed area on the sample. In order to observe correlations in the transmission matrices, we need $N_{\text{open}} < N_{\text{in}}$. Rearranging the terms, we get the condition for observing correlations in the transmission matrix as

$$S > \frac{\lambda n_{\text{eff}}}{L 2\pi (\text{NA})^2}. \tag{2.33}$$

We see that the condition for observing correlations depend on material properties l_{tr} and n_{eff} of the sample as well as the thickness of the sample and the NA used in an experiment. This calculation is made assuming a waveguide geometry of the sample and ignoring diffuse broadening. In this case, L can be made arbitrarily large to observe correlations in a transmission matrix even for low S. If we include diffuse broadening,

$$S > \frac{\widetilde{A} \lambda n_{\text{eff}}}{A L 2\pi (\text{NA})^2} \tag{2.34}$$

is found, assuming an effective area $\widetilde{A}$ of the sample. Its width is the algebraic average of the widths of probed area and the area that the light diffuses to. It is again seen that the experimental conditions and the sample geometry plays an important role in observing correlations in a transmission matrix measurement. A very important conclusion drawn from Eqs. 2.33 and 2.34 is that for large S, correlations in a transmission matrix can be observed in an experiment with less strict requirements on the geometry.

Bibliography

[1] M. C. W. van Rossum and T. M. Nieuwenhuizen, *Multiple scattering of classical waves : microscopy , mesoscopy , and diffusion*, Rev. Mod. Phys. **71**, 313 (1999). — p.13, 14, 15, 22.

[2] G. B. Arfken and H. J. Weber, *Mathematical methods for physicists* (Elsevier Academic Press, 2005). — p.13.

[3] J. F. de Boer, *Optical fluctuations on the transmission and reflection of mesoscopic systems*, Ph.D. thesis, Universiteit van Amsterdam, 1995. — p.14, 16.

[4] A. Ishimaru, *Wave propagation and scattering in random media* (IEEE Press and Oxford University Press, 1997). — p.14.

[5] E. Akkermans and G. Montambaux, *Mesoscopic physics of electrons and photons* (Cambridge University Press, 2007). — p.14, 15.

[6] E. Akkermans, P. E. Wolf, and R. Maynard, *Coherent backscattering of light in disordered media: Analysis of the peak line shape*, Phys. Rev. Lett. **56**, 1471 (1986). — p.14.

[7] A. Lagendijk, R. Vreeker, and P. de Vries, *Influence of internal reflection on diffusive transport in strongly scattering media*, Phys. Lett. A **136**, 81 (1989). — p.14, 15.

[8] J. Zhu, D. Pine, and D. Weitz, *Internal reflection of diffusive light in random media*, Phys. Rev. A **44**, 3948 (1991). — p.14, 15.

[9] G. R. Fowles, *Introduction to modern optics* (Dover Publications, Inc., 1989). — p.14.
[10] B. P. J. Bret, *Multiple light scattering in porous gallium phosphide*, Ph.D. thesis, University of Twente, 2005. — p.15.
[11] J. Gómez Rivas, R. Sprik, C. M. Soukoulis, K. Busch, and A. Lagendijk, *Optical transmission through strong scattering and highly polydisperse media*, Europhys. Lett. **48**, 22 (1999). — p.15.
[12] J. H. Li, A. A. Lisyansky, T. D. Cheung, D. Livdan, and A. Z. Genack, *Transmission and surface intensity profiles in random media*, Europhys. Lett. **22**, 675 (1993). — p.16.
[13] C. F. Bohren and D. R. Huffman, *Absorption and scattering of light by small particles* (John Wiley and Sons, Inc., 1983). — p.16.
[14] I. M. Vellekoop, E. G. van Putten, A. Lagendijk, and A. P. Mosk, *Demixing light paths inside disordered metamaterials*, Opt. Express **16**, 67 (2008). — p.16, 23.
[15] E. G. van Putten, *Disorder-enhanced imaging with spatially controlled light*, Ph.D. thesis, University of Twente, 2011. — p.16.
[16] C. W. J. Beenakker, *Random-matrix theory of quantum transport*, Rev. Mod. Phys. **69**, 731 (1997). — p.16, 18, 19.
[17] I. M. Vellekoop and A. P. Mosk, *Universal optimal transmission of light through disordered materials*, Phys. Rev. Lett. **101**, 120601 (2008). — p.17, 18, 19.
[18] W. Press, S. Teukolsky, W. Vetterling, and B. Flannery, *Numerical recipes the art of scientific computing* (Cambridge University Press, 2007). — p.17.
[19] P. J. Forrester, N. C. Snaith, and J. J. M. Verbaarschot, *Developments in random matrix theory*, J. Phys. A: Math. Gen. **36**, R1 (2003). — p.18.
[20] M. L. Mehta, *Random matrices* (Elsevier Academic Press online book, 2004). — p.18.
[21] T. Guhr, A. Müller-Groeling, and H. A. Weidenmüller, *Random matrix theories in quantum physics: Common concepts*, Phys. Rept. **299**, 189 (1998). — p.18.
[22] J. Wishart, *Generalized product moment distribution in samples*, Biometrika A **20**, 32 (1928). — p.18.
[23] E. P. Wigner, *On the statistical distribution of the widths and spacings of nuclear resonance levels*, Proc. Camb. Phil. Soc. **47**, 790 (1951). — p.18.
[24] M. L. Mehta, *On the statistical properties of level spacings in nuclear spectra*, Nucl. Phys. **18**, 395 (1960). — p.18.
[25] F. J. Dyson, *A brownian motion model for the eigenvalues of a random matrix*, J. Math. Phys. **3**, 1191 (1962). — p.18.
[26] F. J. Dyson, *Statistical theory of the energy levels of complex systems 1*, J. Math. Phys. **3**, 140 (1962). — p.18.
[27] F. J. Dyson, *Statistical theory of the energy levels of complex systems, 2*, J. Math. Phys. **3**, 157 (1962). — p.18.
[28] F. J. Dyson, *Statistical theory of the energy levels of complex systems, 3*, J. Math. Phys. **3**, 166 (1962). — p.18.
[29] C. W. J. Beenakker, *Applications of random matrix theory to condensed*

matter and optical physics, arXiv **0904.1432**, 1 (2009). — p.18.

[30] P. So, S. M. Anlage, E. Ott, and R. N. Oerter, *Wave chaos experiments with and witwith time reversal symmetry: GUE and GOE statistics*, Phys. Rev. Lett. **74**, 2662 (1995). — p.18.

[31] R. A. Méndez-Sánchez, U. Kuhl, M. Barth, C. H. Lewenkopf, and H.-J. Stöckmann, *Distribution of reflection coefficients in absorbing chaotic microwave cavities*, Phys. Rev. Lett. **91**, 174102 (2003). — p.18.

[32] S. Hemmady, X. Zheng, T. M. Antonsen Jr., E. Ott, and S. M. Anlage, *Universal statistics of the scattering coefficient of chaotic microwave cavities*, Phys. Rev. E **71**, 056215 (2005). — p.18.

[33] U. Kuhl, M. Martínez-Mares, R. A. Méndez-Sánchez, and H.-J. Stöckmann, *Direct processes in chaotic microwave cavities in the presence of absorption*, Phys. Rev. Lett. **94**, 144101 (2005). — p.18.

[34] U. Kuhl, H.-J. Stöckmann, and R. Weaver, *Classical wave experiments on chaotic scattering*, J. Phys. A: Math. Gen. **38**, 10433 (2005). — p.18.

[35] Z. Shi and A. Z. Genack, *Transmission eigenvalues and the bare conductance in the crossover to Anderson localization*, Phys. Rev. Lett. **108**, 043901 (2012). — p.18.

[36] Z. Shi, J. Wang, and A. Z. Genack, *Microwave "optical" conductance*, arXiv **1303.1133**, (2013). — p.18.

[37] O. N. Dorokhov, *Transmission coefficient and the localization length of an electron in N bound disordered chains*, JETP Lett. **36**, 318 (1982). — p.18.

[38] P. A. Mello, P. Pereyra, and N. Kumar, *Macroscopic approach to multichannel disordered conductors*, Ann. of Phys. **181**, 290 (1988). — p.18.

[39] O. N. Dorokhov, *On the coexistence of localized and extended electronic states in the metallic phase*, Solid State Commun. **51**, 381 (1984). — p.18.

[40] J. B. Pendry, A. MacKinnon, and A. B. Pretre, *Maximal fluctuations – a new phenomenon in disordered systems*, Physica A **168**, 400 (1990). — p.18.

[41] Y. V. Nazarov, *Limits of universality in disordered conductors*, Phys. Rev. Lett. **73**, 134 (1994). — p.19.

[42] V. A. Marčénko and L. A. Pastur, *Distribution of eigenvalues for some sets of random matrices*, Math. USSR-Sbornik **1**, 457 (1967). — p.19, 20.

[43] A. Goetschy and A. D. Stone, *Filtering random matrices: The effect of imperfect channel control in multiple-scattering*, Phys. Rev. Lett. **111**, 063901 (2013). — p.20, 21.

[44] J. W. Goodman, *Statistical optics* (Wiley, New York, 2000). — p.21.

[45] N. Shnerb and M. Kaveh, *Non-Rayleigh statistics of waves in random systems*, Phys. Rev. B **43**, 1279 (1991). — p.22.

[46] E. Kogan, M. Kaveh, R. Baumgartner, and R. Berkovits, *Statistics of waves propagating in a random medium*, Phys. Rev. B **48**, 9404 (1993). — p.22.

[47] T. M. Nieuwenhuizen and M. C. W. van Rossum, *Intensity distributions of waves transmitted through a multiple scattering medium*, Phys. Rev. Lett. **74**, 2674 (1995). — p.22.

[48] W. L. Vos, A. Lagendijk, and A. P. Mosk, in *Light localization and lasing: random and pseudorandom photonic structures*, edited by L. Pavesi and M. Ghulinyan (Cambridge Univ. Press, to be published). — p.23.

[49] W. L. Vos, R. Sprik, A. van Blaaderen, A. Imhof, A. Lagendijk, and G. H. Wegdam, *Strong effects of photonic band structures on the diffraction of colloidal crystals*, Phys. Rev. B **53**, 16231 (1996). — p.23.

[50] A. F. Koenderink, *Emission and transport of light in photonic crystals*, Ph.D. thesis, University of Amsterdam, 2003. — p.23.

[51] O. L. Muskens, S. L. Diedenhofen, B. C. Kaas, R. E. Algra, E. P. A. M. Bakkers, J. Gómez Rivas, and A. Lagendijk, *Large photonic strength of highly tunable resonant nanowire materials*, Nano Lett. **9**, 930 (2009). — p.23.

[52] T. Strudley, T. Zehender, C. Blejean, E. P. A. M. Bakkers, and O. L. Muskens, *Mesoscopic light transport by very strong collective multiple scattering in nanowire mats*, Nat. Photon. **7**, 413 (2013). — p.23.

CHAPTER 3

Focusing Light Through Random Photonic Media By Binary Amplitude Modulation

3.1. Introduction

In many random photonic materials such as paper, paint and biological tissue light is multiply scattered. As a result, the propagation of light becomes diffuse and the materials appear to be opaque. Nevertheless, it has recently been demonstrated that it is possible to control light propagation through such samples by manipulating the incident wavefront [1–9]. An example for controlling light propagation by wavefront manipulation is optical phase conjugation, where a field that exits from the strongly scattering sample is phase conjugated and sent back to retrace its path to reconstruct the intensity pattern of the original incident field [6–9]. Optical phase conjugation is successful in reconstructing a field through random photonic media, however, it does not provide a one-way focusing of light through such samples. First demonstration of one-way focusing of light through [1], or inside [2] strongly scattering materials was achieved by spatially modifying the phase of the incident light wave pixel by pixel using an algorithm to compensate for the disorder in the sample. It was shown that the shape of the focus obtained with this method is independent of experimental imperfections and has the same size as the speckle correlation function [3]. A related approach to control light propagation by wavefront manipulation was demonstrated by Popoff and coworkers. They measured part of the optical transmission matrix, and used it to create a focus [4] and reconstruct an image behind the strongly scattering sample [5]. All of these methods require modulating the phase of the incident wavefront. Therefore the speed of the utilized phase modulator becomes a limiting factor on the applicability of the method to materials whose configuration change rapidly, such as biological samples [7].

Here we introduce a new focusing method based on binary amplitude modulation. The wave incident to the turbid material is spatially divided into a number of segments. A portion of these segments are selectively turned off. In contrast to existing wavefront shaping methods, the phase of the segments is not modified. We demonstrate two implementations of this method to focus light through a multiply scattering TiO_2 sample; one using a liquid crystal on silicon (LC) spatial light modulator (SLM) in amplitude-only modulation mode and the other

This chapter has been published as: D. Akbulut, T. J. Huisman, E. G. van Putten, W. L. Vos and A. P. Mosk, Opt. Express **19**, 4017–4029 (2011)

using a digital micromirror device (DMD). DMDs consist of millions of mirrors that can be independently controlled to reflect light either to a desired position or to a beam dump. This effectively switches light coming from a particular pixel of the DMD on or off and provides a way to spatially modulate the amplitude of light in a binary fashion. The advantage of DMDs over LC SLMs lie in their switching speed. An important figure of merit for switching speed is the settling time, which is the time required for a pixel to become stable after changing its state. For a standard DMD the settling time is 18 μs [10], which is approximately three orders of magnitude faster than that for typical LC SLMs used in the previous works [1–5, 7–9]. Such fast devices as DMDs have the potential to create a focus behind turbid material in time scales shorter than required for the configuration of the sample to change, hence can prove useful for focusing light through biological tissue [7].

We describe the algorithm that is used to create a focus behind a turbid material by selectively turning off the segments of the SLM in Section 3.2. Implementation of the method using an LC SLM is described in Section 3.3. In this section, we present measurements of the enhancement of intensity inside the created focus and compare the results to the enhancements expected under ideal situations. In Section 3.4, we demonstrate focusing light through a turbid material using a MEMS-based SLM. In the Appendix, derivation of an analytical formula for the intensity enhancement from the binary amplitude modulation algorithm is provided.

3.2. The binary amplitude modulation algorithm

Light transport through a strongly scattering sample can be described using the concept of a transmission matrix that connects incident and outgoing scattering channels. Scattering channels are the angular or spatial modes of the propagating light field [11]. In this chapter, we denote incident and outgoing scattering channels as input and output channels, respectively. At the back of the sample the electric field of light at each output channel is related to the electric field of light at each input channel by the transmission matrix of the sample [12]

$$E_m = \sum_{n=1}^{N} t_{mn} E_n, \tag{3.1}$$

where E_m is the electric field at the m^{th} output channel; E_n is the electric field at the n^{th} input channel; and t_{mn} are the elements of the transmission matrix.

In our experiments a light beam incident to a strongly scattering sample is spatially divided into a number of square segments. Each segment corresponds to a specific range of incident angles to the sample. When input channels are described in terms of angular modes of incident light field, each SLM segment covers a range of input channels. As the SLM is divided into more segments, the angular resolution is increased and more input channels are independently controlled. We image the back surface of the sample with a CCD camera. In

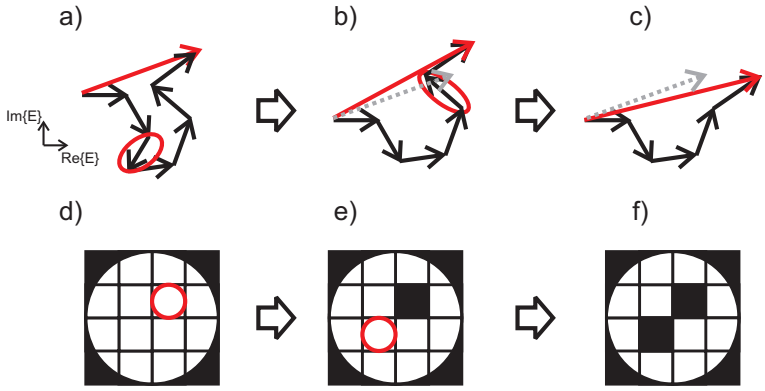

Figure 3.1.: Graphical explanation of the binary amplitude modulation algorithm. (a-c) Complex plane representation of the electric field at the target in successive steps of the algorithm. Small black vectors represent the electric field of each input channel as modified by traveling through the sample. The red vector is the total electric field at the target output channel. Dashed gray vector represents the electric field at the target position before optimization. (d-f) Evolution of the amplitude pattern on the SLM. (a,d) In this step, a segment which contributes negatively to the total amplitude is identified (circled). This segment will be turned off as algorithm proceeds to next segment. (b,e) Subsequently, other segments which contribute negatively are identified and will be turned off. (c,f) At the end of the algorithm, all of the segments which have a negative contribution to the total electric field at the target are turned off.

this case, each diffraction limited spot corresponds to an output channel. In the present experiments we select a single target output channel and use the algorithm to maximize the intensity.

The working principle of the algorithm is illustrated schematically in Fig. 3.1. In the top panel, we see a vectorial representation of the electric field in the selected target channel, E_m. This electric field is a vectorial sum of electric fields of all incident channels multiplied by the corresponding transmission matrix element. With the algorithm all segments of the incident field are successively probed. Each segment is turned on and off while the intensity at the target output channel is being monitored. This procedure can be visualized by following the block arrows in Fig. 3.1 (a-c; d-f). As a result the segments leading to destructive interference with the resultant electric field are turned off and the intensity at the target is increased as compared to the unoptimized case. This increase can be seen by comparing the magnitudes of the red vectors in Fig. 3.1 (a) and Fig. 3.1 (c). The evolution of the amplitude pattern on the SLM can be visualized by following Fig. 3.1 (d-f).

When the algorithm is complete, a two dimensional binary amplitude pattern is obtained on SLM; by sending less light to the sample, more light is concentrated to the position of the focus. This is conceptually similar to focusing light by

a conventional Fresnel zone plate [13]. In fact, with spatial binary amplitude modulation, reconfigurable and high degree of freedom Fresnel zone plates are actively created and utilized to focus light through a strongly scattering material.

3.3. Experiments with a Liquid Crystal Spatial Light Modulator

The setup used in the experiments is shown in Fig. 3.2. A HeNe laser (wavelength 632.8 nm, output power 5 mW) is used as the light source. We pass the beam through a half waveplate and a Glan-Taylor polarizer to obtain vertically polarized light with adjustable power. The beam is expanded with a 30× beam expander (not shown) and sent to a polarizing beam splitter cube (PBS). The vertically polarized light is transmitted through the PBS to fall on the twisted nematic liquid crystal SLM (Holoeye LC-R 2500). Using the technique described in Ref. [14], we can turn a segment of the SLM on or off without changing the phase. Light is projected on to the sample by a 63× 0.95-NA infinity corrected Zeiss microscope objective. Light transmitted through the sample is collected with an identical microscope objective, passed through a polarizer and imaged on to a CCD camera with a 600 mm focal length lens, L3. The effective magnification of the imaging system is 229×. The sample is a 36.5±3.1 μm thick layer of airbrush paint (rutile TiO_2 pigment with acrylic medium). The transport mean free path for similar samples are l_{tr}=0.55±0.1μm at 632.8 nm wavelength [1].

The images captured with the CCD camera before and after the optimization are shown in Fig. 3.3, along with the amplitude map on the SLM. In this case, the SLM is divided into 812 segments. Before the optimization all segments are on and the transmitted intensity pattern is random speckle, Fig. 3.3 (a, b). After the optimization about half of the segments are off and the transmitted intensity pattern is dominated by a single bright spot in the position of target output channel, Fig. 3.3 (c, d). This demonstrates that using spatial binary amplitude modulation, light can be effectively focused behind a multiply scattering medium.

To have a quantitative measure of the contrast between the bright optimized spot and the background, the intensity enhancement η is defined as

$$\eta \equiv \frac{I_{\mathrm{opt}}}{I_{\mathrm{ref}}}, \tag{3.2}$$

where I_{opt} is the optimized intensity inside the target area after spatial binary amplitude modulation is performed for a specific sample and I_{ref} is the reference intensity. To measure a suitable reference intensity, the wavefront that is shaped to give a bright focus at target is sent to different parts of the sample. The intensities measured in target with changing sample configuration are ensemble averaged to give I_{ref}. The enhancement we obtain with this definition gives a measure of the contrast between the focus and the background of the image since the reference intensity is approximately the same as the average background intensity. Since nearly half of the segments on the SLM are turned off in the

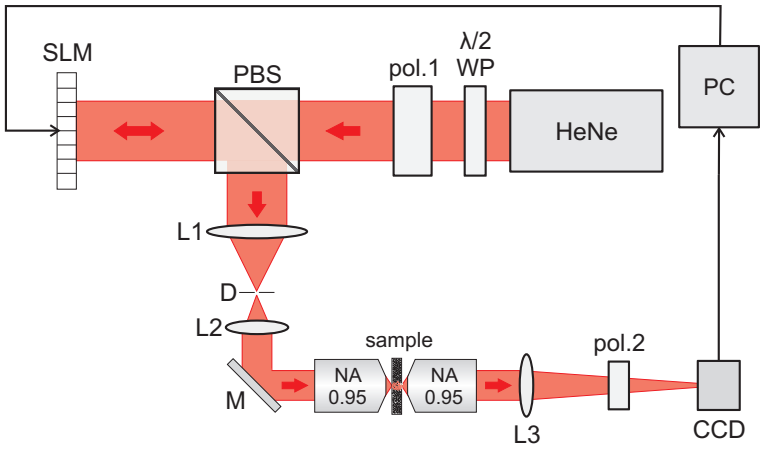

Figure 3.2.: Experimental setup. A HeNe laser beam with a wavelength of 632.8 nm and output power of 5 mW is expanded and passed through a half waveplate ($\lambda/2$ WP), a polarizer (pol.1) and a polarizing beam splitter (PBS) to be reflected off a Holoeye LC-R 2500 liquid crystal spatial light modulator (SLM). Phase and amplitude modulation is decoupled [14]. A high NA (NA=0.95) microscope objective projects the shaped wavefront on the sample and an identical microscope objective collects the light transmitted through the sample. The transmitted intensity pattern is passed through a polarizer (pol.2) and monitored with a CCD camera. The computer (PC) receives intensity pattern from the CCD and adjusts the SLM segments according to the algorithm. L1, 250 mm focal length lens. D, aperture. L2, 150 mm focal length lens. M, mirror. L3, 600 mm focal length lens.

optimized wavefront, the reference intensity is approximately half of the ensemble averaged intensity when all segments are on.

In Fig. 3.4 we show the measured enhancement values as well as the ideally expected enhancement values, using Eq. 3.3. We measured the enhancements for a wide range of segments. The enhancement increases as the SLM is divided into more segments since the number of independently controlled input channels increases. The ideal enhancement η_{ideal} increases linearly with the number of controlled input channels N as

$$\langle \eta_{\text{ideal}} \rangle \approx 1 + \frac{1}{\pi}\left(\frac{N}{2} - 1\right). \tag{3.3}$$

However, deviations from the ideal conditions reduce the intensity enhancement. We have derived (see Appendix) that the intensity enhancement in presence of intensity noise $\langle \eta_{\text{non-ideal}} \rangle$ can be written as

$$\langle \eta_{\text{non-ideal}} \rangle = \langle \eta_{\text{ideal}} \rangle \left(\frac{1}{2} + \frac{1}{\pi}\arctan\left(\frac{SNR}{\sqrt{N}}\right)\right)\frac{\langle A \rangle^2}{\langle A^2 \rangle}, \tag{3.4}$$

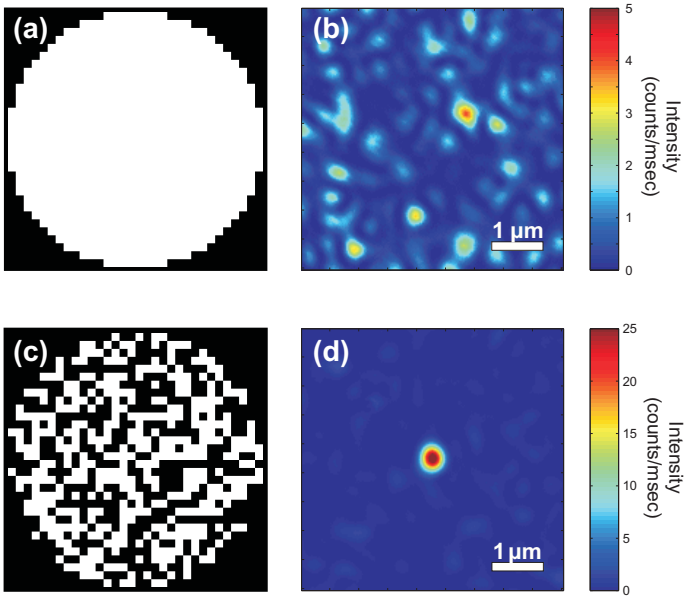

Figure 3.3.: Experimental results of the optimization procedure. (a) Amplitude map written on the SLM before optimization. Active area of the SLM is divided into 812 segments, all of which are on. (b) Image captured by the CCD before optimization is performed. (c) Amplitude map on the SLM after the optimization procedure is complete. (d) Image captured after the optimization is complete. A single bright spot appears on the target point. Note the different color scale between (b) and (d).

where SNR represents the signal to noise ratio of the signal at target position, and $\langle A\rangle^2/\langle A^2\rangle$ is a factor introduced to account for non-uniform illumination of the SLM, with A representing the amplitude of field reflected from each SLM segment. When the illumination pattern of the SLM is investigated, $\langle A\rangle^2/\langle A^2\rangle$ is found to be 0.97±0.01. The derivation of Eq. 3.3 and Eq. 3.4 can be found in the Appendix. The experimental data are fitted to Eq. 3.4 using the signal to noise ratio (SNR) as the only adjustable parameter. The value of the adjusted SNR is found to be 24. From a test performed on the experimental setup with a static binary amplitude pattern on the SLM, the intensity fluctuations of the light incident to the sample was measured and found to have an SNR of 165. The fact that the adjusted SNR has a lower value than measured SNR can be caused by several reasons: in the experiments the state of each segment is updated continuously during an optimization, increasing the rate of wrong decisions as the optimization proceeds. However, Eq. 3.4 assumes that the probability of making a wrong decision for the state of a segment is constant throughout the optimization process. Moreover, Eq. 3.4 takes only intensity noise into account, which is an incomplete description of possible sources of noise or instabilities in the experimental setup. Further investigation of effects of noise and instabilities

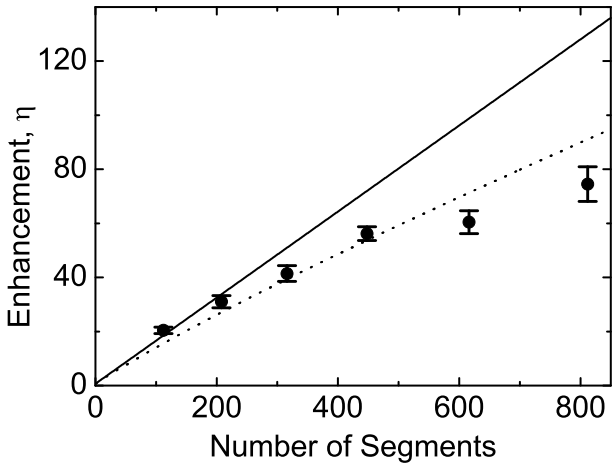

Figure 3.4.: Intensity enhancement at the target position versus the number of segments on the SLM. Black solid line: enhancements expected under ideal conditions, as obtained from Eq. 3.3. Each data point (black circles) is an ensemble average of 14-25 data points obtained from measurements. Bars represent the standard error of each measurement set. Black dotted curve: fit performed for the experimental enhancements using Eq. 3.4 with a single free parameter, SNR. Best curve fit yields SNR=24.

on the performance of the presented algorithm is beyond the scope of this chapter.

Although the implemented algorithm was found to be sensitive to environmental factors, our experimental data convincingly shows that light can be focused through turbid materials using spatial binary amplitude modulation. In our experiments, light intensity at the target position was found to be enhanced up to 75±6 times the average speckle intensity in the background.

3.4. Experiments with a Micro Electro-Mechanical System Based Spatial Light Modulator

Spatial binary amplitude modulation enables the application of MEMS-based devices such as the digital micromirror devices in wavefront shaping experiments. In this section, we describe demonstration of focusing of light through a turbid medium using a MEMS-based SLM to modulate the wavefront. To our knowledge this demonstration is the first MEMS based focusing through turbid media. The SLM that is employed in the experiments described in this section is a disassembled projector (Sharp multimedia projector XR-32X-L), containing a digital micromirror device from Texas Instruments.

The setup used in the MEMS based focusing experiments is shown in Fig. 3.5.

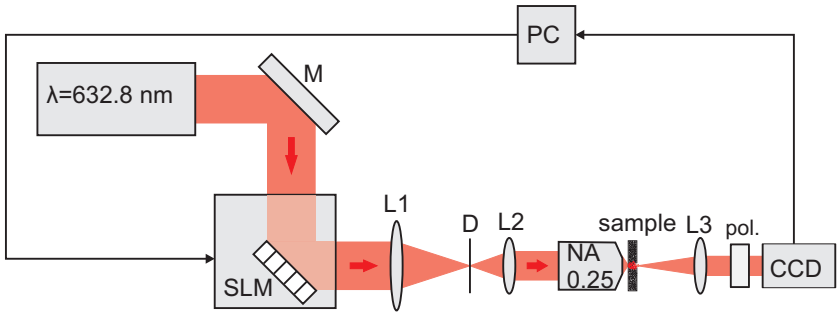

Figure 3.5.: Experimental setup for MEMS-based focusing. A HeNe laser beam that has a wavelength of 632.8 nm and output power of 2 mW is expanded and used to illuminate the SLM via a mirror (M). L1, L2 and L3 are planoconvex lenses with respectively 150 mm, 50 mm and 50 mm focal lengths. D is an aperture used for spatial filtering, and NA 0.25 is a microscope objective having 10× magnification and 0.25 numerical aperture. Light exiting the sample is converted to far field with L3, passed through a polarizer, pol. and projected on a CCD camera, which is connected to the SLM via a PC.

A HeNe laser, which has a wavelength of 632.8 nm and an output power of 2 mW is used as the light source. The beam is expanded with a 10× beam expander (not shown) and sent to the digital micromirror device (DMD) based SLM. The DMD consists of 1024×768 square mirrors each having a size of 10.91×10.91 μm. Each mirror can exhibit two angles; it either reflects light to the intended target or into a light dump [10]. Light reflected from the DMD is projected onto the sample by a 10× 0.25 NA microscope objective and light transmitted through the sample is passed through a polarizer and projected on the CCD camera with a 50 mm focal length lens. The sample that is used in the experiments described in this section is 18.5±2.4 μm thick layer of airbrush paint (rutile TiO_2 pigment with acrylic medium). The transport mean free path for similar samples are l_{tr}=0.55±0.1μm at a wavelength of 632.8 nm [1].

The images captured with the CCD camera before and after the optimization are shown in Fig. 3.6. We successfully focused light through a layer of paint using a MEMS based device. The intensity enhancement is defined here as the ratio of the average intensity inside the bright optimized spot to the average intensity outside the spot, and the highest intensity enhancement that could be obtained with the setup in Fig. 3.5 was found to be 19. However, an ideal enhancement of 514 is expected from Eq. 3.3. The low enhancements are thought to be the consequence of the DMD being embedded into a commercial display projector, introducing undesirable features for our purpose. Such features include turning off of the pixels of the DMD with a predefined timing, which we could not control. Lack of mechanical damping or control of noise sources in the setup is proposed to be another reason for obtaining a reduced enhancement in our experiments.

The DMDs are known to have very fast switching between on and off states

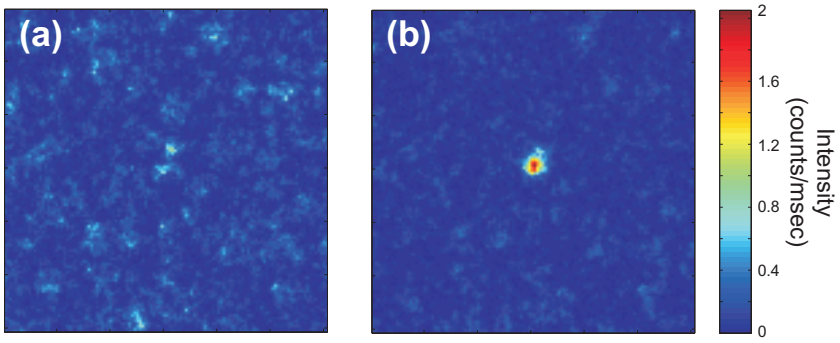

Figure 3.6.: (a) Image of an area of 121 by 121 pixels of the camera is presented just before the optimization process. (b) The same area is presented after the optimization process was finished. An enhancement of 18× is seen. In both figures, the intensity is measured in counts/milliseconds and presented on the same scale. The SLM is divided into 3228 segments.

and a settling time of 18 μs [10]. In our experiments, the optimizations using a DMD chip was achieved in a time scale of several minutes, which is similar to time scales of optimizations performed using the LC SLMs. This effect is due to addressing the device via the video card of the PC, which was performed in the same manner for both SLMs, limiting the communication speed to 60 Hz. With faster control of the DMD devices and use of faster cameras for detection, the speed of the method will increase close to three orders of magnitude and the method will be useful for focusing through materials whose configuration change in short time scales, like biological tissue and can be used for medical imaging purposes.

3.5. Conclusion

We have demonstrated focusing of light through strongly scattering materials by spatially modulating the amplitude of the incident field. From experiments, we have obtained an enhancement of 75 of the target intensity, when the incident wavefront is divided into 812 independently controlled segments. We have also implemented the method using a commercial projector that has a MEMS-based digital micromirror device as the spatial light modulator, providing the first demonstration of MEMS-based focusing of light through turbid materials. Use of MEMS technology will enable a fast and versatile way to control light through turbid materials.

3.A. Analytical Expression for Ideal Intensity Enhancement

When no optimization is performed in the system a plane wave is sent to the sample and the amplitude A and phase ϕ of the electric field E_n in input channel n is equal to

$$E_n = Ae^{i\phi}. \tag{3.5}$$

Since the phase of incident field is assumed to be constant for an unoptimized wavefront, it can as well be taken as ϕ=0, so that $E_n = A$ when no optimization is performed and E_n is either 0 or A after optimization is complete.

For a multiple scattering sample, phases of the transmission matrix elements, $\arg(t_{mn})$ have a uniform distribution between $-\pi$ and π [12]. The amplitudes of the transmission matrix elements, $|t_{mn}|$, on the other hand are approximated by a Rayleigh probability density function.[1] The electric field at the target output channel is a vectorial sum of random phasors

$$E_m = \sum_{n=1}^{N} |t_{mn}| e^{i\arg(t_{mn})} E_n. \tag{3.6}$$

Reference light intensity at the target position is the ensemble average of intensities recorded in the target for different sample configurations

$$I_{\text{ref}} = \langle E_m^* E_m \rangle, \tag{3.7}$$

$$I_{\text{ref}} = \langle \sum_{k}^{N'} A|t_{mk}| e^{-i(\arg(t_{mk}))} \sum_{n}^{N'} A|t_{mn}| e^{i(\arg(t_{mn}))} \rangle, \tag{3.8}$$

the same wavefront is assumed to be sent to the sample while both the intensity inside the focus and the reference intensity are calculated, so that N' is the number of segments that remain on after the optimization procedure is finished. It is important to emphasize that the wavefront is optimized for a certain configuration of the sample and is effectively a randomly shaped wavefront for a different configuration of the sample. So, while I_{ref} is calculated, light coming from different input channels have random phases at the target position. In this case we assume that the phase of each vector constituting E_m is drawn from a distribution that is uniform between $-\pi$ and π. Using this assumption and the fact that the transmission matrix elements and the incident field are statistically independent, the reference intensity can be written as

$$I_{\text{ref}} = N' \langle t^2 \rangle \langle A^2 \rangle, \tag{3.9}$$

where the modulus of a transmission matrix element, t is a random variable having a Rayleigh probability density function.

[1] For the sake of simplicity, subtle correlations between the transmission matrix elements are ignored in this chapter.

If light fields interfere constructively at a certain position, a bright field will be obtained at that position. For this purpose, we probe the projection of the field coming from various input channels on the resultant electric field. The algorithm decides whether a segment shall be on after comparing the intensities at the target for the segment being on and segment being off cases. A segment is kept on if it contributes positively to the intensity at the target position. The contribution of the k^{th} segment to the target intensity, ΔI_k is

$$\Delta I_k = |E_m|^2 - |E_m - E_k t_{mk}|^2. \tag{3.10}$$

Since ΔI_k is a sum of uncorrelated random variables, it has a Gaussian distribution due to the Central Limit Theorem. Therefore the number of segments that remain on after the optimization is determined by the probability of drawing a positive random variable from the distribution

$$f(\widetilde{\Delta I_k}) = \frac{1}{\sigma\sqrt{2\pi}} e^{-\frac{(\widetilde{\Delta I_k}-\mu)^2}{2\sigma^2}}, \tag{3.11}$$

where $\widetilde{\Delta I_k}$ is a random variable representing ΔI_k. This distribution has a mean value of

$$\mu = A^2\langle t^2\rangle, \tag{3.12}$$

and a standard deviation of

$$\sigma = \sqrt{\langle t^4A^4\rangle + (2N-3)\langle t^2A^2\rangle^2}. \tag{3.13}$$

The number of segments that are on after the optimization is

$$N' = NP(x>0) = \int_0^\infty \frac{N}{\sigma\sqrt{2\pi}} e^{-\frac{(x-\mu)^2}{2\sigma^2}} dx, \tag{3.14}$$

$$= \frac{N}{2}\mathrm{erfc}\left(\frac{-\mu}{\sigma\sqrt{2}}\right). \tag{3.15}$$

We assume that the phases of the segments that remain on are uniformly distributed between $(-\pi/2, \pi/2)$ after the optimization, so we have

$$\langle I_{\mathrm{opt}}\rangle = \langle E_m^* E_m\rangle, \tag{3.16}$$

$$= N'\langle A^2t^2\rangle + N'(N'-1)\langle At\rangle^2\frac{4}{\pi^2}. \tag{3.17}$$

Under ideal conditions, i.e. when noise and instabilities are ignored, the ensemble averaged intensity enhancement at the target position, $\langle\eta_{\mathrm{ideal}}\rangle$ is found to be

$$\langle\eta_{\mathrm{ideal}}\rangle = \frac{\langle I_{\mathrm{opt}}\rangle}{\langle I_{\mathrm{ref}}\rangle} = 1 + \frac{1}{\pi}(N'-1). \tag{3.18}$$

When the number of controlled input channels is large, $\langle\eta_{\mathrm{ideal}}\rangle$ becomes

$$\langle\eta_{\mathrm{ideal}}\rangle \approx 1 + \frac{1}{\pi}\left(\frac{N}{2} - 1\right). \tag{3.19}$$

A factor of $\pi^2/2$ more intensity enhancement can be obtained from phase modulation [1]. This is expected since with phase shaping method, all E_n are actively assigned a phase leading to total constructive interference at the target while with binary amplitude shaping active modification of the phases is not performed. The remarkable fact that the enhancement from a 1-bit modulation method can be comparable to a full analog phase modulation has been observed previously in the context of one-channel acoustic time-reversal experiments [15].

In deriving Eq. 3.19 the amplitude of the fields in all input channels were assumed to be the same. However, in our experiments, a Gaussian beam impinges on the SLM and the amplitude of each input channel's field is modified accordingly. This introduces a prefactor of $\langle A\rangle^2/\langle A^2\rangle$ to the theoretically expected enhancement [16]. In the experiments described in Section 3, this prefactor is found to have a value of 0.97 ± 0.01.

3.B. Analytical Expression for Intensity Enhancement Under Intensity Noise

We now proceed to include the effect of noise on the intensity enhancement. We take into account noise due to intensity fluctuations of the incident light to the sample. Noise affects the correctness of the decision on whether to keep each segment of the SLM on or off. Under noisy conditions P_{wrong} is the probability for the algorithm to make a wrong decision for the state of a single segment, *i.e.*, keeping it on while it should be turned off and vice versa. This probability is

$$P_{\text{wrong}} = P(\Delta I_k > 0 \bigwedge \Delta I_k^{exp} < 0) + P(\Delta I_k < 0 \bigwedge \Delta I_k^{exp} > 0), \tag{3.20}$$

where ΔI_k^{exp} is the experimentally measured difference between the target intensities for on and off states of the k^{th} segment and ΔI_k is the ideal difference between the target intensities for on and off states of the k^{th} segment. $P(\Delta I_k > 0 \bigwedge \Delta I_k^{exp} < 0)$ is the probability of experimentally measuring a negative ΔI_k^{exp} while under ideal conditions, ΔI_k is positive. Likewise, $P(\Delta I_k < 0 \bigwedge \Delta I_k^{exp} > 0)$ is the probability of experimentally measuring a positive ΔI_k^{exp} while under ideal conditions ΔI_k is negative.

$$P_{\text{wrong}} = \int_0^\infty f(\widetilde{\Delta I_k}) \int_{-\infty}^0 f(\widetilde{\Delta I_k^{exp}}) d\widetilde{\Delta I_k^{exp}} d\widetilde{\Delta I_k} + \int_{-\infty}^0 f(\widetilde{\Delta I_k}) \int_0^\infty f(\widetilde{\Delta I_k^{exp}}) d\widetilde{\Delta I_k^{exp}} d\widetilde{\Delta I_k}. \tag{3.21}$$

Here $\widetilde{\Delta I_k}$ is a random variable representing ΔI_k and has the probability density function as given in Eq. 3.11. Similarly, $\widetilde{\Delta I_k^{exp}}$ is a random variable representing ΔI_k^{exp} and has the probability density function

$$f(\widetilde{\Delta I_k^{exp}}) = \frac{1}{(\sqrt{2})\sigma_{\text{noise}}\sqrt{2\pi}} e^{-\frac{(\widetilde{\Delta I_k^{exp}} - \Delta I_k)^2}{4\sigma_{\text{noise}}^2}}, \tag{3.22}$$

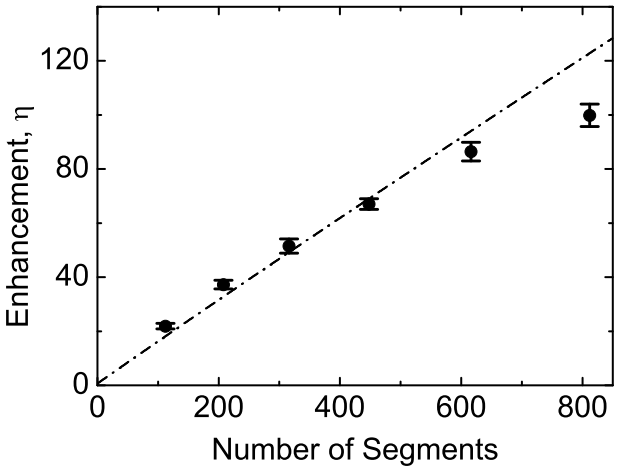

Figure 3.7.: Numerically simulated intensity enhancement at the target position versus the number of segments that the SLM is divided into. Each data point represented by the black circles is an ensemble average of a set of data points obtained from simulations conducted with an intensity noise of SNR=165. Bars represent the standard error of each measurement set. The dashed line shows the enhancements obtained from Eq. 3.25, assuming $\langle A\rangle^2/\langle A^2\rangle = 1$ and using Eq. 3.19.

with $\widetilde{\Delta I_k^{exp}}$ having a mean of ΔI_k and a standard deviation of $\sqrt{2}\sigma_{\text{noise}}$, where σ_{noise} is the standard deviation for noise. Thus, P_{wrong} can be evaluated as

$$P_{\text{wrong}} = \frac{1}{2} - \frac{1}{\pi}\arctan\left(\frac{\sigma}{\sqrt{2}\sigma_{\text{noise}}}\right). \tag{3.23}$$

From Eq. 3.13, it is reasonable to assume that $\sigma = \sqrt{2N}\langle A^2t^2\rangle$ for large N. σ_{noise} can be written as $\sigma_{\text{noise}} = \langle I_m\rangle/SNR = N\langle A^2t^2\rangle/SNR$. Substituting σ and σ_{noise} in Eq. 3.23, we obtain

$$P_{\text{wrong}} = \frac{1}{2} - \frac{1}{\pi}\arctan\left(\frac{SNR}{\sqrt{N}}\right). \tag{3.24}$$

The possibility of making wrong decisions for a segment leads to observation of a reduced intensity enhancement as compared to the ideal case. Using Eq. 3.24, and the prefactor of $\langle A\rangle^2/\langle A^2\rangle$, the intensity enhancement at target position including the effects of noise and a Gaussian illumination profile, $\langle\eta_{\text{non-ideal}}\rangle$ is given by

$$\begin{aligned}\langle\eta_{\text{non-ideal}}\rangle &= \langle\eta_{\text{ideal}}\rangle(1-P_{\text{wrong}})\frac{\langle A\rangle^2}{\langle A^2\rangle},\\ &= \langle\eta_{\text{ideal}}\rangle\left(\frac{1}{2}+\frac{1}{\pi}\arctan\left(\frac{SNR}{\sqrt{N}}\right)\right)\frac{\langle A\rangle^2}{\langle A^2\rangle}.\end{aligned} \tag{3.25}$$

In Fig. 3.7 we show the enhancements obtained from Eq. 3.25 along with the enhancements obtained from simulations for a case where incident light fluctuates with SNR=165. Only intensity noise is considered in the simulations, with SNR being kept constant and the fluctuations in the signal being increased with increased signal intensity. Other sources of noise or instabilities, for instance, detection noise in the CCD or drifts of the sample relative to illumination and detection optics are neglected. It can be seen from Fig. 3.7 that as N increases the enhancements obtained from the simulations become lower than the enhancements expected from Eq. 3.25. We attribute this observation to the fact that the optimal state for each segment is directly applied to the segment as the simulation progresses (as is the case for the experiments) instead of being stored in a separate place to be updated in the end of the simulation. Updating the state of the segments as the simulation progresses leads to an increase in the target intensity, which in turn, leads to an increase in the amplitude of intensity fluctuations in the target. This dynamic increase of the error probability is not taken into account in the derivation of Eq. 3.25. For large N, the increase in the target intensity during the simulation is larger, therefore the amount of noise considered in the simulation and the analytical expression is more different as compared to small N, leading to a more prominent deviation between the simulation and the analytical expression for large N. Further investigation of the effects of noise on the quality of obtained foci is beyond the scope of this chapter and is an interesting subject for further studies.

Bibliography

[1] I. M. Vellekoop and A. P. Mosk, *Focusing coherent light through opaque strongly scattering media*, Opt. Lett. **32**, 2309 (2007). — p.29, 30, 32, 36, 40.

[2] I. M. Vellekoop, E. G. van Putten, A. Lagendijk, and A. P. Mosk, *Demixing light paths inside disordered metamaterials*, Opt. Express **16**, 67 (2008). — p.29, 30.

[3] I. M. Vellekoop, A. Lagendijk, and A. P. Mosk, *Exploiting disorder for perfect focusing*, Nat. Photon. **4**, 320 (2010). — p.29, 30.

[4] S. M. Popoff, G. Lerosey, R. Carminati, M. Fink, A. C. Boccara, and S. Gigan, *Measuring the transmission matrix in optics: An approach to the study and control of light propagation in disordered media*, Phys. Rev. Lett. **104**, 100601 (2010). — p.29, 30.

[5] S. Popoff, G. Lerosey, M. Fink, A. C. Boccara, and S. Gigan, *Image transmission through an opaque material*, Nat. Commun. **1**, 1 (2010). — p.29, 30.

[6] Z. Yaqoob, D. Psaltis, M. S. Feld, and C. Yang, *Optical phase conjugation for turbidity suppression in biological samples*, Nat. Photon. **2**, 110 (2008). — p.29.

[7] M. Cui, E. J. McDowell, and C. Yang, *An in vivo study of turbidity suppres-*

sion by optical phase conjugation (TSOPC) on rabbit ear, Opt. Express **18**, 25 (2010). — p.29, 30.

[8] M. Cui and C. Yang, *Implementation of a digital optical phase conjugation system and its application to study the robustness of turbidity suppression by phase conjugation*, Opt. Express **18**, 3444 (2010). — p.29, 30.

[9] C.-L. Hsieh, Y. Pu, R. Grange, G. Laporte, and D. Psaltis, *Imaging through turbid layers by scanning the phase conjugated second harmonic radiation from a nanoparticle*, Opt. Express **18**, 20723 (2010). — p.29, 30.

[10] D. Dudley, W. Duncan, and J. Slaughter, *Emerging digital micromirror device (DMD) applications*, Proceedings SPIE **4985**, 14 (2003). — p.30, 36, 37.

[11] C. W. J. Beenakker, *Random-matrix theory of quantum transport*, Rev. Mod. Phys. **69**, 731 (1997). — p.30.

[12] J. W. Goodman, *Statistical optics* (Wiley, New York, 2000). — p.30, 38.

[13] M. Born and E. Wolf, *Principles of optics* (Cambridge University Press, 2003). — p.32.

[14] E. G. van Putten, I. M. Vellekoop, and A. P. Mosk, *Spatial amplitude and phase modulation using commercial twisted nematic LCDs*, Appl. Opt. **47**, 2076 (2008). — p.32, 33.

[15] A. Derode, A. Tourin, and M. Fink, *Ultrasonic pulse compression with one-bit time reversal through multiple scattering*, Journal of Applied Physics **85**, 6343 (1999). — p.40.

[16] F. van Beijnum, *Light takes no shortcuts*, Master's thesis, University of Twente, 2009. — p.40.

CHAPTER 4
Experimental Methods

4.1. Introduction

In this chapter we describe in detail the apparatus, the experimental procedures, and the data analysis procedures for transmission matrix measurements. We also discuss sources of noise in transmission matrix measurements and how they affect the results.

A transmission operator describes the relation between the fields incident to and transmitted through the sample. A transmission matrix is a matrix representation of this transmission operator in a pre-chosen basis. In an experiment, a matrix $\widetilde{T}$ is measured, consisting of fields transmitted through the sample in response to the incident fields generated from a pre-determined basis set. The matrix $\widetilde{T}$ is not exactly the same as the transmission matrix of the sample T, since it is modified by the response of the optical setup and the substrate of the sample. By measuring the response matrix of a blank substrate we correct for the difference between the recorded matrix $\widetilde{T}$ and the transmission matrix of the sample T in a numerical model[1] that we developed to interpret our measurements.

The experimental apparatus consisting of the field generation module and the field detection module is described in Section 4.2. The data analysis procedure is described in Section 4.3, including a discussion on the sources of noise in our measurements and their effect on the singular values of measured transmission matrices.

4.2. Experimental apparatus

In a very broad sense, a setup for transmission matrix measurements needs two main parts: a field generation module and a field detection module. The sample of interest is placed in between these two main modules.

The experimental setup constructed for transmission matrix measurements is shown in Fig. 4.1. A HeNe laser is used as a monochromatic light source with a wavelength $\lambda = 632.8$ nm. The laser output beam is expanded $20\times$ in diameter in order to overfill the SLM without getting cropped by the optics in the setup, and is collimated. The expanded beam is divided into two arms; light in one arm is sent to the field generation module and light in the other arm is sent to the

[1] The numerical model is described in detail in Chapter 5.

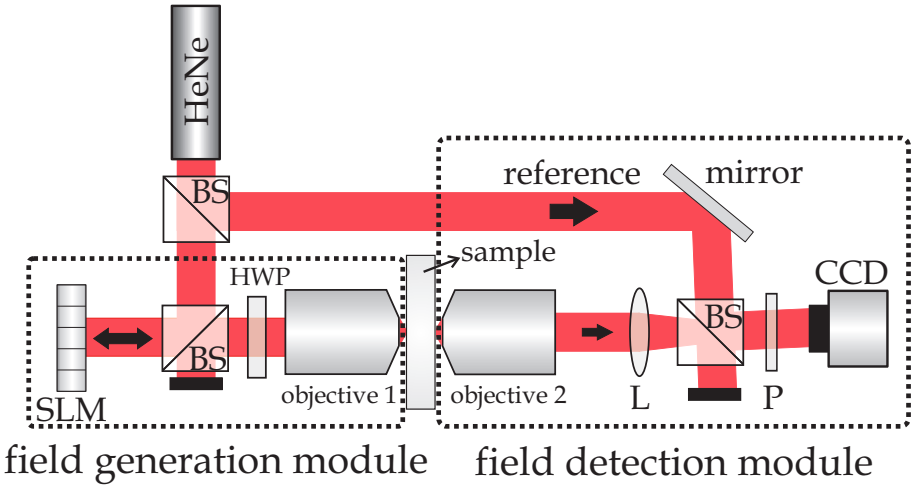

Figure 4.1.: Experimental setup for transmission matrix measurements. The field generation and field detection modules are designated by separate boxes (dashed lines). HeNe: laser. BS: 50:50 beam splitter. SLM: phase-only spatial light modulator. HWP: half-wave plate. P: polarizer. CCD: camera sensor.

field detection module as a reference beam. Wavefronts generated by the field generation module are incident on the sample. Outgoing wavefronts from the sample are relayed to the field detection module by a microscope objective and a lens, with a calculated magnification of 167×.

4.2.1. Field generation

In a transmission matrix measurement, first the basis of choice is determined. In our experiments, we study transmission matrices using monochromatic light. Therefore, we only have spatial degrees of freedom for the generated and detected fields. Fields are spatially manipulated using a spatial light modulator (SLM). A SLM is a pixelated device that has on the order of a million pixels, each of which can be modified -in principle- independently in order to modify the field that is transmitted through or reflected from the SLM. These devices are commonly used in projectors [1] and have been widely used in the fields of microscopy and wavefront shaping, for reviews, see references [2, 3] and the references therein.

The SLM is a Holoeye Pluto phase-only liquid crystal SLM with 1920 by 1080 pixels. Depending on the applied voltage, each pixel can apply a phase shift between 0-2π to the field that is reflected from it. In the experiments described in Chapters 5 and 6, the SLM pixels were grouped together into segments of 3 by 3 and 2 by 2 pixels, respectively.

In our experiments, we choose to define the transversal modes of the incident and outgoing fields in a real space basis. In this case, we can describe these modes as diffraction limited spots on the front surface of the sample, which

form an overcomplete basis, as is described in Section 4.3. In our experimental setup, the SLM and the front surface of the sample are in each other's Fourier planes. In order to obtain a single focus at the center of the area of interest on the front surface of the sample, a flat phase profile is written on the SLM. During transmission matrix recording, this single focus is scanned over the area of interest on the front surface of the sample by applying phase gradients on the SLM.

4.2.2. Field detection

In the optical regime, because of the high temporal frequency of the field, it is not possible to obtain the spatial phase distribution of a wavefront directly, we need to use techniques like interferometry or for simple beam profiles, wavefront sensors. In our experiments, we use a new method that we developed, based on off-axis holographic detection. Off-axis holography was first proposed by Leith and Upatnieks [4]. Its digital implementation for field detection was proposed by Takeda [5], and has been widely used since then [6–11]. We base our wavefront detection on this method because it is an interferometric detection method that requires a single recorded image and therefore insensitive to laser intensity fluctuations. To record the interference pattern of the signal and reference beams, an AVT Dolphin 145B CCD camera with 1392 by 1040 pixels of size 6.45 μm by 6.45 μm is utilized. The images are recorded with 12 bit resolution analog to digital conversion and are analyzed using Matlab to retrieve the signal field from the interference pattern. The procedure of retrieving the signal field is described in Sections 4.2.2.1 and 4.2.2.2.

4.2.2.1. Off-axis holographic detection

Off-axis holographic methods rely on the interference of a signal beam with a reference beam where the signal beam's propagation direction makes a 90° angle with the sensor plane and the reference is tilted by an angle θ with respect to the signal beam. This tilt between the two beams introduces an additional spatial carrier frequency on top of the interference pattern between the signal and reference beams. We denote the field in the signal arm as E_s and the field in the reference arm as E_r. In the CCD sensor plane,

$$E_s(x,y) = |E_s(x,y)|e^{i\phi_s(x,y)}, \tag{4.1}$$
$$E_r(x,y) = |E_r(x,y)|e^{i\phi_r(x,y)-i2\pi qx-i2\pi qy}. \tag{4.2}$$

Here $q = \sin(\theta)/\lambda$ is the phase gradient attained due to tilt on top of $\phi_r(x,y)$.[2] Now, we set the reference phase, $\phi_r(x,y) = 0$ and assume that the phase gradients

[2] A small modification in $\phi_r(x,y)$ attained due to propagation into the tilted plane is neglected.

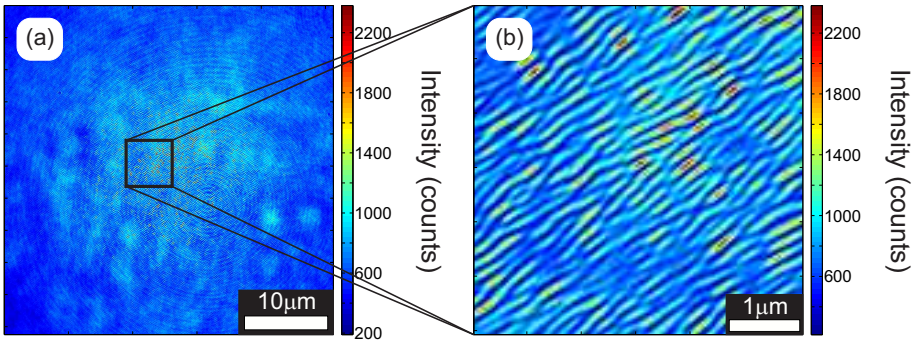

Figure 4.2.: (a) Interference between the signal and the reference over the full field of view of CCD. (b) Zoom-in on part of the interference pattern shown in (a).

in x and y directions are the same. The recorded intensity is then equal to

$$\begin{aligned} I(x,y) =& |E_r(x,y) + E_s(x,y)|^2 && \text{(4.3a)} \\ =& |E_r(x,y)|^2 + |E_s(x,y)|^2 \\ &+ |E_s(x,y)E_r(x,y)|e^{i(\phi_s(x,y)+2\pi qx+2\pi qy)} \\ &+ |E_s(x,y)E_r(x,y)|e^{i(-\phi_s(x,y)-2\pi qx-2\pi qy)} && \text{(4.3b)} \\ =& a(x,y) + c(x,y)e^{i(2\pi qx+2\pi qy)} + c^*(x,y)e^{i(-2\pi qx-2\pi qy)}. && \text{(4.3c)} \end{aligned}$$

The terms giving rise to the intensity pattern can be grouped into two:
(i) The background or dc term which is the sum of the intensity patterns of signal and reference

$$a(x,y) \equiv |E_r(x,y)|^2 + |E_s(x,y)|^2. \tag{4.4}$$

This term contains no interference.
(ii) The terms that contain the phase information

$$c(x,y)e^{i(2\pi qx+2\pi qy)} \equiv |E_s(x,y)E_r(x,y)|e^{i\phi_s(x,y)}e^{i(2\pi qx+2\pi qy)} \tag{4.5a}$$

$$c^*(x,y)e^{i(-2\pi qx-2\pi qy)} \equiv |E_s(x,y)E_r(x,y)|e^{-i\phi_s(x,y)}e^{i(-2\pi qx-2\pi qy)}. \tag{4.5b}$$

In Fig. 4.2, a captured interference pattern is shown, as given in Eq. 4.3a to 4.3c. When this pattern is investigated closely, distorted diagonal fringes are noticed. The tilt between the reference and signal beams gives rise to these fringes. Their distortion is due to the complicated phase pattern of the speckle field, with a possible contribution from non-smooth phase pattern of the reference beam. When two plane waves are interfered, we observe only diagonal stripes when a tilt is introduced between the beams.

To retrieve the phase information of the signal and the reference beams from the interference pattern in a single shot, we need to separate the terms $c(x,y)$ or $c^*(x,y)$ from the term $a(x,y)$. This can be achieved in momentum space since the terms $c(x,y)$ and $c^*(x,y)$ have a phase gradient that corresponds to a spatial

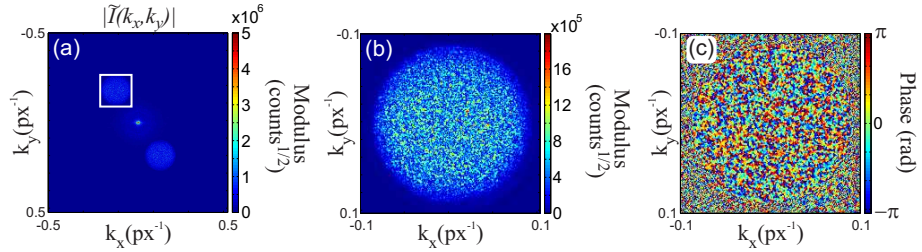

Figure 4.3.: (a) Modulus of the Fourier transform of the interference between the signal and the reference. (b) Modulus and (c) phase of the field in the $+1^{st}$ order region enclosed by the white square shown in (a).

carrier frequency q. When we take the Fourier transform of the expression 4.3c, we have

$$\widetilde{I}(k_x, k_y) = A(k_x, k_y) + C(k_x - q, k_y - q) + C^*(-k_x - q, -k_y - q), \tag{4.6}$$

with

$$A(k_x, k_y) \equiv \mathcal{F}\{a(x, y)\}, \tag{4.7a}$$
$$C(k_x, k_y) \equiv \mathcal{F}\{c(x, y)\}, \tag{4.7b}$$
$$C^*(-k_x, -k_y) \equiv \mathcal{F}\{c^*(x, y)\}. \tag{4.7c}$$

The momentum space map of $|\widetilde{I}(k_x, k_y)|$ is shown in Fig. 4.3 (a). Three distinct regions are visible in this figure. The region centered at $(k_x, k_y) = (0, 0)$ is $A(k_x, k_y)$, Eq. 4.7a, which is the sum of the signal and the reference intensities in momentum space. The terms $|C(k_x - q, k_y - q)|$ and $|C^*(-k_x - q, -k_y - q)|$ are centered at spatial frequencies $k = \pm q$ with $C(k_x, k_y)$ and $C^*(-k_x, -k_y)$ expressed by Eq. 4.7b and Eq. 4.7c respectively. A zoom-in of the modulus of the field $|C(k_x - q, k_y - q)|$ located at the region on top left is shown in Fig. 4.3 (b) and the corresponding phase is shown in Fig. 4.3 (c).[3]

Now we filter $C(k_x - q, k_y - q)$ and translate it in momentum space so that it is centered at $(k_x, k_y) = 0$, *i.e.* we set the spatial carrier frequency q to 0. Later, we take its inverse Fourier transform to get

$$c(x, y) = |E_s(x, y)E_r(x, y)|e^{i\phi_s(x,y)}. \tag{4.8}$$

If the reference beam has a flat amplitude and phase profile, *i.e.*, $E_r(x, y) = 1$ then $c(x, y)$ gives directly the complex amplitude profile of the signal beam.

4.2.2.2. Field detection procedure

Until now, we have explained the well-known off-axis holographic field detection method partially following Ref. [11] and demonstrating main steps with figures

[3] As will be explained in Section 4.2.2.2, the fields shown in Fig. 4.3 are slightly different than ideal $|\widetilde{I}(k_x, k_y)|$, until then we ignore this difference.

captured in our setup. In conventional off-axis holography methods, the reference field must have a constant amplitude to permit accurate retrieval of the signal amplitude using the 1^{st} or -1^{st} order region as shown in Fig. 4.3 (b) and (c). Inspired by the work of Popoff et al. [12], who used a speckled reference, we have developed a new method to retrieve amplitude information in off-axis holography even if the reference amplitude is not constant along its beam profile.

While the beating term between the signal and the reference is ideally given by Eq. 4.8, in an experiment, the fringe visibility of the spatial carrier is reduced due to the modulation transfer function of the detection system. The modulus of the measured beating term $\widetilde{c}$ becomes

$$\begin{aligned} |\widetilde{c}(x,y)| &= M|c(x,y)| && (4.9)\\ &= M|E_s(x,y)||E_r(x,y)|. && (4.10) \end{aligned}$$

Here M represents the modulation transfer function of the detection system in the 1^{st} order region, which is assumed to be constant. The modulation transfer function reduces with increased spatial frequency and expresses the fact that fast spatial modulations (high spatial frequencies k) are imaged with a reduced contrast due to effects such as the size and shape of camera pixels [13, 14]. In order to keep a high value of the modulation transfer function, the tilt angle between the signal and the reference is chosen to be smaller than the maximum (see Fig. 4.3) so that $\pm 1^{st}$ order regions are centered at small spatial frequencies in momentum space. Besides this, care is taken so that the 0^{th} and $\pm 1^{st}$ order regions in the momentum space picture of the interference pattern do not overlap.

When $E_r(x,y) \neq 1$, $c(x,y) \neq E_s(x,y)$. In this case, by combining the measurements of the function $a(x,y)$ and $c(x,y)$, we obtain from their suitable linear combination

$$\begin{aligned} a(x,y) + 2\frac{|\widetilde{c}(x,y)|}{M} &= |E_s(x,y)|^2 \\ &\quad +|E_r(x,y)|^2 + 2|E_s(x,y)||E_r(x,y)| \\ &= (|E_s(x,y)| + |E_r(x,y)|)^2, && (4.11) \end{aligned}$$

and,

$$\begin{aligned} a(x,y) - 2\frac{|\widetilde{c}(x,y)|}{M} &= |E_s(x,y)|^2 \\ &\quad +|E_r(x,y)|^2 - 2|E_s(x,y)||E_r(x,y)| \\ &= (|E_r(x,y)| - |E_s(x,y)|)^2. && (4.12) \end{aligned}$$

From these relations, for $|E_r| > |E_s|$ we can write the magnitude of the signal

$$|E_s(x,y)| = \frac{\sqrt{a(x,y) + 2\frac{|\widetilde{c}(x,y)|}{M}} - \sqrt{|a(x,y) - 2\frac{|\widetilde{c}(x,y)|}{M}|}}{2}. \qquad (4.13)$$

We found that the factor M that best describes our measurements changes between different measurements and its maximum value is M=0.84. At the end of

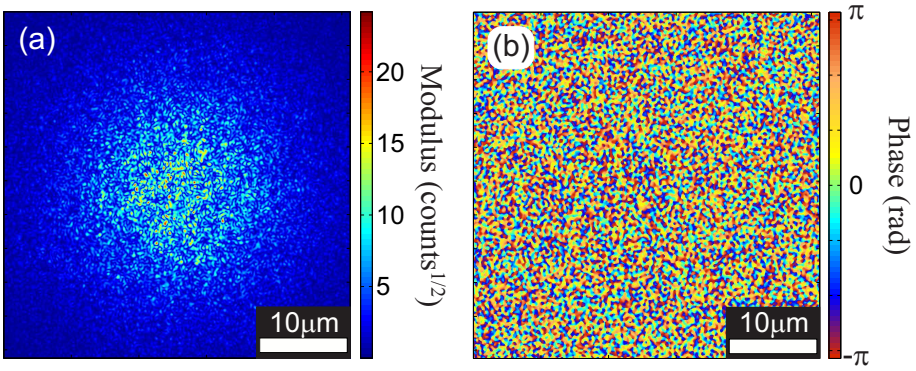

Figure 4.4.: (a) Modulus (b) phase of the signal, E_s as retrieved from the recorded interference pattern.

the procedure described above, using M=0.84, the signal field is obtained and is shown in Fig. 4.4.

In Fig. 4.5, we show the retrieved intensity, as given by $|E_s(x,y)|^2$ versus the intensity directly measured on a CCD camera. $|E_s(x,y)|$ is given by Eq. 4.13. Each data point in Fig. 4.5 represents the intensity in a single pixel. Fig. 4.5 (a) is the case when we corrected for a modulation transfer function of 0.84; the retrieved signal intensity in each pixel is spread around the corresponding measured intensity. Fig. 4.5 (b) is the case when no modulation transfer function correction is made. In this case, the retrieved signal intensities stay below the measured intensities for most intensity values. We see that correcting for a modulation transfer function that is constant over the 1^{st} order region in k-space considerably improves the agreement between retrieved and measured intensities.

In Fig. 4.6 (a) and (b), we show the spatial intensity profiles of the signal retrieved from the interferometric detection and the signal captured directly with the CCD while the reference arm is blocked. It is seen that the spatial profiles of the retrieved and measured signal intensities look alike. The normalized cross-correlation of these images is shown in Fig. 4.6 (c). The peak value of the normalized cross-correlation is 0.97, indicating that the amplitude is very accurately retrieved.

When we record a transmission matrix, we determine a certain region of interest on the front surface of the sample and we scan a single focus on this region of interest. We record the fields transmitted through the sample in response to each distinct spatial position of the focus on the front surface of the sample. In total we collect on the order of 1000 fields consecutively. It is important that the foci probe the predetermined region of interest with consistent displacements. Thus, we require the setup to remain stable during the measurement time. Therefore, we monitor the stability of the setup during each measurement. After a set of interference patterns is recorded, we block the reference and record a set of intensity maps of the same fields whose interference with the reference were recorded. After the measurement is complete, we compare the retrieved and measured

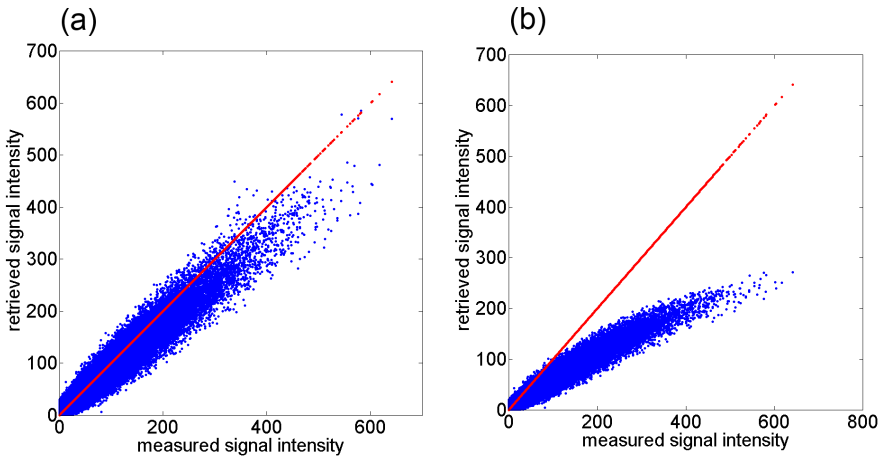

Figure 4.5.: Retrieved versus measured signal intensity. (a) Corrected for a constant MTF of 0.84. (b) Not corrected for MTF. Red dots: measured signal intensity versus itself. Blue dots: retrieved signal intensity versus measured signal intensity.

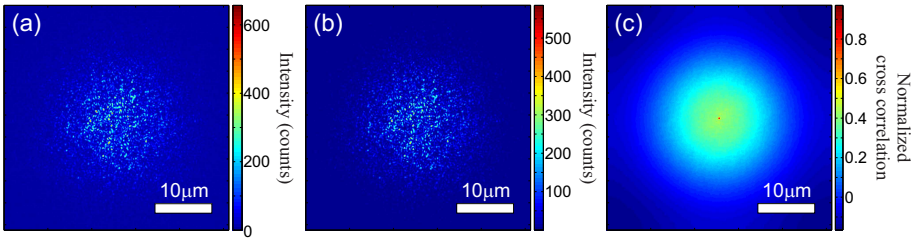

Figure 4.6.: (a) Measured (b) retrieved intensity of the signal. (c) The cross-correlation of the retrieved and measured signal intensities.

speckle intensities by taking their cross correlations. In most measurements the cross correlation between the retrieved and measured speckle intensities is greater than 0.9, and we reject the datasets that have cross correlation less than 0.7.

In this section, we have described how we retrieve the field using a method based on off-axis holographic detection. We have considerably improved the detection procedure to work with non-smooth reference and a modulation transfer function less than 1. We observe that the speckle intensity as retrieved from the recorded interference pattern is very similar to the speckle intensity recorded directly when the reference is blocked, and the correlation between the measured and retrieved intensities is 0.97, which is very high.

4.3. Data analysis

In this section, we describe the formation and analysis of a transmission matrix from a set of detected fields. We also give an analysis of sources of noise in a transmission matrix measurement and discuss their effect on our results.

We measure the transmission matrix of a certain region of the sample. To probe this region with incident fields, we define a basis to be diffraction limited spots, or Airy disks on the incident surface of the sample. For each incident-transmitted field pair, a single focus is created on the incident surface of the sample and the transmitted field is recorded. In a typical measurement, we record 1250 such fields from the probed area. The recorded fields have a spatial resolution higher than required. To reduce the computational demands of the data analysis, we reduce this resolution by grouping 4 pixels together. Also, the detection field of view is larger than necessary, so we define a new field of view, and reduce the size of the detected fields to the detection field of view by applying a sharp window in real space in the detection plane. After this point, the recorded fields are reshaped into column vectors and concatenated to obtain a matrix. We study this matrix by studying the distribution of its singular values.

4.3.1. Noise and errors in transmission matrix measurements

In an experiment, there are many factors resulting from field generation or field detection, leading to deviation of the measured transmission matrix from the ideal one. In most experiments reported so far, the noise contribution is completely ignored. In this section, we describe various noise contributions and discuss their effect on the measured singular values.

Laser noise The laser noise leads to a fluctuation of the total intensity in detected fields between consecutive measurements. Therefore we monitored the laser intensity fluctuations during the total duration of a transmission matrix measurement. The total duration of taking a set of measurements which can be used to construct a single transmission matrix is 23 minutes, which is doubled when the stability test, consisting of recording the intensity maps of transmitted fields, is also performed. The laser output intensity is monitored with a photodiode (Thorlabs SM1PD1A) and a low noise current amplifier (FEMTO DLPCA-200) with a sampling frequency of 2 Hz and a total measurement time between 1 hour and 3 hours. The upper bound for the laser intensity noise is found to be 5% peak to peak, including the measurement noise of the intensity monitor.

Non-orthogonality of the incident fields In an experiment, the measured transmission matrix is defined in the basis of pre-determined incident fields. It is a response matrix of the sample to the incident fields. Maxwell's equations lead to an uncertainty relation between the real space and momentum space so that a field cannot be sharply cut in both spaces. In a real experiment, the physical constraints are finite numerical aperture and finite field of view in the setup.

To span the detection field of view, which is sharply cut off in real space, basis functions are required that are sharply cut in real space. However, such fields cannot be generated due to the limited NA of the system. All of the generated fields are multiplied with the objective aperture function in momentum space, convolving the fields that probe the field of view with an Airy disk. Hence, an orthogonal and complete sampling of the field of view is impossible. There is either an oversampling of the field of view, where the complete field of view is probed with a redundancy in the probing, or there is undersampling, where the fields probing the field of view have negligible overlap but can not fully probe the field of view.

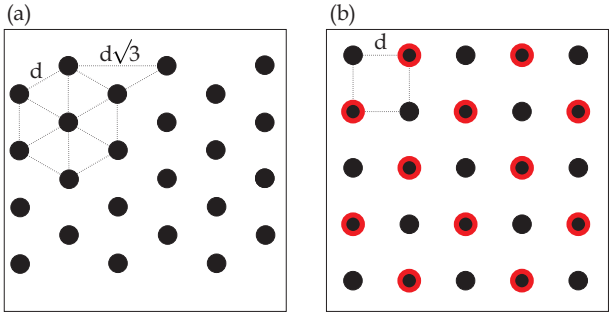

Figure 4.7.: (a) Hexagonal lattice. (b) Square lattice. Black dots: positions of the Airy disks. Red circles: positions of Airy disks after checkerboard filtering.

In our experiments, we use a two-dimensional raster scan of Airy disks as the incident field set. In principle, two Airy disks with the center of one being placed at the first zero of the other are orthogonal. However, in the 2D raster scan, only the nearest neighbor Airy disks can satisfy this condition, but not all other disks in the scan, leading to a finite overlap between verious incident fields. One can optimize the incident fields to obtain minimal overlap between fields while probing a maximal portion of the field of view. For this purpose, one can for instance scan the Airy disks in a hexagonal lattice, Fig 4.7 (a). In our experiments, we scanned the Airy disks in a square lattice for simplicity and in the cases when we found that there is a large amount of overlap, we removed a number of incident-outgoing field pairs from the original dataset using a checkerboard shaped filter applied to the 2D square lattice, Fig. 4.7 (b).

To find out how much overlap is present between generated incident fields, we measure the response matrix $\widetilde{T}_0$ of a bare, non-scattering substrate.[4] The effect of overlap on the singular values of $\widetilde{T}_0$ is found to be a variation of singular values around one and generation of a number of low singular values as the overlap is increased. This can be directly observed by comparing the singular values of $\widetilde{T}_0$ using densely sampled incident fields to the singular values obtained after applying the checkerboard filter. The singular value histograms of $\widetilde{T}_0$ under

[4]To construct $\widetilde{T}_0$, the sample is replaced by a standard glass cover slip and the usual field detection procedure is applied.

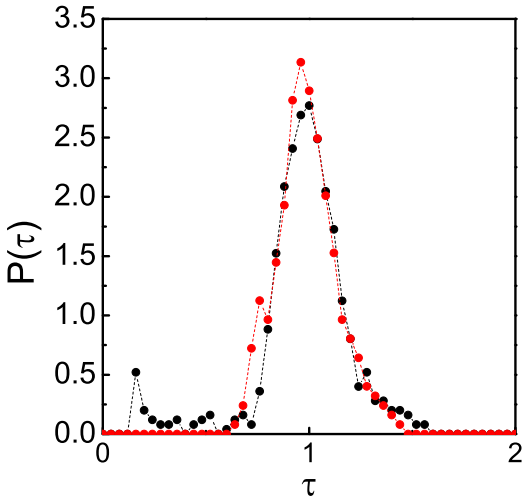

Figure 4.8.: Singular values of the response matrix $\widetilde{T}_0$ of a glass slide when dense and sparse sampling is used. Black dots: Singular value histogram for dense sampling. Red dots: Singular value histogram for sparse sampling.

dense and sparse sampling are shown in Fig. 4.8. In both cases, the histograms are dominated by a large peak near $\tau = 1$, which indicates that $\widetilde{T}_0$ is close to a unitary matrix. There is no peak at the low singular values for the sparsely sampled fields, as compared to the presence of a small peak observed in the case of densely sampled fields, indicating that there is significantly less overlap in the case of the sparsely sampled fields.

Fluctuations in the total intensity of generated fields It is observed that the total intensity in the generated incident fields is not the same between spots focussed on different positions inside the region of interest. Even in the case when there are no drifts or instabilities in the setup, the intensity is highest for the foci around the center and is reduced for the foci close to the edges of the area that is scanned on the front surface of the sample. This could be due to diffraction efficiency of the SLM and the response of the optics in the setup being different for different generated fields. In Fig. 4.9, the normalized average intensity of the focussed spot scanned over the front surface of a glass slide is shown. In this measurement, we observe a mean of 0.92, a standard deviation of 0.03 and a peak to peak variation of 0.14 for the fields transmitted through a bare glass slide. Since this contributes a root-mean-squared (rms) intensity fluctuation of only 3%, we do not compensate for this effect.

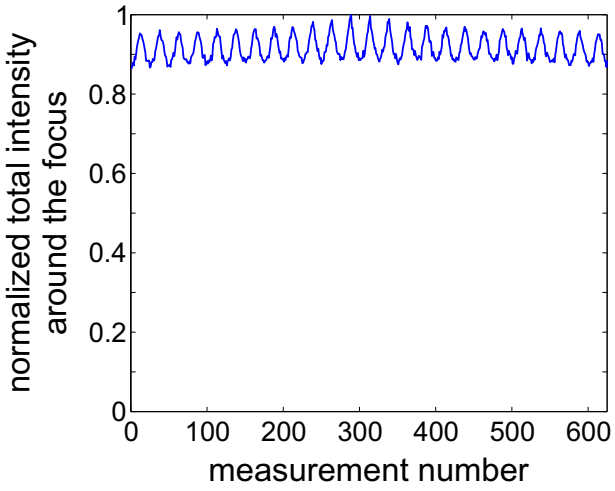

Figure 4.9.: Fluctuations of the intensity of the focus scanned over the pre-determined area on the front surface of a glass slide.

Additive detection noise In order to investigate how much additive noise is present in the detected fields, we performed a measurement where the signal arm is blocked so that only the reference is recorded. The recorded data are analyzed in the same way as the fields transmitted through the sample are analyzed. Since there is no signal, with this measurement we effectively retrieve only additive detection noise. The retrieved noise fields consist of complex numbers. When the histograms of the real and imaginary parts of these noise fields are plotted, they are found to have Gaussian distributions with mean of zero and standard deviations of 3.42 and 3.32 counts, respectively. In order to learn how the additive noise level compares to the detected signal level, we define a signal to noise ratio as

$$SNR = \frac{\langle \sqrt{\overline{I}(k)} \rangle_k}{\sqrt{\langle |E_{\text{noise}}(k,m)|^2 \rangle_{k,m}}}, \tag{4.14}$$

with,

$$\overline{I}(k) = \langle |E_{\text{signal}}(k,m)|^2 \rangle_m. \tag{4.15}$$

Here, the index k indicates different fields that are measured consecutively and index m indicates each individual pixel in a single field. The brackets $\langle . \rangle_k$, $\langle . \rangle_m$ and $\langle . \rangle_{k,m}$ indicate averaging over consecutive measurements, over all pixels in a single measurement and over all pixels in all measurements, respectively. In other words, $\overline{I}(k)$ is the average intensity in a single, k^{th} detected field and $\langle \sqrt{\overline{I}(k)} \rangle_k$ is averaged over consecutive detected fields. E_{signal} is a matrix of detected fields through the sample, with each column, k corresponding to a different field and the rows, m corresponding to pixels in each measurement. Similarly, E_{noise} is the matrix of detected fields when the signal arm is blocked. The signal to noise

ratio per 4 by 4 superpixel of the camera is found to be 12.3 on average for the datasets measured through GaP nanowires.

Phase noise In addition to the additive detection noise, there is phase noise on the measured transmission matrix. This noise is a combination of (i) variation of phase between rows of the transmission matrix, that is the same for each column, (ii) variation of phase between columns of the transmission matrix, that is the same for each row, (iii) random variations of the phase between rows and columns. For now, let us and assume we have only factors (i) and (ii). Then, the measured transmission matrix can be represented as

$$\widetilde{T} = \Phi T \widetilde{\Phi}. \tag{4.16}$$

Here $\widetilde{T}$ is a transmission matrix including the phase errors, Φ is the diagonal matrix representing the phase offsets between each row of the transmission matrix, $\widetilde{\Phi}$ is the diagonal matrix representing the phase offsets between each column of the transmission matrix and T is a transmission matrix with no phase errors. Φ and $\widetilde{\Phi}$ are unitary matrices. In this case, the singular values of $\widetilde{T}$ and T are identical, meaning that the noise terms represented by Φ and $\widetilde{\Phi}$ are irrelevant for the singular values of $\widetilde{T}$.

Term (iii) on the other hand, can lead to modifications of the singular value histogram of $\widetilde{T}$ as compared to the singular value histogram of T. To find the amount of random phase noise in detected transmission matrices, we investigate the same field being recorded consecutively. We investigate a dataset which was recorded under stable conditions and with the total intensity fluctuations in the retrieved fields being less than 3% peak to peak. We compare $|\langle E_1, E_k\rangle|$ to $|\langle |E_1|, |E_k|\rangle|$, with k the index indicating the k^{th} retrieved field, E_1 the first retrieved field and E_k the k^{th} retrieved field. $\langle ., .\rangle$ indicates inner product. The deviation between $|\langle E_1, E_k\rangle|$ and $|\langle |E_1|, |E_k|\rangle|$ gives us information on the amount of phase randomization during the recording of the dataset.

As seen in Fig. 4.10, the absolute value of normalized inner products of the field moduli decreases from 1 to 0.97 and the normalized inner products of the fields decrease from 1 to 0.93. From these results, we conclude that there is some randomization of the measured phase, reducing the inner products of the fields by about 4% below the inner products of the field moduli over a recording time of 400 fields, *i.e.*, over 15 minutes. This randomization in phase slightly modifies the singular values that are retrieved from the measured transmission matrix as compared to the singular values of an ideal transmission matrix, however, the phase randomization is found to be small.

Intensity noise in detection By comparing data taken over a period of several minutes we observed that the fringe visibility during our interferometric detection is not constant over time, which is most likely due to a time-dependence of the coherence length of the HeNe laser. This is studied by investigating the total intensity in the retrieved fields when the incident field on the sample is kept the same and the interference between the field transmitted through the sample and

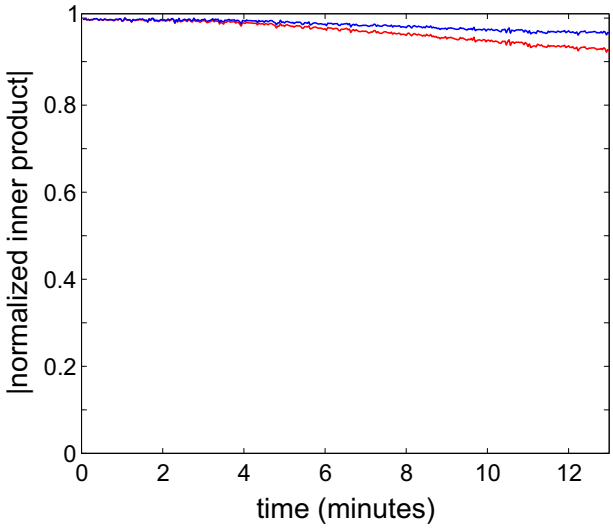

Figure 4.10.: Blue curve: Absolute value of inner product of each k^{th} field modulus with the 1^{st} field modulus, normalized to the inner product of 1^{st} field with itself. Red curve: Absolute value of inner product of each k^{th} field with the first field, normalized to the inner product of 1^{st} field with itself.

the reference beam is recorded over a 0.5 hour time interval.[5] When the fringe visibility is low, the retrieved signal intensity is reduced. In Fig. 4.11, the total retrieved intensity is shown in the field of view for the same field being sent through the sample over 0.5 hours. It is observed that the total intensity reveals a slow variation over the first 500 measurements and remains stable for the last 400 measurements. The fluctuations in total intensity are maximally 25% peak to peak, or about 10% rms.

Another test, in which we compared total intensities in the retrieved and measured speckle fields through a 6 μm thick layer of GaP nanowires reveal that the ratio between the total intensities in retrieved and measured speckle fields have fluctuations below 10% rms levels.

Total noise When all of the error sources described above are considered, it is seen that the dominant contribution to noise is the intensity fluctuations in the retrieved fields relative to the directly measured intensities, which is in the range of 10% rms.

[5] Root mean square fluctuations in the total intensity of recorded interference patterns is found to be 0.4%.

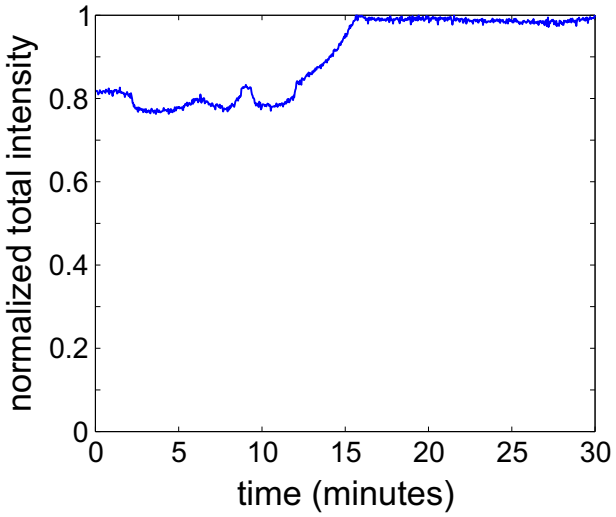

Figure 4.11.: The total intensity in retrieved field versus time, when the field incident on the sample is unchanged.

4.3.2. Effect of noise on the singular values of the transmission matrix

In order to understand if and how the singular value histograms are affected by the dominant noise source, we made several tests. Here, we first present a numerical test, where intensity fluctuations with varying peak to peak amplitude are introduced to an otherwise noise-free transmission matrix. For this purpose, a numerical transmission matrix is constructed having singular values obeying DMPK statistics [15, 16]. DMPK statistics is the theoretical prediction for the distribution of the singular values of a complete transmission matrix. In an experiment, a complete transmission matrix of the sample can not be recorded *e.g.* due to limited numerical aperture of the objective lenses leading to a limited information access. This limited information access is included in the numerical model by cropping the initially generated matrix.[6] In order to include intensity noise in the numerically generated matrix, the columns, the rows, or both the columns and rows of the matrix are multiplied by uniformly distributed random numbers with a peak to peak amplitude varying between 0% and 200%. Multiplying different columns of the numerically generated matrix with random numbers simulate intensity fluctuations between different recorded fields and multiplying rows of the numerically generated matrix with random numbers simulate intensity fluctuations within a single detected field; multiplying both rows and columns of the numerically generated matrix with random numbers simulate both fluctuations. In addition to the tests performed with numerically generated matrices, we present two tests performed using the experimental data. In the tests per-

[6] Detailed description of the numerical model is provided in Chapter 5.

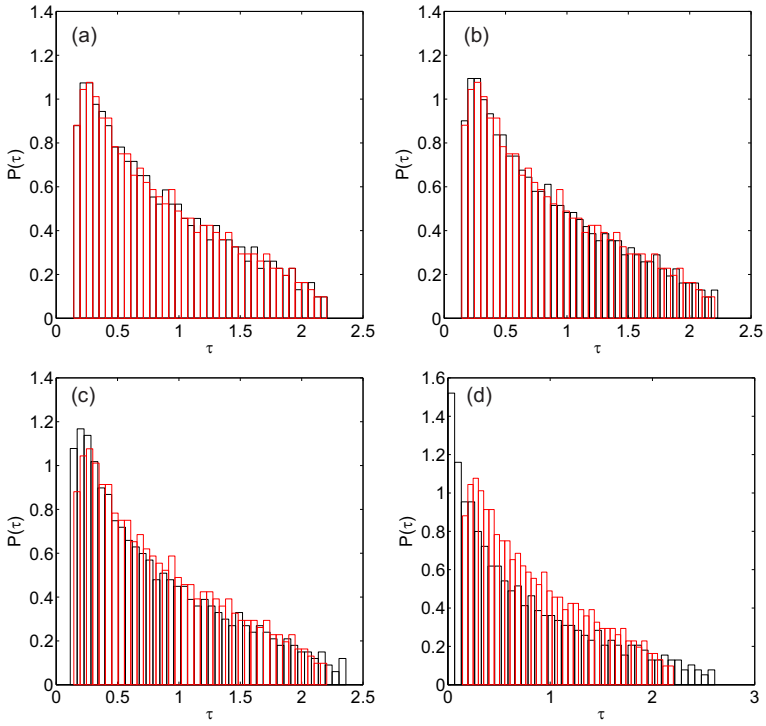

Figure 4.12.: Singular values of a noiseless, numerically generated matrix (red) and a matrix including random intensity noise (black), with (a) 20% (b) 40% (c) 100% (d) 200% peak to peak random fluctuations in the modulus of fields between columns of the transmission matrix.

formed with experimental data, we investigate the effect of fluctuations in the total retrieved intensity between different detected fields and the effect of additive random detection noise on the singular values of the transmission matrix.

In Fig. 4.12, the singular value histograms of a numerically generated matrix without intensity noise and the singular value histograms of a numerically generated matrix including intensity noise between its columns are shown. In Fig. 4.12 (a) and (b), the noiseless and noisy singular value histograms are shown for 20% and 40% peak to peak fluctuations in the field moduli. The singular value histograms are almost identical at these noise levels. In Fig. 4.12 (c) and (d), the noiseless and noisy singular value histograms are shown for high levels of fluctuations in the field moduli as 100% and 200% peak to peak. For these very high noise levels, which are about 8 times higher than the experimental noise levels for the 200% peak to peak amplitude noise, the noisy singular value histograms have a sharp peak and its tail extends further to high singular values compared to the histograms generated for low noise levels. From this test, we conclude that fluctuations in the total intensity of the detected fields have a small effect on the singular values of the transmission matrix, which can be neglected at our noise

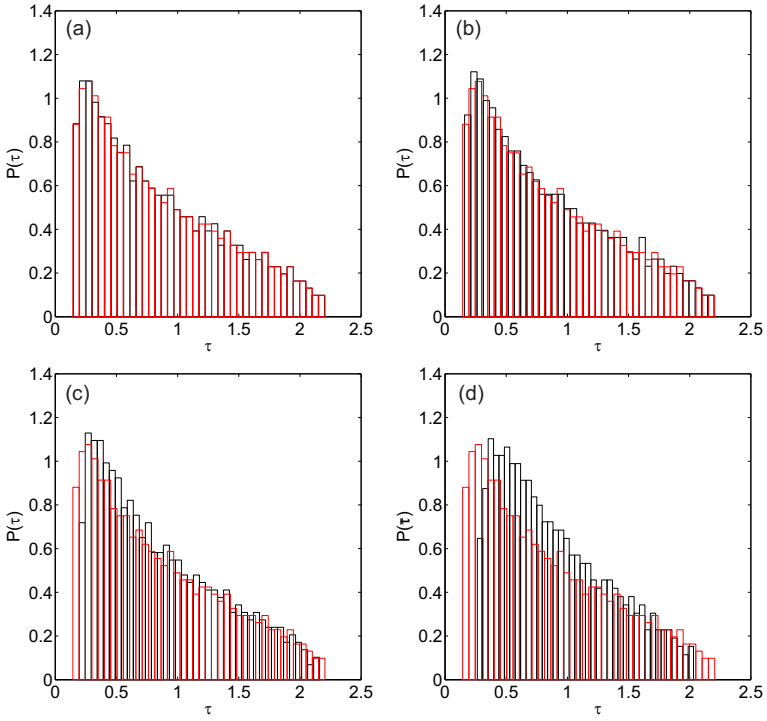

Figure 4.13.: Singular values of a noiseless, numerically generated matrix (red) and a matrix including random intensity noise (black), with (a) 20% (b) 40% (c) 100% (d) 200% peak to peak random fluctuations in the modulus of fields between rows of the transmission matrix.

levels of 10% rms.

In Fig. 4.13, the singular value histograms of a noiseless, numerically generated matrix and the singular value histograms of a numerically generated matrix including intensity noise between rows of the matrix are shown. In Fig. 4.13 (a) and (b), we show the noiseless and noisy singular value histograms for 20% and 40% peak to peak fluctuations in the field moduli, respectively. In Fig. 4.13 (c) and (d), we show the noiseless and noisy singular value histograms for the high noise levels of 100% and 200% peak to peak fluctuations in the field moduli. At these exaggerated noise levels the noise-free and noisy histograms again show discrepancies. In these cases, the peak of the histogram shifts towards higher singular values and becomes less sharp. From this test, we conclude that if the total intensity in each detected field is fixed and the intensities of individual speckles in each detected field fluctuate, the singular value histogram gets modified only at very high noise levels. Again, our experimental histogram is expected to be not significantly modified by this type of noise.

Finally, we made a test with intensity fluctuations between both rows and columns of the numerically generated matrix. First, the total intensity in the

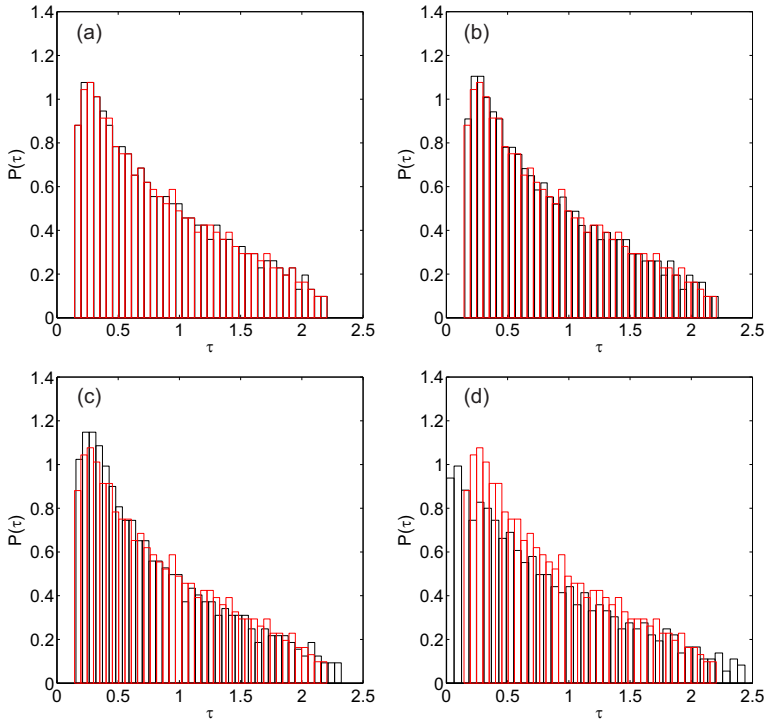

Figure 4.14.: Singular values of a noiseless, numerically generated matrix (red) and a matrix including random intensity noise (black), with (a) 20% (b) 40% (c) 100% (d) 200% peak to peak random fluctuations in the modulus of fields between different columns and within each column of the transmission matrix.

columns are randomized with varying amounts of peak to peak field modulus fluctuations. After this, fluctuations within each column are introduced. The results of the test are shown in Fig. 4.14. In Fig. 4.14 (a) and (b), the singular value histograms of a noiseless, numerically generated matrix and the singular value histograms of a numerically generated matrix including intensity noise between rows and columns of the matrix are shown for noise levels of 20% and 40% peak to peak field modulus. The noise-free and noisy singular value histograms are again almost identical at these noise levels. In Fig. 4.14 (c), the singular value histograms for a noise level of 100% peak to peak fluctuations in the field moduli is shown and the noise-free and noisy singular value histograms show some deviations. Only at the very high noise levels of 200% peak to peak in amplitude, as shown in Fig. 4.14 (d), the singular values are considerably affected by noise. The conclusion of this test is that the fluctuation of total intensity between the columns of the transmission matrix has a more dominant effect on the singular value histograms compared to the fluctuations of intensity within each column. In addition, the effects of intensity noise on the singular value histograms is

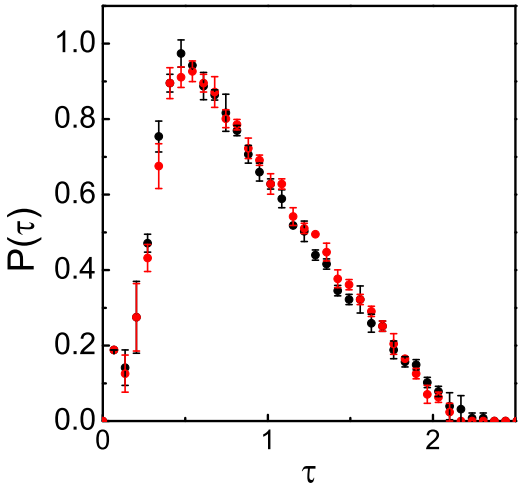

Figure 4.15.: Comparison of singular value histograms of experimental transmission matrices obtained when each field is normalized by total intensity in it (red data points) and when unnormalized (black data points).

significant only at exaggerated noise levels, as in the previous two tests.

An additional test to see whether fluctuations in the total intensity between different columns of the transmission matrix have an effect on the singular value histograms is made using the experimentally measured transmission matrices of the 6 μm thick layer of GaP nanowires. In this test, we remove the fluctuations of the total intensity between the columns of the recorded matrix by normalizing each column by its inner product with itself. Note that this way, the mesoscopic fluctuation signal in the total transmission through the sample in between different measurements is eliminated as well as the fluctuations due to noise. We show the singular values of the transmission matrices that are normalized and unnormalized in Fig. 4.15. It is seen from the figure that the two histograms overlap perfectly. It is concluded that the singular value histogram is not affected significantly by fluctuations in the total intensity between different detected fields, neither by noise nor even by the mesoscopic intensity fluctuations.

In addition to the tests for the effect of the intensity fluctuations on the singular values, we also performed a test of the effect of the additive noise on the singular values. The level of the additive noise is small compared to the multiplicative noise, so intuitively, one would assume that it can be ignored. However, the additive noise is of a different nature than the fluctuations of the total intensity between different recorded fields or the spatial intensity fluctuations within each field. The additive noise is a matrix of complex uncorrelated random variables that is added to the detected transmission matrix. One can intuitively see

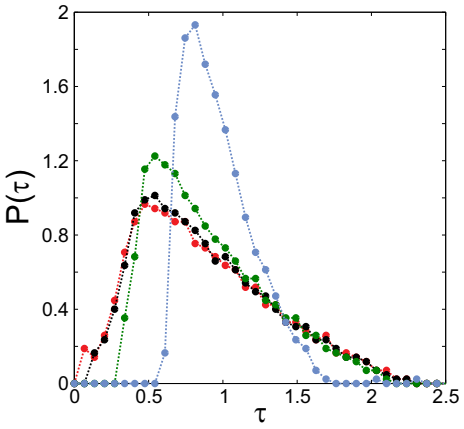

Figure 4.16.: Singular value histograms in the presence of various levels of additive noise. Red dots: Experimental singular value histogram. Singular value histograms when additive noise level is tripled: black dots; increased by 5 times: green dots; increased by 15 times: blue dots.

that at high levels of additive noise, we effectively have an uncorrelated random matrix. We make a test to see when the additive noise starts to affect the singular value histograms. For this test, we artificially added additive noise to a recorded transmission matrix, taken from Chapter 5. The singular value histograms obtained from this test are shown in Fig. 4.16. It is seen that up to an additive noise level of 3 times that of the experimental noise levels, the singular value histograms hardly change. As the artificially added noise level is increased, the peak of the singular value histograms becomes sharper and gradually shifts towards higher singular values. The histograms also have a narrower spread of singular values as the additive noise level is increased and starts to be reshaped into a Marcenko-Pastur probability density function, which is the singular value probability density function of an uncorrelated random matrix.

After an elaborate analysis of the noise terms, the dominant noise source in our experiments is found to be the fluctuation between total retrieved and measured intensities between different measurements and is found to be at 10% rms level. By numerical tests, the main conclusion is that at these noise levels, the singular value histograms are not significantly altered by the noise.

4.3.3. Effect of detection field of view on singular values

In addition to the experimental noise that can affect the results of the transmission matrix measurements, the procedures followed in the data analysis can also affect the outcome of the transmission matrix measurements. Here, we discuss how a chosen detection field of view can affect the singular values.

Since we deal with samples having an open geometry, we seemingly have freedom in terms of how to determine the field of view on the detection side. Suppose we choose a very small field of view, even smaller than the region of interest

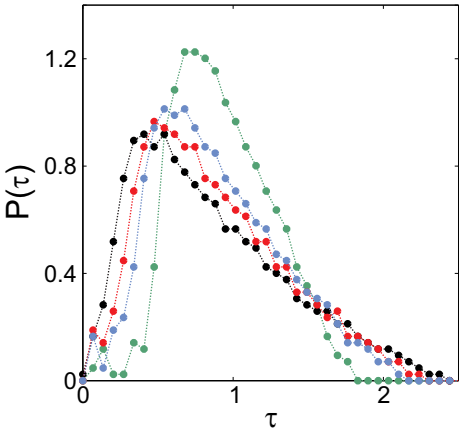

Figure 4.17.: The effect of detection field of view on singular values. Black histogram: 12 μm by 12 μm field of view. Red histogram: 13.9 μm by 13.9 μm field of view. Blue histogram: 16 μm by 16 μm field of view. Green histogram: 39.6 μm by 39.6 μm field of view.

within which the incident focus is scanned. Such a field of view would cut out a large part of the transmitted intensity and would lead to a spurious variation in the total detected intensity as large parts of the transmitted speckle field would sometimes fall outside the detection window. On the other hand, if we perform the data analysis using a very large field of view, we unnecessarily accumulate a large amount of additive noise, which modifies the shape of the observed singular value histograms.

In Fig. 4.17 we show the singular value histograms of a transmission matrix recorded using a 6 μm thick layer of GaP nanowires for various detection fields of view, of width 12 μm, 13.9 μm, 16 μm and 39.6 μm. We observe that the shape of the histogram depends significantly on the field of view. As the field of view gets smaller, the peak of the histogram tends to shift to lower singular values and the tail of the histogram extends further to higher singular values. This is consistent with the idea that at a large field of view more additive noise is sampled. Indeed, as the field of view is increased the histogram changes shape similarly to the trend shown in Fig. 4.16. In the data analysis procedure, we use a field of view equal to the area covered by the full width at half maximum of the intensity average of all outgoing fields on the rear side of the sample, making the field of view of the GaP nanowire samples 13.9 μm wide (also discussed in Chapter 5).

4.4. Conclusions

In this chapter, we have described the field generation and field detection methods that we use to measure transmission matrices. An improvement to standard off-axis holographic detection was described and the retrieved fields are shown to

correlate well with separate intensity measurements. We have also described the data analysis procedure and the information that we are seeking in the recorded transmission matrices, *i.e.*, the distribution of the singular values.

A noise analysis of the recorded transmission matrices is provided. It is observed that the dominant noise source in the recorded transmission matrices is the fluctuations in the total intensities of the retrieved fields as compared to directly measured fields. Numerical tests were performed to investigate the effects of this measurement noise on the singular values of the transmission matrices. It is observed that the noise levels we have in the experiment do not affect the overall shape of the singular value histograms. Using the apparatus and the data analysis procedure as described in this chapter, we can measure transmission matrices with many degrees of freedom and acceptable signal to noise ratio.

Bibliography

[1] L. J. Hornbeck, *From cathode rays to digital micromirrors: a history of electronic projection display technology*, TI Technical Journal **15**, 7 (1998). — p.46.

[2] C. Maurer, A. Jesacher, S. Bernet, and M. Ritsch-Marte, *What spatial light modulators can do for optical microscopy*, Laser Photon. Rev. **5**, 81 (2011). — p.46.

[3] A. P. Mosk, A. Lagendijk, G. Lerosey, and M. Fink, *Controlling waves in space and time for imaging and focusing in complex media*, Nat. Photon. **6**, 283 (2012). — p.46.

[4] E. N. Leith and J. Upatnieks, *Reconstructed wavefronts and communication theory*, J. Opt. Soc. Am. **52**, 1123 (1962). — p.47.

[5] M. Takeda, H. Ina, and S. Kobayashi, *Fourier-transform method of fringe-pattern analysis for computer-based topography and interferometry*, J. Opt. Soc. Am. **72**, 156 (1982). — p.47.

[6] T. Kreis, *Digital holographic interference-phase measurement using the Fourier-transform method*, J. Opt. Soc. Am. A **3**, 847 (1986). — p.47.

[7] T. Ikeda, G. Popescu, R. R. Dasari, and M. S. Feld, *Hilbert phase microscopy for investigating fast dynamics in transparent systems*, Opt. Lett. **30**, 1165 (2005). — p.47.

[8] C.-L. Hsieh, Y. Pu, R. Grange, G. Laporte, and D. Psaltis, *Imaging through turbid layers by scanning the phase conjugated second harmonic radiation from a nanoparticle*, Opt. Express **18**, 20723 (2010). — p.47.

[9] Y. Choi, T. D. Yang, C. Fang-Yen, P. Kang, K. J. Lee, R. R. Dasari, M. S. Feld, and W. Choi, *Overcoming the diffraction limit using multiple light scattering in a highly disordered medium*, Phys. Rev. Lett. **107**, 023902 (2011). — p.47.

[10] M. Kim, Y. Choi, C. Yoon, W. Choi, J. Kim, Q.-H. Park, and W. Choi, *Maximal energy transport through disordered media with the implementation of transmission eigenchannels*, Nat. Photon. **6**, 581 (2012). — p.47.

[11] M. Servin, J. Estrada, and A. Quiroga, *Advances in speckle metrology and related techniques* (Wiley-WCH, 2011). — p.47, 49.

[12] S. M. Popoff, G. Lerosey, R. Carminati, M. Fink, A. C. Boccara, and S. Gigan, *Measuring the transmission matrix in optics: An approach to the study and control of light propagation in disordered media*, Phys. Rev. Lett. **104**, 100601 (2010). — p.50.

[13] J. W. Goodman, *Introduction to Fourier optics* (Roberts & Company, Englewood, 2005). — p.50.

[14] J. C. Feltz, *Development of the modulation transfer function and contrast transfer function for discrete systems, particularly charge-coupled devices*, Optical Engineering **29**, 893 (1990). — p.50.

[15] O. N. Dorokhov, *On the coexistence of localized and extended electronic states in the metallic phase*, Solid State Commun. **51**, 381 (1984). — p.59.

[16] P. A. Mello, P. Pereyra, and N. Kumar, *Macroscopic approach to multichannel disordered conductors*, Ann. of Phys. **181**, 290 (1988). — p.59.

CHAPTER 5

Transmission Matrices of Strongly Scattering Random Photonic Nanowire Ensembles

5.1. Introduction

In this chapter, measurements are presented of optical transmission matrices of strongly scattering random photonic nanowire ensembles. Our measurements show correlations in the complex transmission matrices, as theoretically predicted for samples exhibiting a strong multiple light scattering [1]. An especially interesting aspect is the fact that we observe these correlations despite measuring a very small part of the transmission matrix. Using samples of different thickness but with otherwise similar properties we observe a strong dependence of correlations on sample thickness as expected from theory. In addition, we demonstrate a new approach to retrieve the scattering strength of the samples under study, using transmission matrix measurements along with numerical modeling.

An optical transmission matrix is a matrix describing the relation between the incident and transmitted fields of an arbitrary medium in a certain pre-defined basis. While the transmission matrix of a well-known optical element is a simple one, the transmission matrix of a strongly scattering medium is extremely complex [2]. While experiments that implicitly rely on measuring part of the transmission matrix of a random photonic medium have been carried out for decades [3–9], it is only recently that several optical and microwave experiments have demonstrated that large parts of the transmission matrix of a random photonic medium can be measured directly [10–14]. In the optical experiments, knowledge of the transmission matrix has been used for practical applications of focusing [10, 11, 15], sending an image [16], and enhancing the transmission [17] through a random photonic medium. In Ref. [18], incident wavefronts were carefully shaped such that elusive open transmission eigenchannels in a random photonic medium were accessed. In microwave experiments, explicit measurements of the transmission and scattering matrices have been used to confirm the predictions of random matrix theory for wave transport [1] through random quasi 1D waveguides [13, 14] and 2D chaotic microwave cavities [19, 20]. Recently, frequency-dependent transmission matrix measurements have been reported, which can extend the applications of optical transmission matrices to controlling light transport through random photonic media in space and time [21].

Knowledge of optical transmission matrices has proven useful since it contains the information on how a certain element in an optical setup, in our case a

random photonic medium, modifies the transmitted light and enables one to assign a desired functionality to the optical element. Besides these practical uses of optical transmission matrices, it has been proposed that one can use the transmission matrix to study the properties of the optical element itself [2, 10]. We are interested in light transport in three dimensional random photonic media, and so far no transmission matrix experiments have yielded information on the optical properties of 3D media. This leads to the main motivations behind this chapter: first motivation is to observe that measured transmission matrices have correlations. Achieving this, we deduce that sample information must be retained in the measured transmission matrix, bringing us to the second motivation, which is to investigate what type of sample information is retained in our transmission matrix measurements and to retrieve this information.

In Section 5.2, a description is given of the samples that are used and in Section 5.3 a brief description is provided of our experiment. Our results on the singular value histograms of measured matrices are described in Section 5.4. A description is given of the model that we implemented to predict the singular value histogram of an optical transmission matrix in Section 5.5. Finally, in Section 5.6, predictions of the model are compared with the singular value histograms obtained experimentally in order to estimate the optical properties of the samples under investigation.

5.2. Samples

Random photonic nanowire ensembles are interesting samples for our studies as they are reported to be extremely strongly scattering and already a thin layer scatters light multiply [22, 23]. Strong scattering makes the correlations in a transmission matrix more prominent. A thin sample makes the measurements and analyses relatively easy as compared to a thick sample since our samples have a slab geometry and light diffuses to a smaller area through a thin slab as compared to a thick one [24–26], reducing the problems associated with the open geometry of the sample.

The nanowires are grown using a metal-organic vapor epitaxy on a GaP (100) substrate [22]. GaP is a semiconductor with a very high refractive index of 3.32 at λ= 632.8 nm [27]. After being grown, the nanowires are pressed with a glass slide. During the pressing of the glass slide, long nanowires are broken and blend with the rest of the nanowires. Thus the nanowire ensemble becomes more disordered. The glass slide is left pressed onto the sample in order to protect the nanowires and to allow imaging by an immersion objective.

Samples similar to the ones used in this chapter were reported to have a transport mean free path as low as l_{tr}=0.20±0.02 μm at λ=632.8 nm [22]. A study conducted with similar samples showed that light transport through these samples has strong contributions from mesoscopic interference effects, and the transport takes place over only a few open transmission eigenchannels [23].

It was also reported that the diffusion through these samples is anisotropic [23]. The birefringence of similar GaP nanowire samples was studied previously and

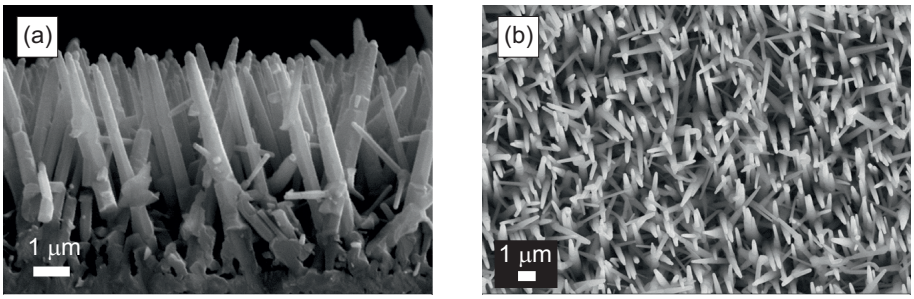

Figure 5.1.: Scanning electron microscope images of (a) Side view, (b) top view of a random photonic ensemble of GaP nanowires, before they are pressed with a glass slide.

was reported to be as large as $\Delta n = 0.209$ [28, 29].

By considering the range of possible values of the material parameters transport mean free path l_{tr} and effective refractive index n_{eff}, we expect kl_{tr} to be between 3.7 and 7.5. The parameter kl_{tr} indicates how strongly scattering a sample is, smaller kl_{tr} means stronger scattering (see Section 2.5, $S = 1/kl_{\mathrm{tr}}$). Here, we consider the l_{tr} values reported in Ref. [23] and n_{eff} values ranging from 1.5 and 2.3 as estimated from Bruggeman effective refractive index formula [30] with a filling fraction $44\% \pm 15\%$[1] for the GaP. The anisotropy of the samples is ignored in the calculation of n_{eff}.

We study samples with 1.6±0.2 μm and 6±0.5 μm thick layers of nanowire ensembles sandwiched between a GaP slab and a standard cover glass (a schematic is given in Fig. 5.7). Throughout this chapter, these samples are called the "thin sample" and the "thick sample", respectively. A scanning electron microscope (SEM) image of a similar thick sample before a glass slide is pressed on top is provided in Fig. 5.1. The side view is shown in Fig. 5.1 (a). Individual nanowires are resolved, which are up to 6.4 μm long with up to 500 nm diameter at their base and 300 nm at their tip. The top view is shown in Fig. 5.1 (b). While it is seen that some nanowires are randomly oriented with respect to the substrate normal, most nanowires seem to have a preferred orientation.

In Fig. 5.2, we show a map of the thick sample viewed with an optical microscope using (a) transmission illumination, (b) reflection illumination. The sample consists of several shards, as the gallium phosphide substrate is broken. Moreover, it is seen that the sample has different regions that look slightly different than neighboring regions but it is homogeneous within each region. Some regions look darker in transmission and brighter in reflection and *vice versa*. At certain regions, an air gap of 6±2 μm width is found between the nanowires and the glass slide. The thickness of the air gap is measured by alternately bringing the top of the nanowire ensemble and the bottom surface of the glass in focus. An air gap is undesired as it introduces an extra optical layer that complicates experiments and interpretation.

[1] Estimated from SEM pictures

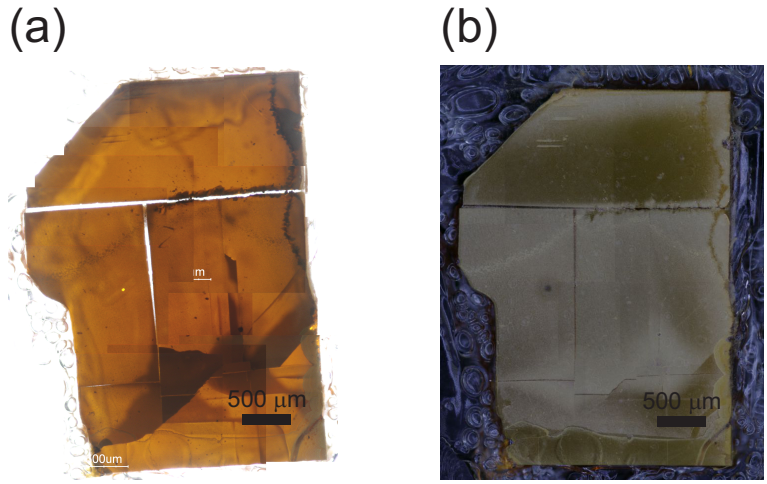

Figure 5.2.: (a) Transmission (b) Reflection image of the 6 μm thick sample captured with an optical microscope.

At other areas, we could not conclude on the existence of the air gap as it cannot be resolved using the refocusing method. This indicates that the gap is either thinner than the depth of field of the microscope objective (50×, 0.8NA), which is calculated to be 1.5 μm, or the nanowires even touch the glass. The measurements reported in this chapter are carried out on areas where no obvious air gap is found under the optical microscope.

An image of the sample captured in the experimental setup from the side of the glass slide is shown in Fig. 5.3. The figure shows the interface between the GaP nanowire ensemble and the glass slide. A high intensity region is shown of ≈25 μm diameter, corresponding to the area illuminated by a white LED in the setup. In the illuminated area, distinct shapes of individual nanowires are seen on the glass surface. However, occasionally, there are empty areas devoid of nanowires occupying several μm^2. The presence of regions devoid of nanowires is consistent with the hypothesis of an air gap being present along with several nanowires stuck on the glass in the areas where we carried out measurements even though with the refocussing method we could not detect a gap.

A momentum-space map, showing the root mean square (rms) field modulus versus the transversal wave vector, $\sqrt{\langle |E(k)|^2 \rangle}$, of fields transmitted through the thick sample is shown in Fig. 5.4. The data are averaged over 625 different incident fields (diffraction limited spots scanned over the front surface of the sample). As can be seen from Fig. 5.4 (a), the transmitted light is not uniform in momentum space. Cross-sections of the disk that is shown in Fig. 5.4 (a), taken along x- and y-directions are shown in Fig. 5.4 (b). There is a bright central region in momentum space, placed on top of a pedestal that has an rms field modulus less than half of the peak value. It is observed that the height of the pedestal is slightly different along x- and y-directions.

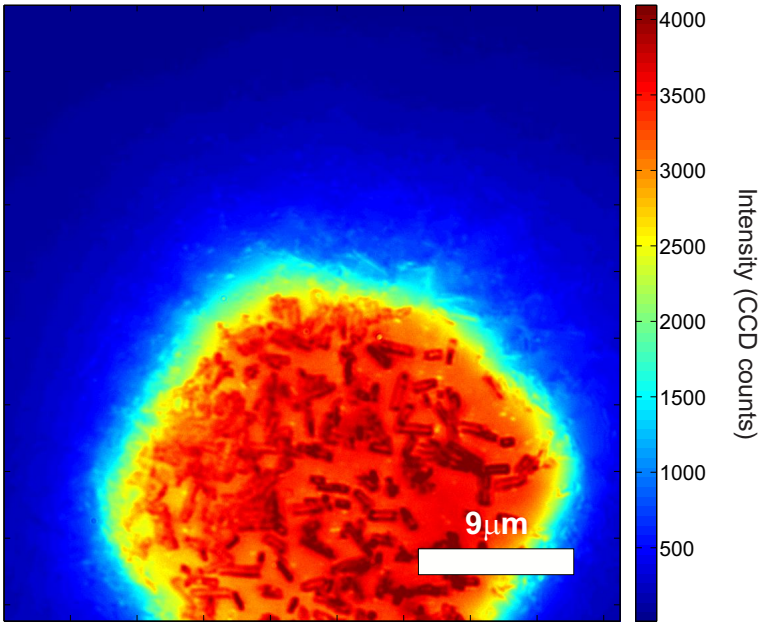

Figure 5.3.: Image of nanowire-glass interface of the thick sample taken *in situ* in our setup using a white LED.

Normally, light that exits a scattering sample approximately has a Lambertian distribution, and can be measured by escape function measurements, see, *e.g.* Ref. [31–34]. The observed momentum space profile deviates from a Lambertian profile, which can be explained if a thin air gap is present between the nanowires and the glass slide, with a small amount of nanowires stuck to the glass. The large wavevectors that can propagate in the nanowire layer due to its high effective refractive index become evanescent in the air gap and the transverse wavevectors are limited to a maximum of $k_0 = 2\pi/\lambda_0$, with λ_0 being the free space wavelength, in the air gap. After the air gap, the nanowires that are broken and stuck on the glass scatter a small portion of the light to transverse wavevectors with a large magnitude. The light scattered from the single layer of broken nanowires on glass is detected with our NA=1.42 oil immersion objective, giving rise to the pedestal.

For the fields transmitted through the thin sample, we observe the limitation of k_x/k_0 and k_y/k_0 to a maximum of unity as well. Moreover, while studying the thin sample in our setup, we could not see a sharp image of the nanowires on the detection side. This is attributed to the nanowires being placed at a distance from the glass slide that is larger than the working distance of the objective. These observations indicate that there is an air gap between the nanowires and the glass slide for the thin sample.

A momentum-space density map, showing the root mean square field modulus versus the transverse wave vector, $\sqrt{\langle |E(k)|^2 \rangle}$ of fields transmitted through the

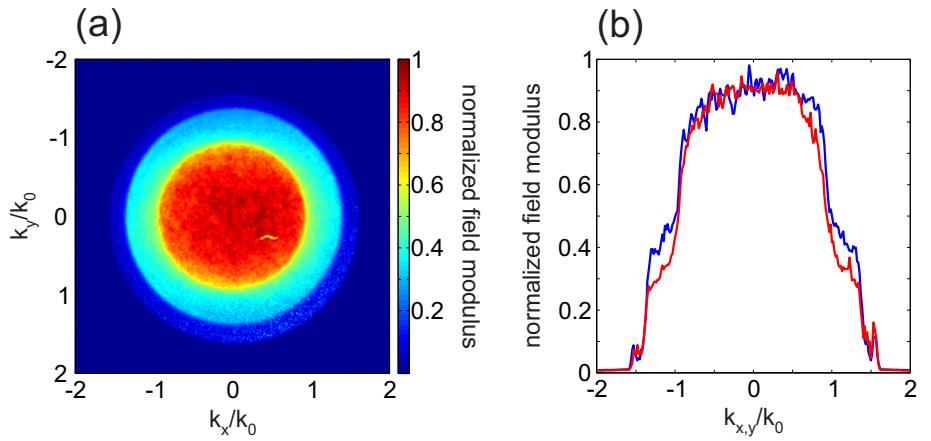

Figure 5.4.: (a) Momentum-space density map of root mean square fields, $\sqrt{\langle |E(k)|^2 \rangle}$ transmitted through the thick sample. (b) Cross sections of the image in (a) along x- (blue curve) and y- (red curve) directions.

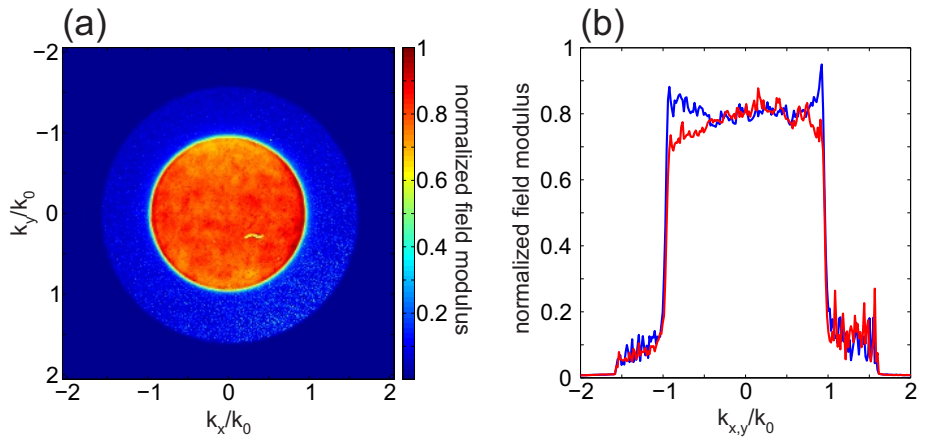

Figure 5.5.: (a) Momentum-space density map of the root mean square fields, $\sqrt{\langle |E(k)|^2 \rangle}$ transmitted through the thin sample. (b) Cross sections of the image in (a) along x- (blue curve) and y- (red curve) directions.

thin sample is shown in Fig. 5.5. The transmitted light is limited to a central region in momentum space. The low intensity pedestal that we see in Fig. 5.4 has a much lower intensity in the case of fields transmitted through the thin sample. This observation suggests that there is an air gap between the nanowires and the glass slide, limiting the detected transversal wave vectors to a maximum of k_0. The absence of the pedestal suggests that there are not many nanowires stuck to the glass surface.

5.3. Experimental method

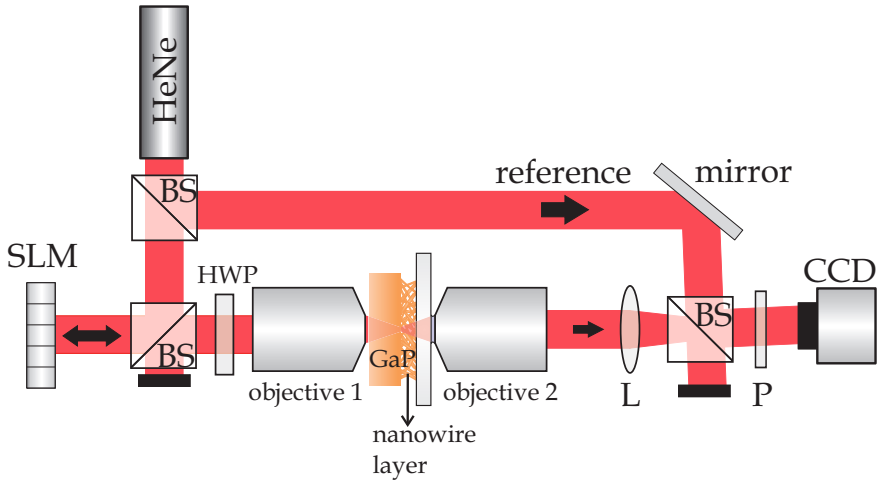

Figure 5.6.: Experimental setup. HeNe: laser. BS: 50:50 beam splitter. SLM: phase-only spatial light modulator. HWP: half-wave plate. GaP: sample substrate, nanowire layer: sample. Objective 1: 40X 0.6-NA objective. Objective 2: 60X 1.42-NA oil immersion objective. L: 500 mm focal length lens. P: polarizer. CCD: camera sensor.

The experimental setup is shown in Fig. 5.6. The light source is a helium-neon laser with a wavelength of 632.8 nm and an output power of 5 mW. Light from the laser is expanded and divided into two arms. Light in one arm is used as a reference field, light in the other arm, which is the signal arm, is reflected from a phase-only spatial light modulator (SLM, Holoeye Pluto). Light modulated by the SLM is passed through a half-wave plate (HWP), and focused on the interface of the nanowire layer with an infinity corrected objective. The sample is oriented with the GaP substrate on the incident side. In order to reduce the aberrations caused by focussing through the 300 μm thick GaP slab that has a thin layer of SiO_2, of approximately 300 nm thickness deposited on top, the illumination objective is chosen to have a moderate NA of 0.6. We use its cover glass correction ring to minimize the aberration that the GaP slab induces. The light transmitted through the nanowire layer is collected with an oil immersion objective (Olympus 60× NA=1.42). The sample surface is imaged onto the CCD camera with a calculated magnification of 167×. The light transmitted through the sample and the reference beam pass through a polarizer and interfere on the CCD sensor plane. We use off-axis holographic detection (see Chapter 4), which is a method based upon original proposals by Leith and Upatnieks [35], and a digital implementation by Takeda and coworkers [36]. With this method, a relative phase map between the signal and the reference fields is obtained in the detection plane. Throughout the text, when we describe a measured field, we refer to the retrieved map of field modulus and phase.

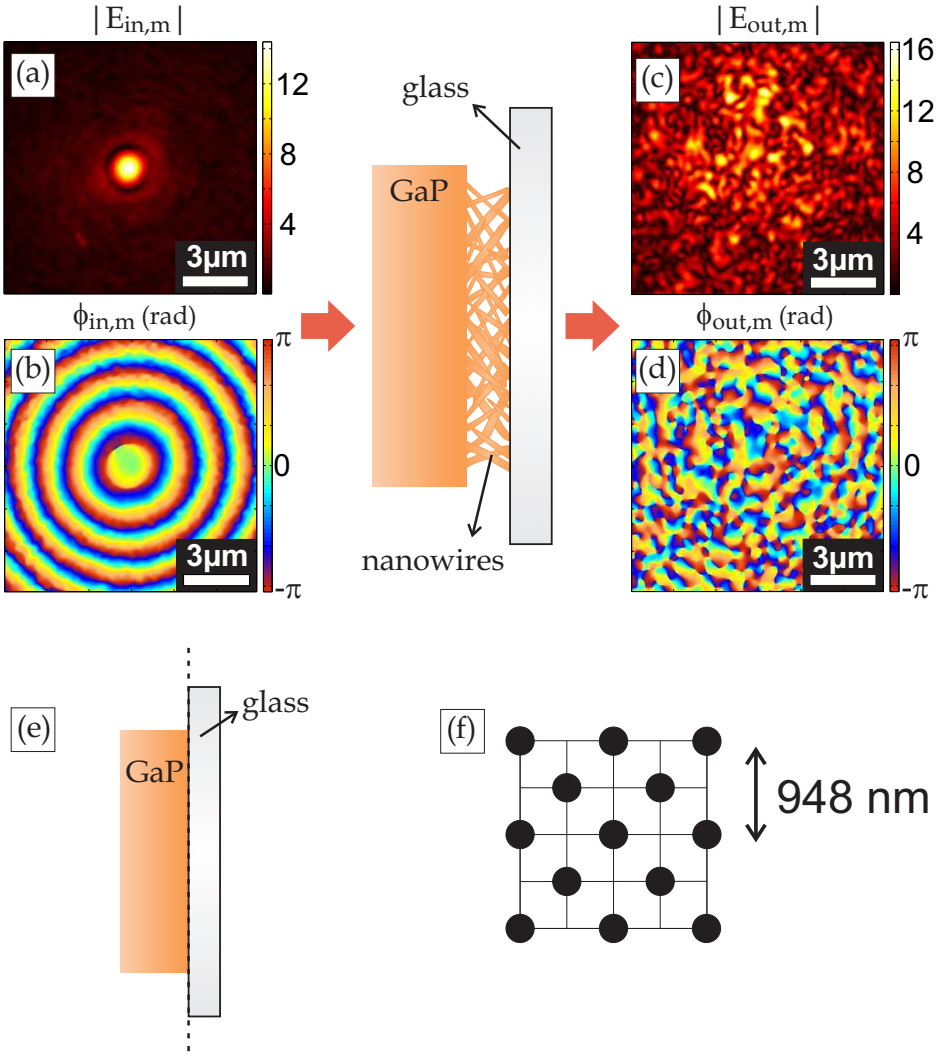

Figure 5.7.: Recording of the transmitted fields. (a) Amplitude and (b) phase map of a single incident field. (c) Amplitude and (d) phase map of the corresponding transmitted field. (e) GaP slab glued to a glass slide. (f) Schematic of the checkerboard filter applied to the incident fields. Black grid: original grid; the incident fields are focused on the corners of each square in the grid. Black dots: positions of incident spots that are kept in the analysis.

In Fig. 5.7 (a-d), we show an example of an incident-transmitted field pair, corresponding to the incident field being focused at the center of the probed area. $|E_{\mathrm{in},m}|$ and $\phi_{\mathrm{in},m}$ represent the modulus and the phase of the incident field, respectively. Here, m is an index used to label different incident fields, since the

transmission matrix is collected from hundreds of measurements, $|E_{\text{out},m}|$ and $\phi_{\text{out},m}$ represent the modulus and the phase of the fields transmitted through the sample. In order to record the actual incident fields at the front surface of the nanowire layer, we replace the sample with a blank substrate, which is a GaP slab glued to a glass slide, as shown in Fig. 5.7 (e). We focus the incident fields at the interface between the GaP slab and the glass slide and image this plane, which is represented by the dashed line in Fig. 5.7 (e), on to the CCD camera. In the field modulus map of the m^{th} incident field with $m = 157$ out of $m_{\max} = 313$, shown in Fig. 5.7 (a), a single bright spot at the center of the image is seen. The corresponding phase map, shown in Fig. 5.7 (b) has concentric rings of phase wraps covering the field of view, implying that the focus obtained through the GaP slab contains some residual aberrations even after the use of the correction ring on the objective. Maps of the modulus and of the phase of the corresponding fields transmitted through the nanowire layer are shown in Fig. 5.7 (c, d), respectively. They show a speckle field, with bright and dark spots in the map of the field modulus, Fig. 5.7 (c) and a phase that is constant within each speckle and that changes randomly between each speckle, Fig. 5.7 (d). By applying phase gradients on the SLM, we scan the incident spot over a 12 μm by 12 μm area on the front sample surface. In order to minimize overlap between incident fields, we apply a checkerboard filter to positions of the incident spots on the front sample surface, Fig. 5.7 (f). The spacing between the nearest neighbor spots is 673±25 nm, which is $1.06\lambda \pm 0.04\lambda$ and the spacing between the second nearest neighbor spots is 948±22 nm, which is $1.5\lambda \pm 0.04\lambda$. The size of the spot focussed on the front surface of the sample is ≈1 μm at FWHM. For each position of incident field, the corresponding transmitted field distribution is recorded and filtered as described in Section 5.4. The recorded two dimensional complex map of the m^{th} transmitted field is reshaped into one dimensional column vector $E_{\text{out},m}$. Finally, all $E_{\text{out},m}$ are concatenated to form a matrix $\widetilde{T}$.

The transmission matrix $\widetilde{T}$ is measured using far-field optics. The fields pass not only through the sample, but also through the optics before the sample, the GaP slab, the glass slide and the optics after the sample. Therefore, the measured matrix $\widetilde{T}$ is equal to the product $\widetilde{T} = T_2 T T_0$. Here, T is the transmission matrix of the sample, the singular values of which we are interested in. T_2 is the matrix that maps the fields at the rear surface of the sample to the detected fields, and T_0 is the matrix consisting of the fields at the incident surface of the sample.

Random matrix theory predicts the singular values of the sample transmission matrix T, which is not directly accessible. The statistical properties of $\widetilde{T}$ are identical to those of T if T_2 and T_0 are unitary. In order to investigate how far this is the case and to be able to compensate for any deviations, we measure a reference matrix $\widetilde{T}_0 = T_2 T_0$. $\widetilde{T}_0$ is the matrix that is recorded when the sample is replaced by a blank sample consisting of a GaP slab glued to a glass slide as shown in Fig. 5.7 (e). While it is conceivably possible to compensate for non-unitary matrices T_0 and T_2 by pseudoinversion [37], this procedure is very sensitive to phase drifts that may occur in between the measurements of $\widetilde{T}_0$ and $\widetilde{T}$. Instead, we adopt the significantly more stable procedure of taking $\widetilde{T}_0$ into account when

modeling the experiment.

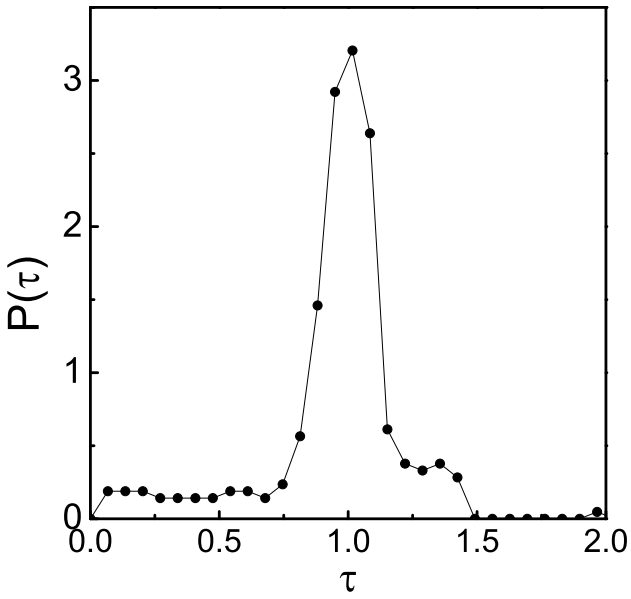

Figure 5.8.: Transmission singular value histogram of the reference GaP substrate without nanowires, normalized so that $\sqrt{\langle \tau^2 \rangle} = 1$. Black dots: measured singular value histogram.

In Fig. 5.8, we show the singular value histogram of $\widetilde{T}_0$.[2] The incident fields are focused on the interface between GaP and glass and the transmitted fields are recorded from the same plane. The singular value histogram shows a peak centered at the singular value of 1.02 with a full width at half maximum of 0.23. A small but significant variation to low singular values is observed, which is attributed to overlap between the fields transmitted through the reference sample. Two isolated singular values are observed at 1.96 and 2.91 (not shown). The two isolated high singular values are present in all sets of recorded matrices, and are found to be due to fields that are present as an offset in all recorded fields such as a small reflection from the front window of the SLM. Whereas we observe a sharp peak centered at 1 in the singular value histogram of the reference measurement, this peak has a finite width and is not a delta function. This finite width is attributed to an interplay of detection noise, fluctuations in the focussed spot intensity and spatial overlap between incident spots, *e.g.*, by

[2]The singular values are normalized so that their second moment is equal to 1 as is usually done when an *a-priori* normalization is not available [10, 38, 39]. The same normalization is performed in all of the presented singular value histograms in this chapter.

spherical aberration shown in Fig. 5.7. In addition, due to Fourier uncertainty relations, there is no basis of incident or outgoing modes that is simultaneously sharply defined in real space and momentum space, leading to either oversampling or undersampling of the probed area (see also Chapter 4).

5.4. Results

In this section, we describe the results of the measurements we performed with 1.6 μm and 6 μm thick layers of GaP nanowires. We measure the transmission matrices of both samples and investigate their singular value histograms.

According to random matrix theory of light transport, a random photonic medium has a large number of closed transmission eigenchannels that reflect light back and a small number of open transmission eigenchannels that completely transmit light. The number of open transmission eigenchannels in a random photonic sample is approximately Nl_{tr}/L, where N is the total number of transmission eigenchannels of the sample, l_{tr} is the transport mean free path, L is the thickness of the sample. If the number of open transmission eigenchannels is small in a sample, all of the transmitted fields in response to different incident fields are linear superpositions of a small number of independent fields and are correlated. An ensemble of nanowires with a thickness of 6 μm is about 20 transport mean free paths thick. The probed area of the sample is expected to have a number of open transmission eigenchannels between about 240 and 750, given the uncertainties in the material parameters l_{tr} and n_{eff}.[3] In our experiment, we probe the sample with 626 incident fields, which is in the same range as the number of open transmission eigenchannels. In this case, we expect to observe correlations in the fields transmitted through the thick sample. Moreover, we expect to be able to retrieve sample parameters by investigating the retrieved singular values.

In the case of the thin sample, the number of open transmission eigenchannels is estimated to be between 820 and 2550, by considering the previously reported range of l_{tr} and n_{eff}.[4] In this case, the number of open transmission eigenchannels is larger than the incident-transmitted field pairs that we excite and detect. So we expect to observe significantly less correlations in the transmission matrices of the thin sample as compared to that of the thick sample.

In this section, the experimentally obtained singular value histograms are compared to the Marcenko-Pastur density [40]. This density describes the probability density of singular values of a random, uncorrelated matrix. Therefore, comparing the experimental singular value histograms to the Marcenko-Pastur density provides a qualitative test for determining whether there are correlations in the measured transmission matrices.

The minimum and maximum singular values along with the shape of the Marcenko-Pastur density depend on the aspect ratio, γ, *i.e.* the ratio between

[3] To determine N, the sample is modeled as a waveguide 12.8-μm wide and 6-μm long and Eq. 5.5 is used.

[4] The sample is modeled as a waveguide 12.2-μm wide and 1.6-μm long.

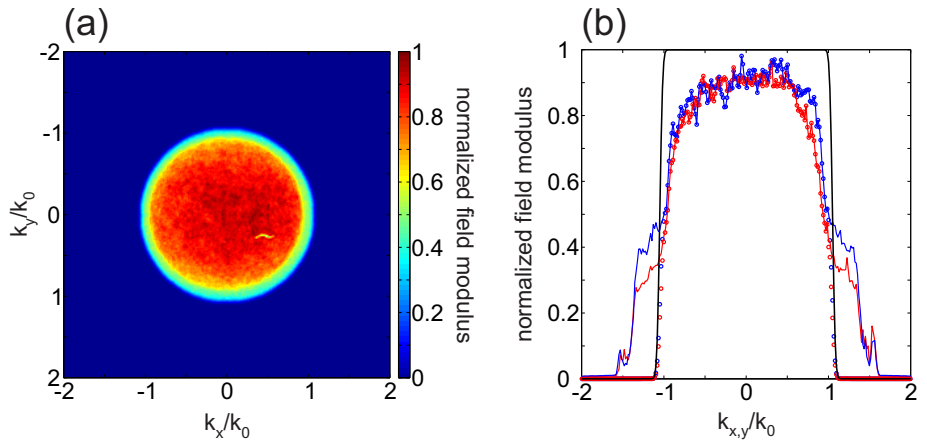

Figure 5.9.: (a) Momentum-space density map of root mean square fields, $\sqrt{\langle |E(k)|^2 \rangle}$ transmitted through the 6 μm thick layer of GaP nanowires after being filtered in momentum space. (b) Cross sections of the image in (a) along x- (blue curve) and y- (red curve) directions. Solid red and blue lines: original magnitude profile in momentum space; red and blue lines with open circles: momentum space magnitude profile after filtering; black solid line: cross section of the low-pass filter in momentum space.

the number of rows and the number of columns of the matrix, equal to

$$\begin{aligned} \gamma &= \frac{N_{out}}{N_{in}} \\ &= \frac{m_2}{m_1}, \end{aligned} \tag{5.1}$$

with m_2 and m_1 described in the same way as in our numerical model in Section 5.6. When $\gamma = 1$, the Marcenko-Pastur density looks like a quarter circle centered at the origin and extending up to a maximum singular value of 2. As γ increases, the shape of Marcenko-Pastur curve becomes more elliptical and narrower (see Chapter 2). In the limiting case of $\gamma \to \infty$, the Marcenko-Pastur curve becomes a delta function centered at 1.

Here, we compare all of our experimentally observed histograms to Marcenko-Pastur densities with the aspect ratios γ determined by the number of accessible incident and outgoing modes in our setup. Therefore, γ is not a freely adjustable parameter and has the value $\gamma = 2$ for the thick sample and $\gamma = 1.87$ for the thin sample.

5.4.1. Thick sample

As seen in Fig. 5.9 (b), the fields transmitted through the thick sample have a pedestal and a bright center region on top of this pedestal in momentum space. In order to have a well-defined field distribution in momentum space independent

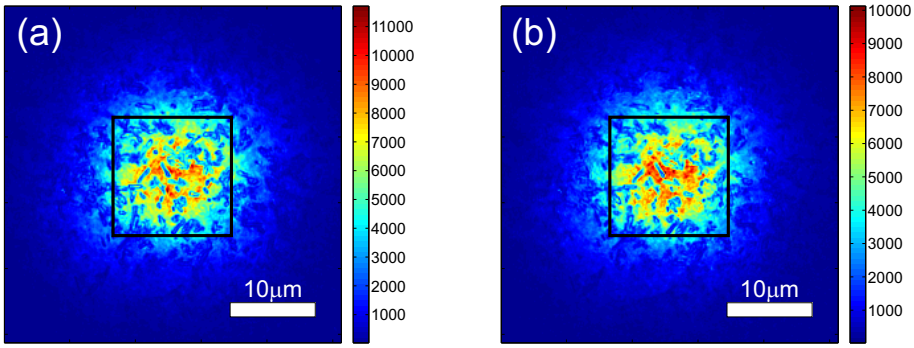

Figure 5.10.: Average intensities of 313 fields transmitted through 6 μm thick layer of GaP nanowires. (a), (b) H and V polarized incident fields.

of the presence of an air gap between the nanowires and the glass slide, we apply a low-pass filter in momentum space to each measured field. The momentum-space density map of rms fields obtained after applying a low-pass filter is shown in Fig. 5.9 (a). A disk-shaped bright region is seen. The rms field modulus drops to half of its maximum value at $k_x = 1$ and $k_y = 0.95$. The cross-section of the disk in Fig. 5.9 (a) is shown in Fig. 5.9 (b), along with the cross-section of the applied filter. It is seen that the low intensity pedestal is removed after applying the low-pass filter.

After filtering in momentum space, the fields are inverse Fourier transformed into real space to form the transmission matrix. We choose a field of view in real space, and consider the fields that stay within the field of view. In order not to accumulate unnecessary CCD detection noise while keeping a reasonable amount of intensity within the field of view, we choose a field of view that has a width equal to the full width at half maximum (FWHM) of the total intensity pattern of all detected fields. The total intensity pattern and the corresponding field of view for a dataset is shown in Fig. 5.10. The total intensity map is bright in the center and gets dimmer towards the edges due to diffusion. The nanowires that are stuck on the glass are clearly seen as the shadows in the intensity map. The field of view is indicated by a black square in Fig. 5.10 and has a width of 13.9 μm.

The singular value histogram of $\widetilde{T}$ is shown in Fig. 5.11. Its normalized singular values are observed to lie between 0.04 and 2.3. The singular value histogram is asymmetric with its peak at $0.49^{+0.06}_{-0.05}$.[5] To test whether the observed singular value histogram is consistent with an uncorrelated random matrix, the experimentally obtained singular value histogram is compared with the Marcenko-Pastur density [40], taking into account the dimensions determined by

[5] A 5^{th} order polynomial is fitted to several bins with highest counts. The peak is determined as the peak of the fitted function. The error margin in peak position is taken as the abscissa corresponding to ordinates with a value within a σ from the peak value. σ is the average standard deviation in the experimental histogram. The same procedure is applied for all histograms in this chapter.

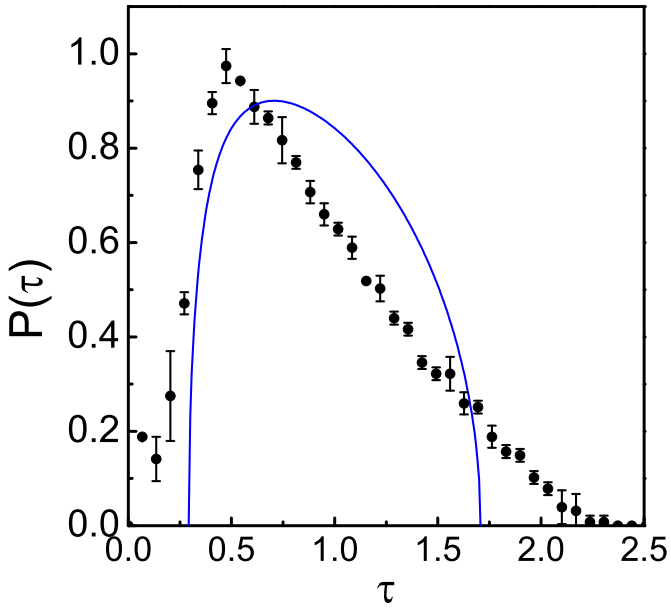

Figure 5.11.: Normalized singular value histogram of the transmission matrix of the thick sample, normalization factor=$\sqrt{\langle \tau^2 \rangle}$. Black dots: mean values, errorbars: standard deviation of the normalized counts in the singular value histograms of three different transmission matrices. Solid curve: Marcenko-Pastur density, with $\gamma = 2$.

the number of accessible incident and outgoing modes in our experimental setup. The Marcenko-Pastur density lies between $\tau = 0.29$ and $\tau = 1.7$ and has the shape of a distorted ellipse. It is seen that the experimentally obtained singular value histogram deviates strongly from the Marcenko-Pastur density in terms of its width and shape. The experimental histogram has a sharper peak and to the right of the peak, the histogram initially has a fast decrease in the histogram bin counts that later becomes a slow decreasing tail extending up to a singular value of 2.3, whereas the Marcenko-Pastur density has a slow decrease around the peak, that becomes a sharp decrease at high singular values. This deviation is an experimental evidence of correlations in an optical transmission matrix, which is reported here for the first time.

5.4.2. Thin sample

In order to be consistent with the analysis of the thick sample data we apply the same filter that is applied to the fields transmitted through 6 μm thick sample.

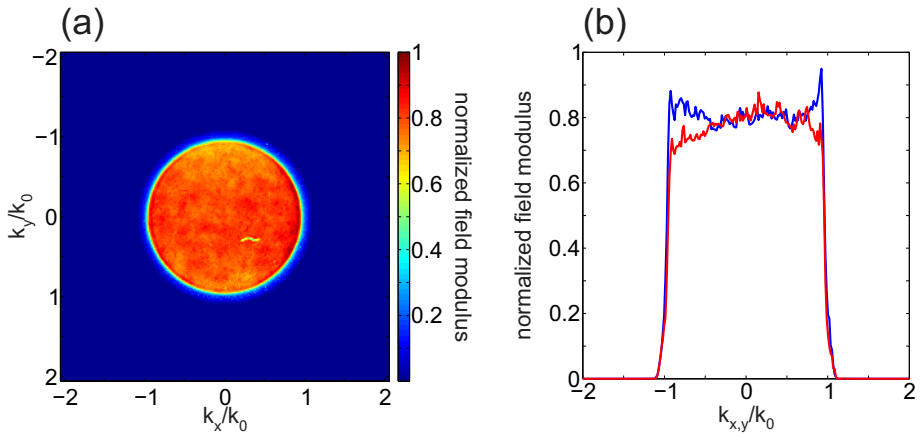

Figure 5.12.: (a) Momentum-space density map of root mean square fields, $\sqrt{\langle |E(k)|^2 \rangle}$ transmitted through the 1.6 μm thick layer of GaP nanowires after being filtered in momentum space. (b) Cross sections of the image in (a) along x- (blue curve) and y- (red curve) directions.

Applying this filter also removes the small artifact that is observed between $k_{x,y} = k_0$ and $k_{x,y} = 1.5k_0$.

In Fig. 5.12, we show the momentum-space density map of fields transmitted through the thin sample after the low-pass filter is applied. A bright disk with a sharp cut-off is seen in the density map shown in Fig. 5.12 (a). The cross-section of the density map is shown along the x- and y-directions in Fig. 5.12 (b); a sharp cut-off is seen in both directions. As can be seen from comparison of Fig. 5.5 with Fig. 5.12, the filtering only removes the small pedestal and does not affect the momentum space profile of the transmitted fields.

In Fig. 5.13, the average intensities of detected fields are shown. Similar to the procedure followed for the thick sample, an area that has boundaries at the FWHM of the average intensity of all detected fields is determined and is indicated by the black square. In this case, it has a width of 12.4 μm. The incident fields are scanned in the same manner as the 6 μm thick sample measurements. Since the sample is only $\approx$1.6 μm thick the square shape of the area over which the incident fields are scanned is distinguishable.

In Fig. 5.14, we show the normalized singular value histogram of the thin sample transmission matrix. In this case, the results are obtained from a single data set, since the other datasets were later found to be measured under unstable conditions, although they show very similar results. The experimentally obtained singular value histogram is compared with the Marcenko-Pastur density. The experimental singular value histogram is found to lie between the histogram bins of 0.07 and 1.97, whereas the Marcenko-Pastur density lies between the singular values of 0.27 and 1.73. The shape of both histograms are similar around the peak, with a slow decrease to the right of the peak and a fast decrease to the left of the peak. There are discrepancies between the two histograms at the high and low

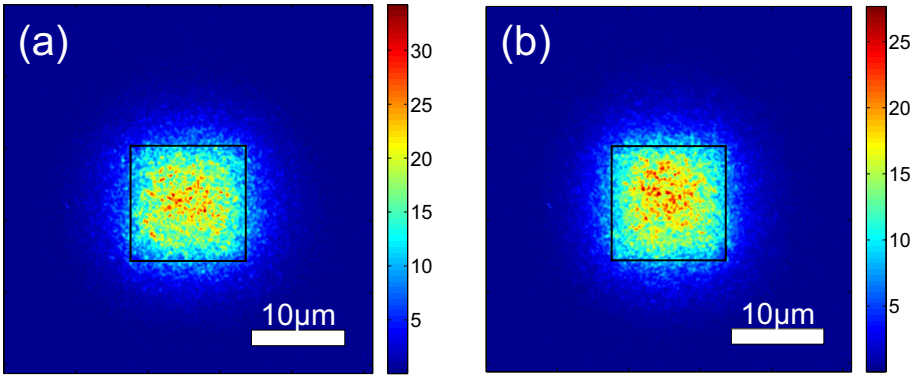

Figure 5.13.: Average intensities of 625 fields transmitted through 1.6 μm thick layer of GaP nanowires. (a), (b) H and V polarized incident fields

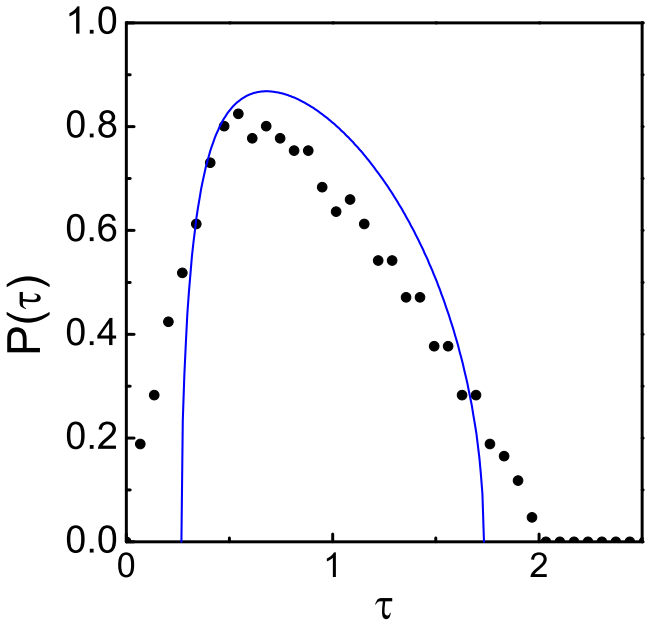

Figure 5.14.: Black dots: Normalized singular value histogram of the transmission matrix of the thin sample, normalized by $\sqrt{\langle\tau^2\rangle}$. Solid curve: Marcenko-Pastur density, with $\gamma = 1.86$.

end of the histograms, with the experimental histogram showing a wider spread of the singular values. The discrepancies are small compared to the discrepancies

observed in the case of the thick sample. It is seen that the measured transmission matrix of the thin sample is approximately an uncorrelated random matrix.

From a comparison of the thick and thin sample data, we observe that the singular value histograms obtained from the transmission matrices of the two samples are considerably different. The 6-μm thick sample shows pronounced correlations, whereas correlations are not evident in the transmission matrices of the thin sample. This confirms our expectations that the thick, strongly scattering sample has only a small number of open transmission eigenchannels, whereas the thin sample has more open transmission eigenchannels and displays less correlations.

5.5. Model

It is seen that the Marcenko-Pastur theory cannot be used to describe transport through the thick nanowire sample. Therefore, we have developed a new model that we use to predict the singular value histograms to be observed from the transmission matrix measurements of our samples. In this model, we assume a DMPK probability density function (see Chapter 2) [1, 41, 42] for the transmission coefficients of the transmission eigenchannels. The singular value density of the model transmission matrix is modified by experimental conditions such as limited information access, noise and field generation limitations.

Forming the model transmission matrix consists of three steps:

Step 1: We model the ideal transmission matrix for assumed sample parameters. In our model, we start by generating matrices of size N by N, having singular value densities as obtained from the bimodal probability density function predicted by Dorokhov [41]. The size of the matrix is chosen to be N=8000 by 8000 in order to use a large matrix while keeping computational constraints in mind. The material parameters enter the model through the average transmission, which is expressed in diffusion theory as

$$\langle T \rangle = \frac{z_{\mathrm{inj}} + z_{e1}}{L + z_{e1} + z_{e2}}. \tag{5.2}$$

Here, z_{inj} is the diffuse injection depth (see Chapter 2), z_{e1} and z_{e2} are the extrapolation lengths on incident and exit facets of the sample [43, 44]. When a plane wave is incident on a slab $z_{\mathrm{inj}} = l_{\mathrm{tr}}$ [45, 46]. In our case, light is focused on the front surface of the sample, with a 0.6 NA objective. In this case, z_{inj} can still be approximated to be equal to l_{tr}, giving a total transmission

$$\langle T \rangle = \frac{l_{\mathrm{tr}} + z_{e1}}{L + z_{e1} + z_{e2}}. \tag{5.3}$$

The description of the sample is simplified to a waveguide geometry with no loss. In reality, the sample has a slab geometry, so the fields are not confined in the lateral dimensions. Unfortunately there is presently no theory that permits us to incorporate exactly the effects of this lateral spreading. Still, we see that

modeling the sample as a waveguide is accurate enough to model our experiments. The cross-sectional width of this waveguide is taken as the average of the widths of the probed area on the incident surface of the sample and the area covered by the FWHM of the diffuse light.

Step 2: We take into account the limited access to the full transmission matrix of a sample in an experimental setup. The DMPK theory describes the singular value density of the full transmission matrix of the sample, however, it is well known that a partial matrix has a different singular value density [47, 48]. Due to the limited numerical apertures of our optics and the sampling density we use in the experiment, we effectively have access to only a part of the matrix. We model this limited information access by cropping the transmission matrix generated at the end of step 1. The columns of the transmission matrix represent different detected fields in response to different incident fields. Their number is determined by how many incident fields we send to our sample. Since the number of incident fields that are used in the experiment is smaller than the number of transmission eigenchannels, we need to reduce the number of columns of the model transmission matrix that is obtained at the end of step 1 by multiplying it by "m_1"

$$m_1 = N_{\text{in}}/N_{\text{channels}}, \tag{5.4}$$

where, N_{in} is the number of incident fields in an experiment and N_{channels} is the number of transmission eigenchannels of the waveguide that is used as the representation of our slab-type sample. N_{channels} is found using [2]

$$N_{\text{channels}} = \frac{2\pi A n_{\text{eff}}^2}{\lambda^2}, \tag{5.5}$$

where, A is the area of the waveguide, λ is the free space wavelength, n_{eff} effective refractive index of the scattering sample. The factor of 2 accounts for two orthogonal polarizations. On the exit side, the number of modes that can be detected is determined by the detection numerical aperture. As shown in Section 5.4, the detection numerical aperture, $\text{NA}_{\text{det}} = 1$. In this case, the number of modes that can be detected, N_{det} is

$$N_{\text{det}} = \frac{\pi A \text{NA}_{\text{det}}^2}{\lambda^2}. \tag{5.6}$$

The factor of 2 is not applied in N_{det} since the detection is performed for single polarization. In the model, we reduce the number of rows by multiplying the initial number of rows by m_2,

$$\begin{aligned} m_2 &= N_{\text{det}}/N_{\text{channels}}, \\ m_2 &= \text{NA}_{\text{det}}^2/2n_{\text{eff}}^2. \end{aligned} \tag{5.7}$$

Step 3: In the third step, we consider other experimental factors than cropping that deviate from an ideal case. For example, the generated incident fields may be oversampling the probed area. Also in an experiment there is noise. In order to account for these effects, we multiply the matrix that we obtained at the end of step 2 by a matrix M_0 that has the same singular value histogram

as $\widetilde{T}_0$, as is explained in Section 5.3. Effects of the overlap between different incident fields and the multiplicative noise, due to fluctuations in laser power, varying diffraction efficiency of the SLM for different phase gradients and the fluctuations in the coherence length in the laser output are included in the model via multiplication by M_0. Additive detection noise is found to be small compared to the multiplicative noise component and is therefore not included in the model.

The described approach allows us to generate singular value histograms that include the basic physical effects as well as the characteristics of our measurement apparatus. The results of the model can be compared directly to the experimental results. Now we investigate the result of the model for an *a priori* likely choice of parameters $l_{\mathrm{tr}} = 0.3$ μm and $n_{\mathrm{eff}} = 2.25$. For this effective refractive index, the extrapolation lengths on incident and exit sides of the sample are [44],[6]

$$z_{e1} = 0.78 l_{\mathrm{tr}} \tag{5.8}$$

$$z_{e2} = 7.39 l_{\mathrm{tr}} \tag{5.9}$$

The long extrapolation length on the exit side of the medium results from the high contrast between the effective refractive index of the nanowire layer and air. Similarly high extrapolation lengths have been reported before for the porous GaP samples [33, 49]. The average transmission $\langle T \rangle$, in turn, is calculated to be 6.3%. Taking into account the filtered momentum space distribution cropped to $k = k_0$ in the detection procedure, the cropping ratio of the matrix on the detection side becomes

$$\begin{aligned} m_2 &= \frac{1}{2}(1/2.25^2) \\ &= 0.1 \end{aligned} \tag{5.10}$$

In order to find the cropping ratio on the incident side, m_1, we consider the area probed by the incident spots, *i.e.*, $(12\ \mu\mathrm{m})^2$ and the area that the diffuse spot extends to on the rear side of the sample, which, using diffusion theory, is found to be $(13.6\ \mu\mathrm{m})^2$ at full width at half maximum of the intensity. The area of the waveguide that models our sample is then taken to be $(12.8\ \mu\mathrm{m})^2$. Such a waveguide with $n_{\mathrm{eff}} = 2.25$ has 13000 modes. We probe 626 modes out of 13000 modes, so we find that m_1=0.05.

In Fig. 5.15, the singular value histograms obtained from the model are compared to the experiments. Both the model and the experimental histograms are asymmetric in shape with a sharp rise at low singular values to reach a peak at a singular value of $0.40^{+0.09}_{-0.06}$ for the model, in good agreement with $0.49^{+0.11}_{-0.08}$ for the experiment. After the peak, both histograms decrease in a slightly concave manner, with the experimental histogram having a higher slope, and reach zero counts after the histogram bin centered at τ=2.3. It is also seen that bin

[6] The extrapolation lengths depend on the relative refractive indices of the sample and the media in its surroundings. Here, GaP is the medium on incident side, determining z_{e1} and air is the medium on the exit side, determining z_{e2}.

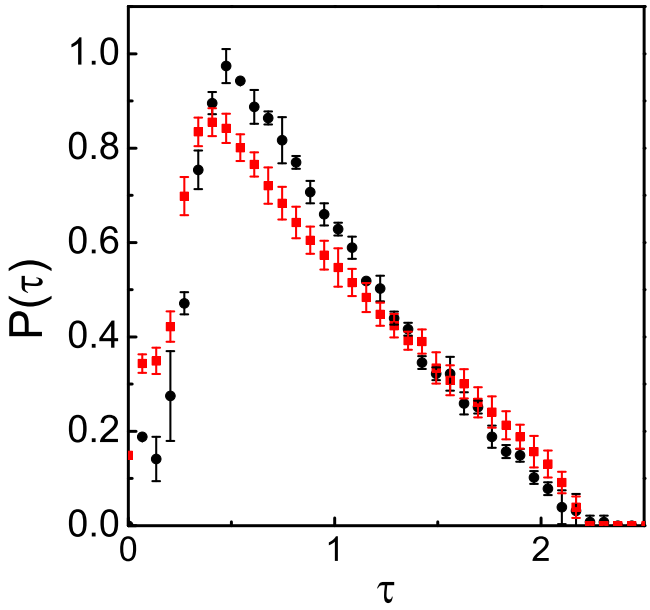

Figure 5.15.: Normalized singular value histograms obtained from the model and the experiment. Black dots: mean values, black errorbars: standard deviation of the normalized bin counts in 3 experimental singular value histograms. Red squares: mean values, red errorbars: standard deviation of the normalized bin counts in singular value histograms obtained from 20 runs of the model with independently generated random matrices.

counts around the peak is lower in the model histogram compared to the experimental histogram. The good agreement of the model and the data clearly shows the model captures the essential physics and that slab geometry samples are within reach of being modeled using DMPK theory. This observation, agrees with Nazarov's work [50], and it is remarkable as light propagation in slabs can be quite different from the waveguides that DMPK theory was developed for.

5.6. Retrieving sample parameters by comparing the model and the experiment

We have shown in Section 5.4 that the thick sample transmission matrix displayed correlations. Now, we focus our attention on whether we can retrieve information about the thick sample that is studied and what type of information we can retrieve. We aim to retrieve the sample parameters by comparing the sin-

gular value histograms obtained from our model to the singular value histograms obtained from the experiments. In this section, we explain how we make this comparison and discuss the sample parameters that we retrieve.

In order to retrieve sample parameters from our measurements, we make a fit of the mean singular value histogram obtained from the model to the mean experimental singular value histogram, using l_{tr} and n_{eff} as free parameters in the model. First, a large number of singular value histograms are calculated by varying the parameters $\langle T \rangle$ between 0.025 and 0.083 and n_{eff} between 1.5 and 3.1. Then, we compare the numerically and experimentally obtained singular value histograms using a χ^2 goodness of fit metric, defined as

$$\chi^2 = \sum_{k=k'}^{M} \frac{|\mathrm{H_1(k)} - \mathrm{H_2(k)}|^2}{\mathrm{H_1(k)} + \mathrm{H_2(k)} + \varepsilon}, \tag{5.11}$$

with k the histogram bin index; k′ the histogram bin index of the bin with maximum counts, M the total number of histogram bins [51]. $\mathrm{H_1(k)}$ is the number of counts in the $\mathrm{k^{th}}$ numerical histogram bin; $\mathrm{H_2(k)}$ is the number of counts in $\mathrm{k^{th}}$ experimental histogram bin. ε is a small number included to provide numerical stability. The low singular values that lie to the left of the peak in the histogram are not taken into account as this part of the histogram is found to be extremely sensitive to detection noise. In simulations we have observed that adding noise to a transmission matrix drastically modifies this flank, but has much less effect on the rest of the histogram (see Chapter 4).

We show the obtained χ^2 values in Fig. 5.16 as a function of the n_{eff} and $\langle T \rangle$ values used in the model. Lighter colors indicate lower χ^2 and thus a better fit to the model. The white region is where the minimum goodness of fit χ^2 is expected.[7] The region of minimum χ^2 is observed to be a diagonal valley running from high transmission and low effective index to low transmission and high effective index. The goodness of fit metric χ^2 rises sharply when one moves perpendicular to this valley, but varies only little along its length. This valley tracks approximately constant kl_{tr} lines. While we can not retrieve l_{tr} and n_{eff} independently, we can retrieve the product kl_{tr}, which is the dimensionless scattering strength.

In Fig. 5.17, the experimental singular value histograms are compared to the numerical singular value histograms for the *a priori* estimates $l_{\mathrm{tr}} = 0.3$ μm and $n_{\mathrm{eff}} = 2.25$ and $l_{\mathrm{tr}} = 0.33$ μm and $n_{\mathrm{eff}} = 2.95$. The singular value histogram obtained for the parameters of $l_{\mathrm{tr}} = 0.33$ μm and $n_{\mathrm{eff}} = 2.95$ corresponds to the point of lowest χ^2 between the experimental and numerical singular value histograms. One can observe that in the region of low singular values the experimental histogram is influenced by noise, which is not included in the model. The noise causes a depletion of low singular values, and an increase in their density near the peak. In the right flank of the histogram both model curves agree qualitatively with the data, where the best fit curve obviously reproduces the shape

[7] Within 3σ from the minimum χ^2 as obtained from comparison of average experimental and numerical histograms. σ is the standard deviation of minimum χ^2 as obtained from the comparison of each model histogram with the average experimental histogram.

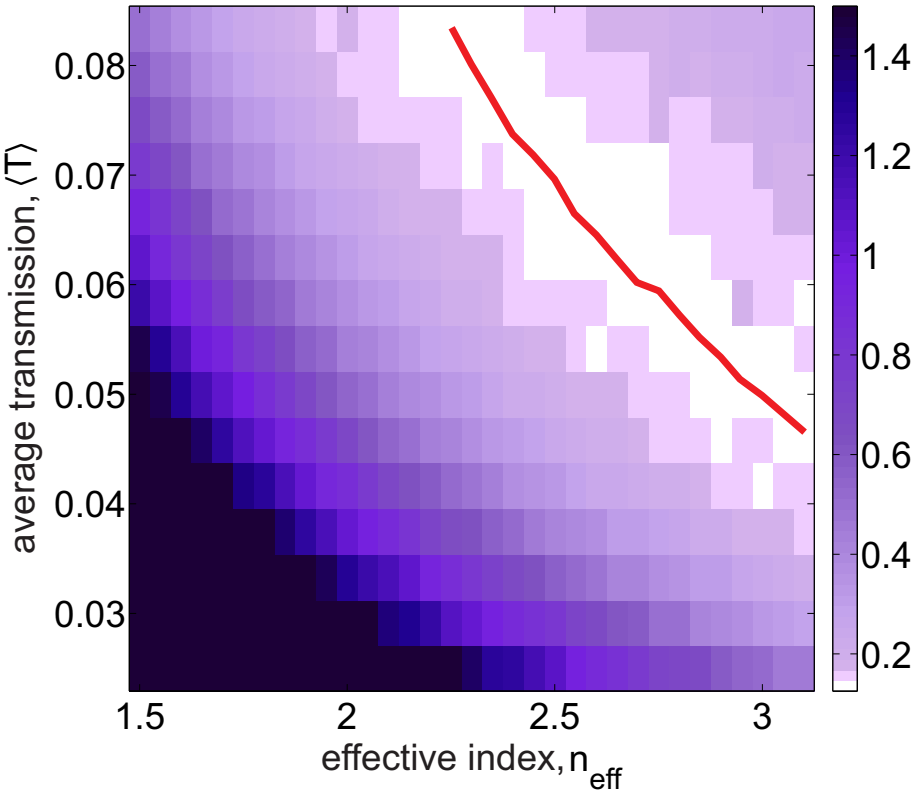

Figure 5.16.: Map of χ^2, the distance metric between the numerical model and the experimental data, as a function of the parameters $\langle T \rangle$ and n_{eff}. The white region corresponds to the best agreement between experiment and the model. Red line: kl_{tr} =10.2 curve.

of the experimental histogram a bit better.

While $n_{\text{eff}} > 2.3$ is not physical for the sample under study given the estimated filling fraction[8], we keep $n_{\text{eff}} > 2.3$ in the determination of kl_{tr} since we assume the filling fraction and l_{tr} are *a priori* unknown. In the region of best agreement between the model and experiment, $\text{k}l_{\text{tr}}$ is found to vary between 7.4 and 16.8, and its mean is found to be 10.5. To estimate an upperbound for the error in retrieved $\text{k}l_{\text{tr}}$, we assume all values between minimum and maximum $\text{k}l_{\text{tr}}$ found in the white region and derive $\text{k}l_{\text{tr}} = 10.5^{+6.3}_{-3.1}$. This errorbar is the statistical error of different model outcomes. Apart from this error we take into account other uncertainties:

1. The uncertainty in the thickness of the sample. The sample thickness is 6±0.5 μm, the uncertainty thus contributes about 8% error to kl_{tr}.

2. Mapping the slab transmission matrix to a waveguide model introduces a

[8] n_{eff} was estimated to be between 1.5 and 2.3.

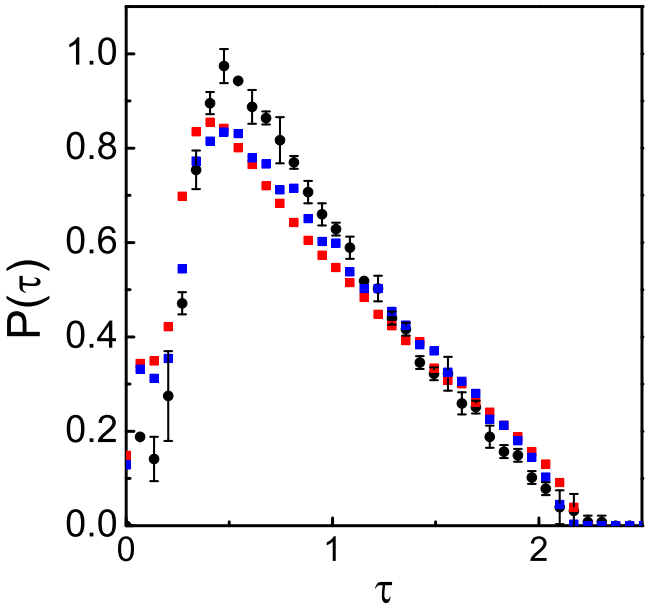

Figure 5.17.: Normalized singular value histograms obtained from the model and the experiment. Black dots: mean values, black errorbars: standard deviation of the normalized bin counts in 3 experimental singular value histograms. Red squares: model with l_{tr}=0.3 μm and $n_{\mathrm{eff}} = 2.25$. Blue squares: model with l_{tr}=0.33 μm and $n_{\mathrm{eff}} = 2.95$. Model curves are averages over 20 independent runs. The standard deviation of the model curves is similar to that of the experiment, for clarity the model is shown without error bars.

systematic uncertainty as the effective width of the waveguide can be chosen between the size scanned by the input fields and the FWHM area filled by all output spots. We take the average area, leaving an uncertainty in the effective waveguide area of 13%. This is expected to lead to an error of the same order in the number of open transmission eigenchannels, and therefore in kl_{tr}. In order to find a conservative total error estimate on kl_{tr}, we assume a symmetric error of 39% obtained from the fitting procedure. The total error is found by quadratically adding the statistical error contributions due to sample thickness and fitting, and subsequently directly adding the systematic error due to the waveguide width. We find that a conservative estimate for the total error in kl_{tr} is about 50%

While the obtained value of kl_{tr} is slightly higher, it is in the same range as the kl_{tr} values that we estimated from backscatter measurements and estimations of the effective index. The total error estimate on our determination of kl_{tr} is about

50%, which is good compared to other methods of determining this value.

5.7. Conclusions

In this chapter, we have described our experimental study on the transmission matrices of strongly scattering random photonic nanowire ensembles. We observe that the singular value histogram of the 6 μm thick nanowire ensemble indicates presence of correlations in the measured matrices. This is the first report of correlations in measured transmission matrices of such strongly scattering samples at optical wavelengths [52]. Using a numerical model, along with estimated sample parameters of l_{tr} and n_{eff}, we model the singular value histograms and find good agreement with experimental histograms.

By using the *a priori* uncertain sample parameters as fit parameters we retrieve the dimensionless scattering strength, kl_{tr} of the 6 μm thick nanowire ensemble. This is the first quantitative retrieval of sample parameters from a measured transmission matrix. Our result for kl_{tr} is consistent with prior estimates. The uncertainty in the retrieved scattering strength is $\pm 50\%$ which compares well with other methods. Remarkably, the most promising way to further reduce uncertainty is to improve the theoretical modeling.

Bibliography

[1] C. W. J. Beenakker, *Random-matrix theory of quantum transport*, Rev. Mod. Phys. **69**, 731 (1997). — p.69, 85.

[2] E. G. van Putten and A. P. Mosk, *The information age in optics: Measuring the transmission matrix*, Physics **3**, (2010). — p.69, 70, 86.

[3] N. Garcia and A. Z. Genack, *Crossover to strong intensity correlation for microwave radiation in random media*, Phys. Rev. Lett. **63**, 1678 (1989). — p.69.

[4] R. Pnini and B. Shapiro, *Fluctuations in transmission of waves through disordered slabs*, Phys. Rev. B **39**, 6986 (1989). — p.69.

[5] J. F. de Boer, M. C. W. van Rossum, M. P. van Albada, T. M. Nieuwenhuizen, and A. Lagendijk, *Probability distribution of multiple scattered light measured in total transmission*, Phys. Rev. Lett. **73**, 2567 (1994). — p.69.

[6] A. Derode, P. Roux, and M. Fink, *Robust acoustic time reversal with high-order multiple scattering*, Phys. Rev. Lett. **75**, 4206 (1995). — p.69.

[7] A. A. Chabanov, M. Stoytchev, and A. Z. Genack, *Statistical signatures of photon localization*, Nature **404**, 850 (2000). — p.69.

[8] P. Sebbah, B. Hu, A. Z. Genack, R. Pnini, and B. Shapiro, *Spatial-field correlation: the building block of mesoscopic fluctuations*, Phys. Rev. Lett. **88**, 123901 (2002). — p.69.

[9] G. Lerosey, J. de Rosny, A. Tourin, and M. Fink, *Focusing beyond the diffraction limit with far-field time reversal*, Science **315**, 1120 (2007). — p.69.

[10] S. M. Popoff, G. Lerosey, R. Carminati, M. Fink, A. C. Boccara, and S. Gigan, *Measuring the transmission matrix in optics: An approach to the*

study and control of light propagation in disordered media, Phys. Rev. Lett. **104**, 100601 (2010). — p.69, 70, 78.

[11] Y. Choi, T. D. Yang, C. Fang-Yen, P. Kang, K. J. Lee, R. R. Dasari, M. S. Feld, and W. Choi, *Overcoming the diffraction limit using multiple light scattering in a highly disordered medium*, Phys. Rev. Lett. **107**, 023902 (2011). — p.69.

[12] Y. Choi, M. Kim, C. Yoon, T. D. Yang, K. J. Lee, and W. Choi, *Synthetic aperture microscopy for high resolution imaging through a turbid medium*, Opt. Lett. **36**, 4263 (2011). — p.69.

[13] Z. Shi and A. Z. Genack, *Transmission eigenvalues and the bare conductance in the crossover to Anderson localization*, Phys. Rev. Lett. **108**, 043901 (2012). — p.69.

[14] Z. Shi, J. Wang, and A. Z. Genack, *Microwave "optical" conductance*, arXiv **1303.1133**, (2013). — p.69.

[15] I. M. Vellekoop and A. P. Mosk, *Focusing coherent light through opaque strongly scattering media*, Opt. Lett. **32**, 2309 (2007). — p.69.

[16] S. Popoff, G. Lerosey, M. Fink, A. C. Boccara, and S. Gigan, *Image transmission through an opaque material*, Nat. Commun. **1**, 1 (2010). — p.69.

[17] M. Kim, Y. Choi, C. Yoon, W. Choi, J. Kim, Q.-H. Park, and W. Choi, *Maximal energy transport through disordered media with the implementation of transmission eigenchannels*, Nat. Photon. **6**, 581 (2012). — p.69.

[18] I. M. Vellekoop and A. P. Mosk, *Universal optimal transmission of light through disordered materials*, Phys. Rev. Lett. **101**, 120601 (2008). — p.69.

[19] S. Hemmady, X. Zheng, T. M. Antonsen Jr., E. Ott, and S. M. Anlage, *Universal statistics of the scattering coefficient of chaotic microwave cavities*, Phys. Rev. E **71**, 056215 (2005). — p.69.

[20] R. A. Méndez-Sánchez, U. Kuhl, M. Barth, C. H. Lewenkopf, and H.-J. Stöckmann, *Distribution of reflection coefficients in absorbing chaotic microwave cavities*, Phys. Rev. Lett. **91**, 174102 (2003). — p.69.

[21] Z. Shi, M. Davy, J. Wang, and A. Z. Genack, *Focusing through random media in space and time: a transmission matrix approach*, Opt. Lett. **38**, 2714 (2013). — p.69.

[22] O. L. Muskens, S. L. Diedenhofen, B. C. Kaas, R. E. Algra, E. P. A. M. Bakkers, J. Gómez Rivas, and A. Lagendijk, *Large photonic strength of highly tunable resonant nanowire materials*, Nano Lett. **9**, 930 (2009). — p.70.

[23] T. Strudley, T. Zehender, C. Blejean, E. P. A. M. Bakkers, and O. L. Muskens, *Mesoscopic light transport by very strong collective multiple scattering in nanowire mats*, Nat. Photon. **7**, 413 (2013). — p.70, 71.

[24] J. H. Li, A. A. Lisyansky, T. D. Cheung, D. Livdan, and A. Z. Genack, *Transmission and surface intensity profiles in random media*, Europhys. Lett. **22**, 675 (1993). — p.70.

[25] K. L. van der Molen, *Experiments on scattering lasers from Mie to random*, Ph.D. thesis, 2007. — p.70.

[26] I. M. Vellekoop, *Controlling the propagation of light in disordered scattering media*, Ph.D. thesis, University of Twente, 2008. — p.70.

[27] D. E. Aspnes and A. A. Studna, *Dielectric functions and optical parameters*

of Si, Ge, GaP, GaAs, GaSb, InP, InAs, and InSb from 1.5 to 6.0 eV, Phys. Rev. B **27**, 985 (1983). — p.70.

[28] O. L. Muskens, J. Gómez Rivas, R. E. Algra, E. P. A. M. Bakkers, and A. Lagendijk, *Design of light scattering in nanowire materials for photovoltaic applications*, Nano Lett. **8**, 2638 (2008). — p.71.

[29] S. L. Diedenhofen, *Propagation of light in ensembles of semiconductor nanowires*, Ph.D. thesis, Eindhoven University of Technology, 2010. — p.71.

[30] C. F. Bohren and D. R. Huffman, *Absorption and scattering of light by small particles* (John Wiley and Sons, Inc., 1983). — p.71.

[31] J. Gómez Rivas, D. H. Dau, A. Imhof, R. Sprik, B. P. J. Bret, P. M. Johnson, T. W. Hijmans, and A. Lagendijk, *Experimental determination of the effective refractive index in strongly scattering media*, Opt. Commun. **220**, 17 (2003). — p.73.

[32] A. F. Koenderink and W. L. Vos, *Light exiting from real photonic band gap crystals is diffuse and strongly directional*, Phys. Rev. Lett. **91**, 213902 (2003). — p.73.

[33] B. P. J. Bret and A. Lagendijk, *Anisotropic enhanced backscattering induced by anisotropic diffusion*, Phys. Rev. E **70**, 036601 (2004). — p.73, 87.

[34] B. P. J. Bret, *Multiple light scattering in porous gallium phosphide*, Ph.D. thesis, University of Twente, 2005. — p.73.

[35] E. N. Leith and J. Upatnieks, *Reconstructed wavefronts and communication theory*, J. Opt. Soc. Am. **52**, 1123 (1962). — p.75.

[36] M. Takeda, H. Ina, and S. Kobayashi, *Fourier-transform method of fringe-pattern analysis for computer-based topography and interferometry*, J. Opt. Soc. Am. **72**, 156 (1982). — p.75.

[37] T. L. Boullion and P. L. Odell, *Generalized inverse matrices* (John Wiley and Sons, Inc., 1971). — p.77.

[38] A. Aubry and A. Derode, *Random matrix theory applied to acoustic backscattering and imaging in complex media*, Phys. Rev. Lett. **102**, 084301 (2009). — p.78.

[39] A. Aubry and A. Derode, *Singular value distribution of the propagation matrix in random scattering media*, Waves Random Complex Media **20**, 333 (2010). — p.78.

[40] V. A. Marčénko and L. A. Pastur, *Distribution of eigenvalues for some sets of random matrices*, Math. USSR-Sbornik **1**, 457 (1967). — p.79, 81.

[41] O. N. Dorokhov, *On the coexistence of localized and extended electronic states in the metallic phase*, Solid State Commun. **51**, 381 (1984). — p.85.

[42] P. A. Mello, P. Pereyra, and N. Kumar, *Macroscopic approach to multichannel disordered conductors*, Ann. of Phys. **181**, 290 (1988). — p.85.

[43] A. Lagendijk, R. Vreeker, and P. de Vries, *Influence of internal reflection on diffusive transport in strongly scattering media*, Phys. Lett. A **136**, 81 (1989). — p.85.

[44] J. Zhu, D. Pine, and D. Weitz, *Internal reflection of diffusive light in random media*, Phys. Rev. A **44**, 3948 (1991). — p.85, 87.

[45] J. F. de Boer, *Optical fluctuations on the transmission and reflection of*

mesoscopic systems, Ph.D. thesis, Universiteit van Amsterdam, 1995. — p.85.

[46] E. Akkermans, P. E. Wolf, and R. Maynard, *Coherent backscattering of light in disordered media: Analysis of the peak line shape*, Phys. Rev. Lett. **56**, 1471 (1986). — p.85.

[47] S. Olver and R. R. Nadakuditi, *Numerical computation of convolutions in free probability theory*, arXiv **1203.1958**, (2012). — p.86.

[48] A. Goetschy and A. D. Stone, *Filtering random matrices: The effect of imperfect channel control in multiple-scattering*, Phys. Rev. Lett. **111**, 063901 (2013). — p.86.

[49] F. J. P. Schuurmans, *Light in complex dielectrics*, Ph.D. thesis, Universiteit van Amsterdam, 1999. — p.87.

[50] Y. V. Nazarov, *Limits of universality in disordered conductors*, Phys. Rev. Lett. **73**, 134 (1994). — p.88.

[51] W. Press, S. Teukolsky, W. Vetterling, and B. Flannery, *Numerical recipes the art of scientific computing* (Cambridge University Press, 2007). — p.89.

[52] *We have learnt that similar observations have been made in the group of the late Prof. Michael Feld.* — p.92.

CHAPTER 6

Transmission Matrices of Strongly Scattering Random Photonic Nanoparticle Media

6.1. Introduction

The optical transmission matrix is a matrix representation of the transmission operator through a sample, written in a pre-defined basis. It describes how the fields incident on and transmitted through the sample are related. Direct measurements of the optical transmission matrices of scattering samples have been reported by several groups [1–5]. In these studies, knowledge of the transmission matrix was used to focus through [1], send an image through [2], enhance the transmission through [5] the scattering sample and increase the resolution of the imaging system made from a random medium [3, 4].

In this chapter, we describe measurements of the transmission matrices of strongly scattering random photonic media composed of ZnO nanoparticles. Similar samples have been used in many experiments [3–8] and have been characterized very well. The geometry of the samples enables good optical access during transmission matrix measurements, thus allowing measurement of large parts of the transmission matrix. When measurement of a large part of the transmission matrix is combined with the sufficiently strong scattering of the random photonic medium, mesoscopic correlations are expected to show up in the measured transmission matrices but have not been reported before [9]. The first motivation of this chapter is thus to observe mesoscopic correlations in the transmission matrices of strongly scattering random photonic media composed of ZnO nanoparticles. Our second motivation is to compare the experimental results to a numerical model developed by us and to an analytical model developed by Goetschy and Stone [10] to interpret our measurements.

In Section 6.2, the ZnO samples are described. The experimental procedure is described in Section 6.3 and the results are shown in Section 6.4. A comparison of the experimental and numerical results is given in Section 6.5. Finally, the experimental results are compared to the predictions of an analytical theory [10] in Section 6.6.

6.2. Samples

In this chapter, measurements are performed on two samples of different thickness. Both samples are layers of ZnO nanoparticles in air. The samples were prepared by Elbert van Putten using a method described in detail in Ref. [11]. The ZnO powder that is used is a commercial powder with average grain size of 200 nm (Sigma Aldrich ZnO < 1 μm 99.9%). Samples prepared according to similar procedures have a transport mean free path of $l_{\rm tr}$=0.7±0.2 μm and an effective refractive index of $n_{\rm eff}$=1.4±0.1 in Ref. [8] and $l_{\rm tr} = 0.63^{+0.17}_{-0.11}$ μm and $n_{\rm eff} = 1.4 \pm 0.06$ in Ref. [11].

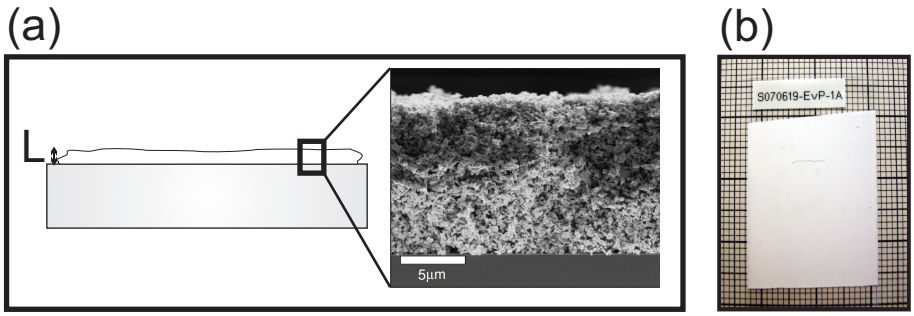

Figure 6.1.: (a) Schematic of a layer of ZnO nanoparticles in air sprayed on a glass substrate, with the scanning electron microscope (SEM) picture of a typical layer shown in the inset. L:thickness of layer. (b) Photograph of a typical sample. SEM image and the photograph taken from Reference [12].

In Fig. 6.1 (a) the schematic of the random photonic medium, composed of ZnO nanoparticles in air is shown. The thickness L of the layers used in this chapter are 11±1 μm and 31±6 μm, measured under an optical microscope using a scratch made in the nanoparticle layer[1]. The glass substrate is a standard microscope cover glass and has a thickness of nominally 170 μm. A SEM picture of the layer of nanoparticles in air is shown in the inset of Fig. 6.1 (a). It is seen that the layer is porous and there is good contact between the glass slide and ZnO nanoparticles. From Fig. 6.1 (b), it is seen that the samples completely hide a pattern behind them. They are optically thick and fully opaque.

In Fig. 6.2, the root mean square (rms) fields transmitted through both the thin and the thick samples are shown as density plots in momentum space. The momentum space maps of the two samples are almost identical where the transmitted fields approximately fill a disk in momentum space with an effective detection numerical aperture (NA) extending up to 1.3 in the x-direction and up to 1.2 in the y-direction at the half maximum of the rms field.

Besides being strongly scattering samples, layers of ZnO nanoparticles in air are chosen because of relatively low effective refractive indices and direct access to the front and rear surfaces of the sample. SEM images and rms field density

[1] From this point on, the 11-μm thick sample is called the "thin sample" and the 31-μm thick sample the "thick sample".

plots in momentum space indicate good contact between the samples and the glass substrate. In combination of all these properties, these samples provide an excellent system for transmission matrix experiments.

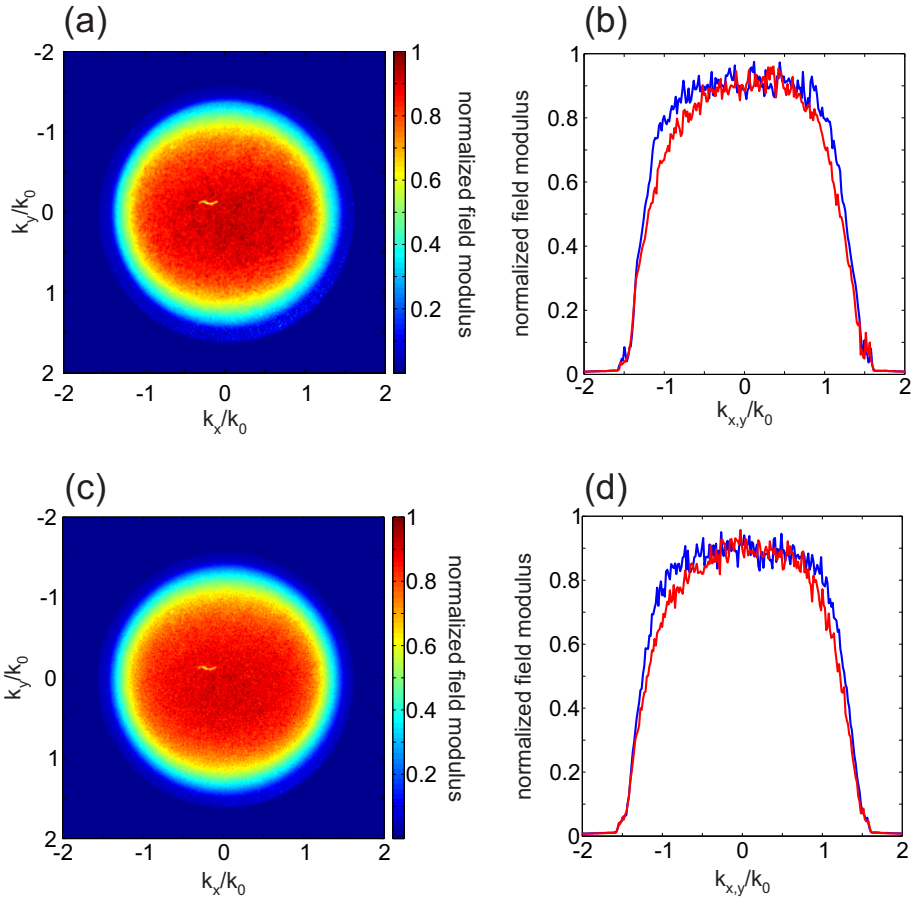

Figure 6.2.: (a, c) Momentum-space density map of root mean square fields, $\sqrt{\langle |E(k)|^2 \rangle}$ transmitted through the 11-μm and 30-μm thick layer of ZnO nanoparticles on glass. (b, d) Cross sections of the images in (a, d) along x- (blue curve) and y- (red curve) directions. The illumination NA is 0.95.

6.3. Experimental method

The experimental setup is shown in Fig. 6.3. It is identical to the setup used for transmission matrix measurements of GaP nanowire layers as explained in Chapter 5, except for the illumination objective. In the case of ZnO nanoparticle layers, the sample geometry allows us to use a high NA objective on both illumination and detection sides. On the illumination side, a Zeiss objective with

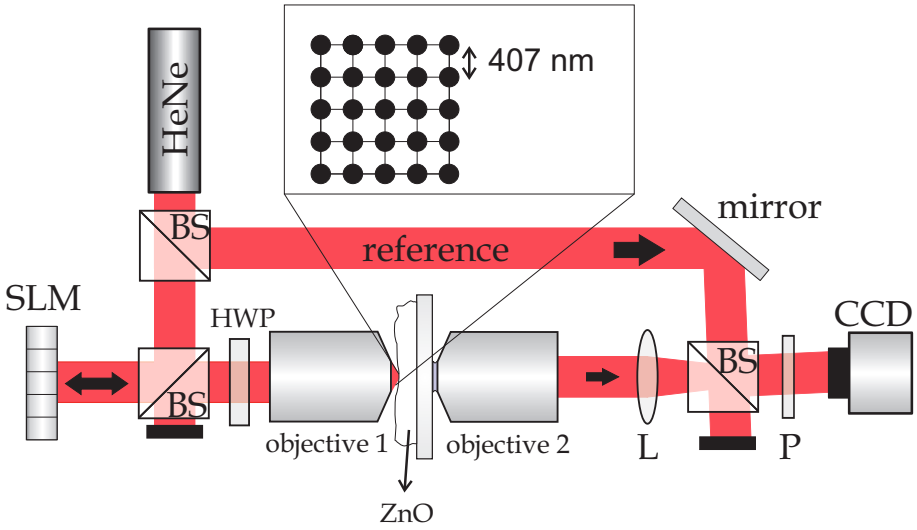

Figure 6.3.: Experimental setup. HeNe: laser. BS: 50:50 beam splitter. SLM: phase-only spatial light modulator. HWP: half-wave plate. ZnO: sample. Objective 1: 63× 0.95-NA objective. Objective 2: 60× 1.42-NA oil immersion objective. L: 500 mm focal length lens. P: polarizer. CCD: camera sensor.

63× magnification and NA=0.95 is used and on the detection side, an Olympus oil-immersion objective with 60× magnification and NA=1.42 is used. The FWHM of the spot focused on the front surface of the sample is ≈390 nm. In this case, the overlap between different incident fields is found to be small so that the probed area could be sampled in a dense way, as shown in the inset in Fig. 6.3. When dense sampling is performed, the distance between the centers of two nearest neighbor incident spots on the sample surface is 407±19 nm, corresponding to $0.64\lambda \pm 0.03\lambda$. In section 6.4, we also provide the results of analyses when a checkerboard filtering is applied to the positions of incident spots. In that case, the distance between two nearest neighboring spots becomes 576±27 nm, corresponding to $0.91\lambda \pm 0.04\lambda$. Throughout the chapter, the sampling made when checkerboard filter is applied is called the sparse sampling. In both cases, the incident spots are scanned over an area of 10.2 μm by 10.2 μm.

The matrix $\widetilde{T}$ that is obtained from a transmission matrix experiment is related to the transmission matrix of the ZnO layer T by $\widetilde{T} = T_2 T T_0$. T_2 is the matrix that maps the fields at the rear surface of the sample to the detected fields, and T_0 is the matrix constructed by the fields at the incident surface of the sample. To quantify how much $\widetilde{T}$ differs from T, we measure a reference matrix $\widetilde{T}_0 = T_2 T_0$ through a bare glass slide. We thus investigate how much the singular value histogram of the reference glass slide deviates from the singular value density of a unitary matrix, which is a single peak at the singular value 1. The singular value histogram of $\widetilde{T}_0$ matrix is used in the numerical model to include the experimental sampling condition and the multiplicative noise.

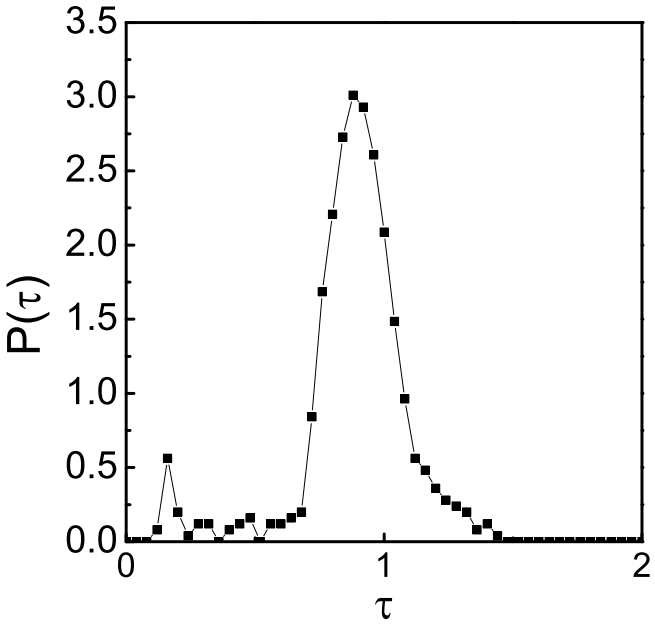

Figure 6.4.: Transmission singular value histogram of the reference glass slide, as normalized by $\sqrt{\langle \tau^2 \rangle}$. Black dots: measured singular values.

The normalized singular value histogram of the reference glass transmission matrix $\widetilde{T}_0$ is shown in Fig. 6.4. The normalized[2] histogram has a peak centered at the singular value of 0.89 and a full width at half maximum of 0.29. A small peak at a histogram bin centered at the singular value of 0.17 is observed. This can be due to overlap between the incident fields. Two isolated singular values are observed at 3.46 and 9.91 (not shown)[3]. These isolated high singular values are attributed to fields that are present as an offset in all recorded fields such as a small reflection from the front window of the SLM. These spurious singular values are observed in all measurements and are not shown from this point on, as they decouple from the rest of the singular values.

As we also observed, it is not possible to measure a unitary transmission matrix in an optical experiment first of all due to the fundamental limitation that fields with limited spread in momentum space do not form a complete basis in a finite area (see Chapter 4). Moreover, other experimental factors such as detection

[2]In all singular value histograms presented in this chapter, the normalization is done to make $\sqrt{\langle \tau^2 \rangle} = 1$ as is usually performed when an *a priori* normalization is not available.

[3]The spurious singular values are included in the normalization. When they are excluded from the normalization, the peak of the histogram is found to be at singular value of 1. In the rest of the chapter, their effect on the shape of the histograms is found to be negligible.

noise, fluctuations in the focussed spot intensity and spatial overlap between incident spots broaden the peak in the singular value histogram.

6.4. Results

In this section, we present the results of transmission matrix measurements performed on both samples. We study the singular value histograms of the measured transmission matrices and as a first test, compare the obtained histograms to the Marcenko-Pastur singular value density [13]. The Marcenko-Pastur theory gives the singular value density of an uncorrelated random matrix. The minimum and maximum singular values and the shape of the singular value density plot only depend on the aspect ratio γ of the number of rows to the number of columns of the matrix (see Chapters 2 and 5). The aspect ratio γ is not a free parameter, but it is fixed as the ratio of accessible incident and outgoing modes in our setup,

$$\begin{aligned} \gamma &= \frac{\mathrm{N_{out}}}{\mathrm{N_{in}}} \\ &= \frac{m_2}{m_1}, \end{aligned} \tag{6.1}$$

with m_2 and m_1 described in the same way as in our numerical model in Section 6.5. We observe deviations from Marcenko-Pastur curves. This deviation is an indication for correlations being present in the experimental data.

The experimental procedure is the same for the thin and the thick samples, and their results are presented together. The thickness of the thin sample is comparable to the side length of the area over which the incident free modes are scanned. Taking into account the reported range for the l_{tr} and n_{eff} parameters [8, 11], we estimate the number of open transmission eigenchannels to be between 170 and 415 in our experiments on the thin sample.[4] For the thick sample, we expect this number to be between 180 and 440, which is very similar to the case of the thin sample.[5] The number of pairs of independent incident fields and fields detected in our transmission matrix measurements is larger than the number of estimated open transmission eigenchannels for both samples. In light of the above arguments, we expect to observe similar results with clear signatures of correlations in the transmission matrices of both samples.

In Fig. 6.5 (a) and (b) average intensities of the fields transmitted through the thin and thick ZnO layer are shown for incident horizontal polarization, respectively. The average intensity profile is roughly circular in both cases and displays a granular structure, due to a shadowing effect of ZnO nanoparticles on glass. In Fig. 6.5 (a) the average intensity covers a smaller area on the detector as the sample is thinner and the diffuse spreading is less as compared to Fig. 6.5 (b). The black squares in Fig. 6.5 (a) and (b) reside at the position where the average transmitted intensity drops to about half of its peak value. The 14-μm

[4] The thin sample is modeled as a waveguide 12.1-μm wide and 11.25-μm long, see Sec. 6.5 and Sec. 6.6

[5] The thick sample is modeled as a waveguide 20.6-μm wide and 30.7-μm long, see Sec. 6.6

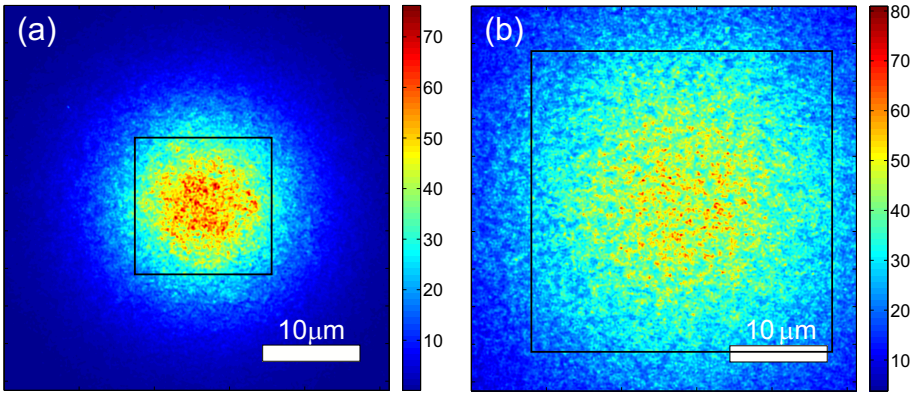

Figure 6.5.: Average intensities of 625 fields transmitted through (a) 11-μm thick and (b) 31-μm thick layer of ZnO.

wide region inside the black square in Fig. 6.5 (a) and the 31-μm wide region inside the black square in Fig. 6.5 (b) are used as the detection field of view during data analysis of the thin and thick samples, respectively.

In Fig. 6.6, we show the normalized singular value histograms of (a) thin and (b) thick ZnO layer in the sparse sampling case. The histogram is highly asymmetric in both Fig. 6.6 (a) and (b), it shows a sharp rise at the low singular values and decays almost linearly. In Fig. 6.6 (a), the obtained singular values lie between 0.28 and 2.00, the peak of the histogram is observed at $0.46^{+0.05}_{-0.04}$.[6] In Fig. 6.6 (b) the singular values lie between 0.34 and 1.90 and the peak of the singular value histogram is at $0.57^{+0.11}_{-0.08}$. We show the Marcenko-Pastur singular value density alongside the experimental histogram. In Fig. 6.6 (a), the Marcenko-Pastur singular value density lies between $\tau = 0.47$ and $\tau = 1.53$, and in Fig. 6.6 (b), it lies between $\tau = 0.69$ and $\tau = 1.31$, with a sharp peak at $\tau = 0.95$. Its shape is less asymmetric than the experimental results, the peak occurs at a higher singular value, and the width is narrower. Since the model for an uncorrelated random matrix is completely different from the experimental histogram, it is concluded that the measured fields are correlated.

In Fig. 6.7, the singular value histogram measured with the dense sampling of incident fields is shown for (a) the thick and (b) the thin sample. Here the full dataset of 1250 fields is used without applying the checkerboard filter. In both cases, the experimental singular value histogram is highly asymmetric. The overall shape of the experimental singular value histograms look similar, however, there are some small discrepancies. The singular values of the thin sample, shown in Fig. 6.7 (a) are slightly more spread and lie between singular values of 0.09

[6] A 5^{th} order polynomial is fitted to several bins with highest counts. The peak is determined as the peak of the fitted function. The error margin in peak position is taken as the abscissa corresponding to ordinates with a value within a σ from the peak value. σ is the average standard deviation in the normalized bin counts. The same procedure is applied for all histograms in this chapter.

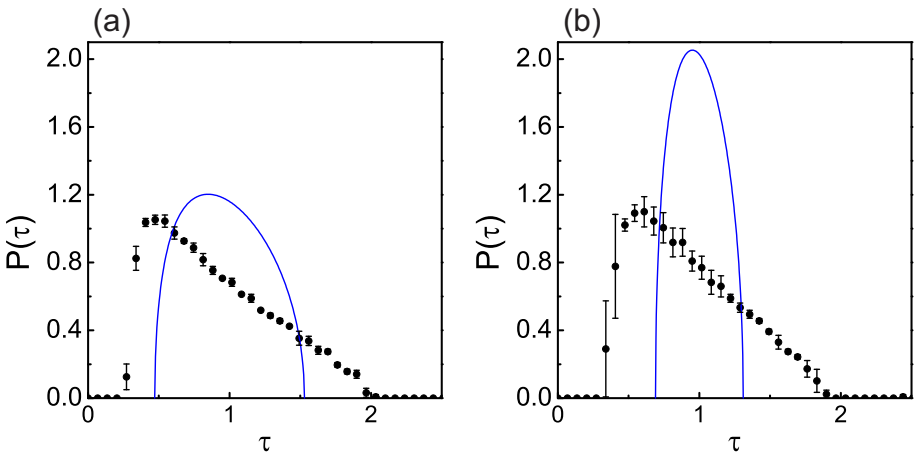

Figure 6.6.: Normalized singular value histogram of the transmission matrix of (a) thin sample, (b) thick sample in the case of sparse sampling, normalization factor=$\sqrt{\langle\tau^2\rangle}$. Black dots: mean values, errorbars: standard deviation of the normalized counts in the singular value histograms of three different transmission matrices. Solid curve: Marcenko-Pastur singular value density with (a) $\gamma = 3.57$, (b) $\gamma = 10.4$.

and 2.46 with a sharp peak at $0.25^{+0.04}_{-0.02}$, whereas the singular values of the thick sample, shown in Fig. 6.7 (b) lie between 0.04 and 2.30 with a peak at $0.38^{+0.1}_{-0.07}$. In Fig. 6.7 (a), the Marcenko-Pastur singular value density extends between the singular values of 0.25 and 1.75 and resembles a distorted semi-ellipse and in Fig. 6.7 (b), the Marcenko-Pastur curve lies between $\tau = 0.56$ and $\tau = 1.44$, and looks like a semi-ellipse with a peak at $\tau = 0.9$. In both cases, the Marcenko-Pastur singular value density shows a strong disagreement with the experimental singular value histograms regarding peak position, width and shape. The fact that we see a continuous spread of experimental singular values at $\tau > 2$, which is impossible for the Marcenko-Pastur curves demonstrates that there are strong correlations in the transmission matrices.

Interestingly, it is found that the random photonic samples of ZnO nanoparticles in air are expected to have on the same order of and even slightly smaller number of open transmission eigenchannels as compared to the random photonic nanowire mats that were described in the previous chapter. This is surprising since the l_{tr} of the nanowire mats is smaller as compared to that of the layers of ZnO nanoparticles, so that the nanowire mat of 6 μm thickness has a smaller average transmission $\langle T\rangle$ than the 11 μm thick layer of ZnO nanoparticles. This puzzle can be solved by considering that when we investigate a certain area of the sample, the sample with the higher n_{eff} supports more transmission eigenchannels N_{channels} as compared to the sample with lower n_{eff}. This leads to a lower number of estimated open transmission eigenchannels $N_{\mathrm{open}} \approx N_{\mathrm{channels}}\langle T\rangle$ for the sample with the low n_{eff}, even if it has a larger $\langle T\rangle$.

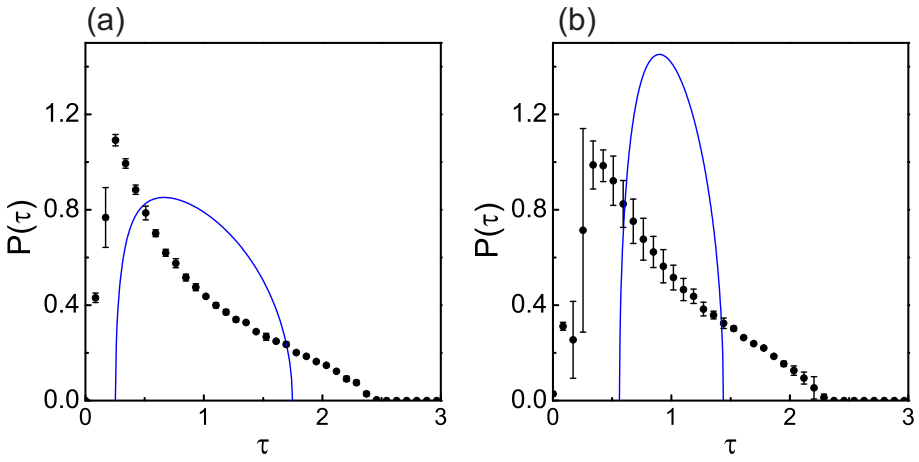

Figure 6.7.: Normalized singular value histograms of the transmission matrix of (a) thin sample, (b) thick sample in the case of dense sampling, normalization factor=$\sqrt{\langle\tau^2\rangle}$. Black dots: mean, errorbars: standard deviation of the normalized counts in the singular value histograms of three different transmission matrices. Solid curve: Marcenko-Pastur singular value density with (a) $\gamma = 1.79$, (b) $\gamma = 5.2$.

It must be kept in mind that we have slab type samples that we model as waveguides. In a slab, there is no lateral confinement for the light. For the thick sample, there is a considerable mismatch between the probed area (10.2 μm width) and the thickness of the sample (30.7 μm), and in turn, with the detection field of view (31 μm width). Intuitively, one can appreciate that the number of outgoing modes in the detection field of view is much larger than the number of modes incident to the probed area. Since only a small fraction of the transmission matrix that describes the detection area is probed, one would expect reduced correlations in the transmission matrix of the thick sample, despite the small number of open transmission eigenchannels predicted when the sample is modeled as a waveguide. Our results show that the transmission matrices of the thick sample have similar properties as the transmission matrices of the thin samples, and both show correlations. Therefore we conclude that modeling the samples as waveguides is appropriate even for the thick sample.

6.5. Comparison to numerical model

In this section, we describe the singular value histograms of the thin sample as predicted by a numerical model that we developed. In summary, this model gives the singular value histogram of a transmission matrix that is measured partially. Experimental noise and oversampling of the incident fields are also included in

the model. A more detailed description of this model is given in Chapter 5.[7]

The model simplifies the slab-type geometry of the sample to that of a waveguide, and takes effective refractive index, n_{eff}, average transmission, $\langle T \rangle$, m_1 and m_2 as input parameters. It gives the singular values of the partial transmission matrix as output. Here m_1 is the ratio of number of fields incident on the sample N_{in} to the total number of transmission eigenchannels N_{channels} of the model waveguide, and m_2 is the ratio of detectable outgoing free modes from the sample N_{det} to the total number of transmission eigenchannels of the model waveguide N_{channels}

$$m_1 = \frac{N_{\text{in}}}{N_{\text{channels}}}, \tag{6.2}$$

with

$$N_{\text{channels}} = \frac{2\pi A n_{\text{eff}}^2}{\lambda^2}. \tag{6.3}$$

Here, λ is the free space wavelength and A is the area of the waveguide taken as the algebraic average of the width of the area scanned by incident fields and the width of detection field of view. In our case $A = (12.1\ \mu\text{m})^2$ for the thin sample.

For the detection side,

$$m_2 = \frac{\text{NA}_{\text{det}}^2}{2n_{\text{eff}}^2}. \tag{6.4}$$

where $\text{NA}_{\text{det}} = 1.4$ is the detection numerical aperture. The factor of $1/2$ is included since the detection is made with a single polarization.

We now provide the result of the model for $l_{\text{tr}} = 0.65\ \mu\text{m}$ and $n_{\text{eff}} = 1.4$. Using the given parameters and the expression

$$\langle T \rangle = \frac{z_{\text{inj}} + z_{e1}}{L + z_{e1} + z_{e2}}. \tag{6.5}$$

Using $z_{\text{inj}} = 0.87 l_{\text{tr}}$ along with extrapolation lengths of $z_{e1} = 1.96 l_{\text{tr}}$ and $z_{e2} = 0.68 l_{\text{tr}}$, $\langle T \rangle = 0.15$, $m_1 = 0.28$ and $m_2 = 0.5$ are obtained and used in the model.

In Fig. 6.8, we show the singular value histograms obtained from the experiment and the model. The two curves overlap almost perfectly. Both histograms show a sharp rise at the low singular values with the peak of the experimental singular value histogram at $0.25^{+0.04}_{-0.02}$, slightly to the right of the peak of the model histogram, which is at 0.19 ± 0.02. The experimental histogram decays to zero at the singular value of 2.46, whereas the model histogram has no counts in the histogram bins beyond a singular value of 2.37. The decaying behavior of the two histograms is qualitatively similar; both show a fast decay near the peak with a slower decaying tail extending to high singular values. It is also observed that the experimental histogram has higher counts at the bins around the peak and has slightly lower counts in the bins between the normalized singular values of 1 and 2 as compared to the counts in the model histogram.

Next, we run the numerical model for a range of $\langle T \rangle$ and n_{eff} values to see the dependance of the obtained histograms on these parameters. The bins corresponding to low singular values are more susceptible to noise. For this reason,

[7] In this chapter the size of the unitary matrices used in Step 1 of the model is 4000 by 4000 instead of 8000 by 8000.

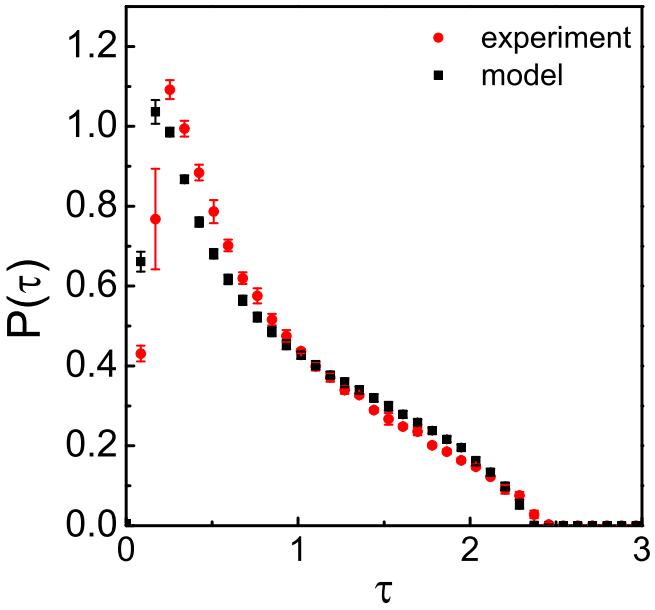

Figure 6.8.: Normalized singular value histograms obtained from the experiment and from the model using $l_{\mathrm{tr}} = 0.65$ μm and $n_{\mathrm{eff}} = 1.4$, with normalization factor, $\sqrt{\langle \tau^2 \rangle}$. Red dots: mean, red errorbars: standard deviation of 3 experimental singular value histograms. Black squares: mean, black errorbars: standard deviation of singular value histograms obtained from 20 runs of the model.

the comparison between numerical and experimental histograms is made using the bins of singular values higher than the bin with the maximum counts in the experimental histogram. The metric used for comparison is the goodness of fit χ^2 [14]

$$\chi^2 = \sum_{k=k'}^{M} \frac{|\mathrm{H}_1(\mathrm{k}) - \mathrm{H}_2(\mathrm{k})|^2}{\mathrm{H}_1(\mathrm{k}) + \mathrm{H}_2(\mathrm{k}) + \varepsilon}, \tag{6.6}$$

where $\mathrm{H}_1(\mathrm{k})$ is the number of counts in the k^{th} numerical histogram bin; $\mathrm{H}_2(\mathrm{k})$ is the number of counts in k^{th} experimental histogram bin, k is the histogram bin index; k' is the histogram bin index of the bin with maximum counts, M is the total number of histogram bins and ε is a small number added to the denominator for numerical stability.

The map of χ^2 obtained for a range of parameters, n_{eff} from 1.2 to 1.8 and $\langle T \rangle$ from 0.04 to 0.22 is shown in Fig. 6.9. Lighter colors indicate lower values of χ^2, meaning good agreement between experiment and model. We observe that

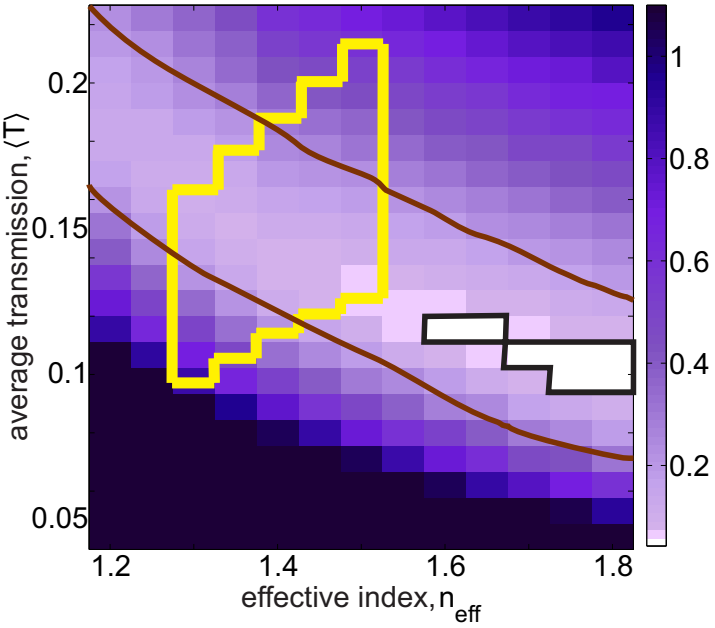

Figure 6.9.: Parameter maps for χ^2, obtained from comparison of numerical and experimental singular value histograms. The white region enclosed by black lines corresponds to the region of best agreement between experiment and model. The region enclosed by yellow borders correspond to the parameters that have been reported before.

the relatively low χ^2 values lie in a valley marked by the brown lines. This valley lies diagonally from $n_{\text{eff}} = 1.2$ with $\langle T \rangle$ between 0.16 and 0.22 to $n_{\text{eff}} = 1.8$ with $\langle T \rangle$ between 0.07 and 0.13. The trough of the valley is the white region, enclosed by black lines. The white region is where minimum χ^2 is expected.[8] The region enclosed by yellow borders indicates the region of parameters that were reported in Ref. [8]. This region resembles a parallelogram and extends from low $\langle T \rangle$, 0.1 and low n_{eff}, 1.3 to high $\langle T \rangle$, 0.21 and high n_{eff}, 1.5 and intersects with the valley we find.

6.6. Comparison to analytical model

In this section, we compare the singular value histograms obtained from our measurements with the probability density function of singular values predicted

[8] Within 3σ from the minimum χ^2 as obtained from comparison of average experimental and numerical histograms, σ is the standard deviation of minimum χ^2 as obtained from the comparison of each model histogram with the average experimental histogram.

by an analytical theory developed by Goetschy and Stone [10].[9] The analytical model is developed to take into account the limited information access to the sample under study. This is a typical situation in all transmission matrix measurements and prevents the experimenter from observing the full DMPK singular value density, which has a bimodal shape [15, 16]. The new analytical theory is developed to account for this effect and to investigate how the DMPK singular value density is modified as a portion of the full transmission matrix is measured and analyzed.

The analytical model assumes that the sample has a confined geometry with well-defined transmission eigenchannels and assumes that a transmission matrix of this sample is constructed by exciting and detecting a portion of the transmission eigenchannels. Limited access to the transmission eigenchannels is included by introducing two new parameters to the DMPK theory. The newly introduced parameters are the ratio m_1 of the number of free modes that are coupled to the sample to the total number of transmission eigenchannels and the ratio m_2 of the number of detectable independent free modes on the detection side to the total number of transmission eigenchannels, as also described in Section 6.5. The analytical model also takes the average transmission through the sample $\langle T \rangle$ as an input parameter.

In order to compare the experimental results with the analytical model, we model the slab geometry sample as a waveguide with area A defined as in Section 6.5 and we use $n_{\text{eff}} = 1.4$ and $l_{\text{tr}} = 0.63$ μm as the sample parameters. $A = (12.1\ \mu\text{m})^2$ is assumed for the thin sample and $A = (20.6\ \mu\text{m})^2$ is assumed for the thick sample.

We calculate m_1 using Eq. 6.2. In the case of dense sampling, some of the incident fields are linear superpositions of others, as inferred by the histograms of $\widetilde{T}_0$ matrix shown in Fig. 6.4. Since we can not directly use the reference $\widetilde{T}_0$ matrix in the analytical model, we use an effective number of independent incident fields $\widetilde{N}_{in}$ instead of N_{in} to find m_1 in the case of dense sampling.[10] For the thin sample $m_1 = 0.27$ and $m_1 = 0.14$ for the cases of dense and sparse sampling respectively. For the thick sample $m_1 = 0.09$ and $m_1 = 0.05$ for the cases of dense and sparse sampling, respectively. In order to calculate m_2, we use Eq. 6.4. For all four cases described above, $m_2 = 0.5$. Finally, $\langle T \rangle$ is calculated using Eq. 6.5 and is found to be $\langle T \rangle = 0.14$ for the thin sample and $\langle T \rangle = 0.06$ for the thick sample.

In Fig. 6.10, the experimental singular value histogram of the thin and the thick sample when the incident fields are densely sampled is shown along with the singular value density obtained from analytical theory. In Fig. 6.10 (a) the analytical singular value density is non-zero between singular values of 0.10 and 2.19 and the experimental singular value histogram has counts starting from the bin centered at the singular value of 0.09. Both curves have a sharp peak; for the analytical singular value density the peak is at a singular value of 0.18, whereas the experimental singular value histogram has a peak between $0.25^{+0.04}_{-0.02}$.

[9] Using a code kindly provided by Arthur Goetschy.

[10] We take $\widetilde{N}_{in}$ equal to the number of singular values of $\widetilde{T}_0$ larger than 0.3, where the value of 0.3 is chosen to avoid the peak at low singular values.

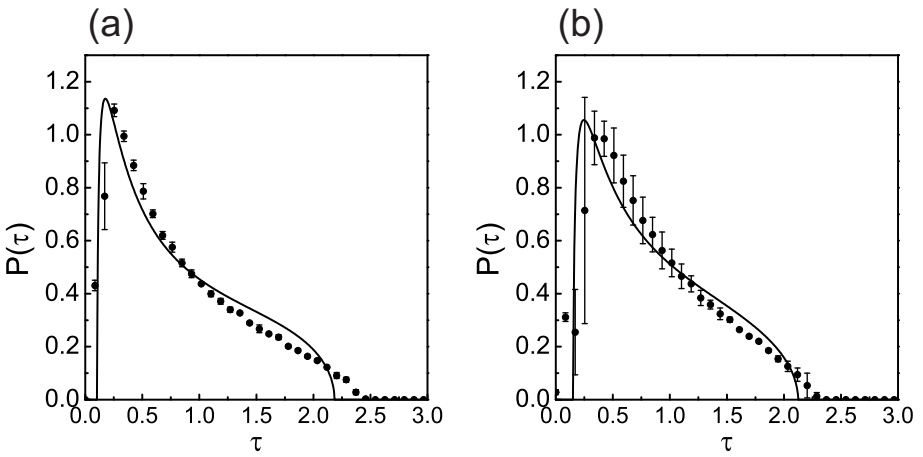

Figure 6.10.: Singular value densities obtained from the analytical model and the experiment for (a) thin (b) thick sample with dense sampling of incident fields (normalization factor=$\sqrt{\langle\tau^2\rangle}$). Black dots: mean, black errorbars: standard deviation of the normalized bin counts in 3 experimental singular value histograms. Solid curve: Histogram obtained from analytical model using $n_{\text{eff}} = 1.4$ and $l_{\text{tr}} = 0.63$ μm, with no adjusted parameters.

Beyond the peak, both histograms decay with a concave shape, the shape of the analytical curve becomes convex at the large singular values and it is sharply cut off at a singular value of 2.19. The experimental histogram, however, has a tail, extending up to the singular value of 2.46. In Fig. 6.10 (b) the experimental singular value histogram is shown along with the results of the analytical theory when the fields incident on the thick ZnO sample are densely sampled. The analytical theory results are similar to those obtained for the thin sample, in line with the prediction from the waveguide model that both samples have about the same number of open transmission eigenchannels. The analytical singular value density function has a peak at the singular value of 0.25, lying at the lower end of the range of plausible peak positions of the experimental histogram. The analytical curve extend between the singular values of 0.14 and 2.13 and the experimental singular value histograms lie between the singular values of 0.04 and 2.30, with the low singular values being attributed to the small overlap between the different incident fields. The agreement between the analytical formula and the experiment is very good for both thin and thick samples, which is remarkable, taking into account the fact that no parameters were adjusted.

In Fig. 6.11, we show the singular value histograms of the thin and the thick sample and the analytical theory curves. In this case, we use the checkerboard sampling to reduce overlap between the incident fields. In Fig. 6.11 (a) both the experimental histogram and the analytical probability density have no counts below a singular value of 0.28 and the positions of the peaks overlap perfectly. The shapes of the two histograms are also in good agreement. In this case, the analytical theory again has a convex shape at large singular values and drops

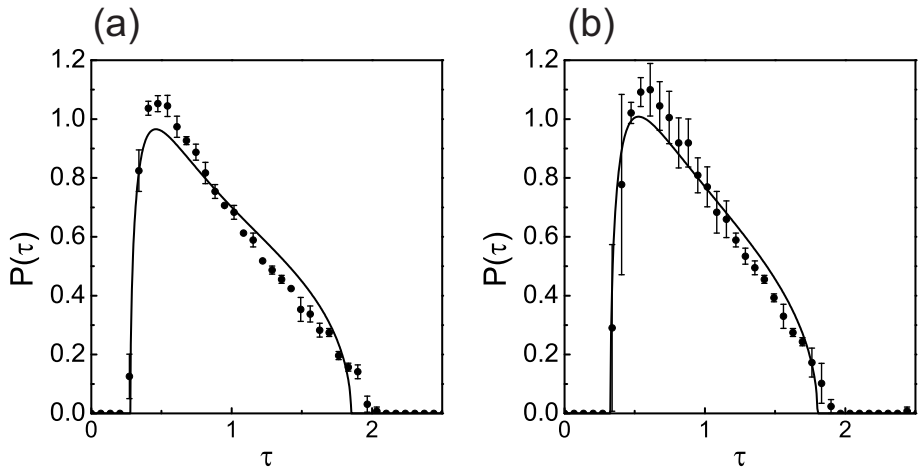

Figure 6.11.: Singular value densities obtained from the analytical model and the experiment for (a) thin (b) thick sample with sparse sampling of incident fields (normalization factor=$\sqrt{\langle \tau^2 \rangle}$). Black dots: mean, black errorbars: standard deviation of the normalized bin counts in 3 experimental singular value histograms. Solid curve: Spectrum obtained from analytical model using $n_{\text{eff}} = 1.4$ and $l_{\text{tr}} = 0.63$ μm, with no adjusted parameters.

sharply to 0 at a singular value of 1.85, whereas the experimental histograms display a linear decrease and extend up to singular value of 2. In Fig. 6.11 (b) the peak of the analytical theory curve is at 0.53, lying within the peak position of the experimental histogram. The cut-off of the analytical formula occurs at the singular value of 0.33 on the low side and at the singular value of 1.81 on the high side; the experimental singular value histograms lie between the singular values of 0.32 and 1.90. The correspondence between the experimental and zero parameter theory is again remarkably good for both samples.

In this section, we compared the experimentally obtained singular value histograms of 11-μm and 31-μm thick samples to the singular value probability density functions predicted by an analytical theory developed by Goetschy and Stone. The comparison is made using the values of the l_{tr} and n_{eff} obtained from independent measurements. The agreement between the analytical and experimental results is remarkable, considering that no parameters were adjusted during the comparison. The good agreement between the analytical theory and the experiment indicates that the samples are well described as ideal lossless waveguides.

6.7. Conclusions

In this chapter, we described our transmission matrix measurements on ZnO nanoparticle layers. Similar samples have been widely used in many experiments until now, including wavefront shaping experiments and transmission matrix ex-

periments [3, 5–8]. We carried out transmission matrix measurements in a regime where correlations are expected to show up and indeed we did observe correlations in the measured transmission matrices.

We applied the numerical model that was also described and used in Chapter 5 to these samples. Using sample parameters that were reported previously, we obtained histograms that are qualitatively similar to the experimental results. By comparing histograms obtained from the numerical model and experiments, a valley of best fit parameters can be found, which agrees well with independent measurements.

A comparison is made with an analytical theory developed for singular value histograms under partial transmission matrix measurements. The agreement between the experimental results and the predictions of the analytical theory is remarkably good.

Our results indicate that layers of ZnO are sufficiently strongly scattering to show mesoscopic correlations and that the transmission matrices retain sample information, which can be retrieved with help of numerical or analytical models.

Bibliography

[1] S. M. Popoff, G. Lerosey, R. Carminati, M. Fink, A. C. Boccara, and S. Gigan, *Measuring the transmission matrix in optics: An approach to the study and control of light propagation in disordered media*, Phys. Rev. Lett. **104**, 100601 (2010). — p.97.

[2] S. Popoff, G. Lerosey, M. Fink, A. C. Boccara, and S. Gigan, *Image transmission through an opaque material*, Nat. Commun. **1**, 1 (2010). — p.97.

[3] Y. Choi, T. D. Yang, C. Fang-Yen, P. Kang, K. J. Lee, R. R. Dasari, M. S. Feld, and W. Choi, *Overcoming the diffraction limit using multiple light scattering in a highly disordered medium*, Phys. Rev. Lett. **107**, 023902 (2011). — p.97, 112.

[4] Y. Choi, M. Kim, C. Yoon, T. D. Yang, K. J. Lee, and W. Choi, *Synthetic aperture microscopy for high resolution imaging through a turbid medium*, Opt. Lett. **36**, 4263 (2011). — p.97.

[5] M. Kim, Y. Choi, C. Yoon, W. Choi, J. Kim, Q.-H. Park, and W. Choi, *Maximal energy transport through disordered media with the implementation of transmission eigenchannels*, Nat. Photon. **6**, 581 (2012). — p.97, 112.

[6] M. D. Birowosuto, S. E. Skipetrov, W. L. Vos, and A. P. Mosk, *Observation of spatial fluctuations of the local density of states in random photonic media*, Phys. Rev. Lett. **105**, 013904 (2010). — p.97, 112.

[7] I. M. Vellekoop and A. P. Mosk, *Universal optimal transmission of light through disordered materials*, Phys. Rev. Lett. **101**, 120601 (2008). — p.97, 112.

[8] I. M. Vellekoop, E. G. van Putten, A. Lagendijk, and A. P. Mosk, *Demixing light paths inside disordered metamaterials*, Opt. Express **16**, 67 (2008). — p.97, 98, 102, 108, 112.

[9] *We have learnt that similar observations have been made in the group of the late Prof. Michael Feld.* — p.97.

[10] A. Goetschy and A. D. Stone, *Filtering random matrices: The effect of imperfect channel control in multiple-scattering*, Phys. Rev. Lett. **111**, 063901 (2013). — p.97, 109.

[11] E. G. van Putten, *Disorder-enhanced imaging with spatially controlled light*, Ph.D. thesis, University of Twente, 2011. — p.98, 102.

[12] I. M. Vellekoop, *Controlling the propagation of light in disordered scattering media*, Ph.D. thesis, University of Twente, 2008. — p.98.

[13] V. A. Marčénko and L. A. Pastur, *Distribution of eigenvalues for some sets of random matrices*, Math. USSR-Sbornik **1**, 457 (1967). — p.102.

[14] W. Press, S. Teukolsky, W. Vetterling, and B. Flannery, *Numerical recipes the art of scientific computing* (Cambridge University Press, 2007). — p.107.

[15] O. N. Dorokhov, *On the coexistence of localized and extended electronic states in the metallic phase*, Solid State Commun. **51**, 381 (1984). — p.109.

[16] P. A. Mello, P. Pereyra, and N. Kumar, *Macroscopic approach to multichannel disordered conductors*, Ann. of Phys. **181**, 290 (1988). — p.109.

CHAPTER 7

Intensity Statistics of Light Transmitted Through Random Photonic ZnO Nanoparticle Media

7.1. Introduction

In this chapter, we describe our measurements on the intensity statistics of light waves transmitted through random photonic media composed of ZnO nanoparticles. Our aim is to observe predicted deviations from Rayleigh statistics in the measured intensity distributions and to retrieve the value of the dimensionless conductance g of the samples.

Statistical methods have been widely employed in the study of wave transport through disordered systems, particularly to study mesoscopic correlations due to interference effects [1–5]. The dimensionless conductance g, which is equal to the number of open transmission eigenchannels is the parameter that is at the center of interest in these studies and is defined in a waveguide geometry as

$$g \approx \frac{N l_{\mathrm{tr}}}{L}, \tag{7.1}$$

with N the total number of transmission eigenchannels that light in the incident free modes can couple to; l_{tr} is the transport mean free path and L is the thickness. In a slab geometry, g is different than given by Eq. 7.1, and can be calculated using an expanding waveguide model [6], in which case g still increases with increasing N and l_{tr}. As g becomes smaller, the mesoscopic effects become more prominent [7–10].

In this chapter, we are interested in the intensity statistics of waves transmitted through random media. We denote the normalized speckle intensity in exit channel a by s_{ab}. The distribution $P(s_{ab})$ of speckle intensity is a Rayleigh distribution when mesoscopic correlations are negligible

$$P(s_{ab}) = \frac{1}{\langle T_{ab} \rangle} e^{(-s_{ab})}. \tag{7.2}$$

Speckle intensity statistics, as studied in this chapter, have a mesoscopic correction proportional to g^{-1}. In case of a large g, the distribution is well-described by Rayleigh statistics [11].

Deviations from Rayleigh statistics have so far been reported in studies conducted in the microwave regime with quasi 1D waveguides [1, 4], and with quasi

2D resonators having randomly distributed conical scatterers [12]. The experiments performed with quasi 1D waveguides are well-explained using the existing mesoscopic transport theories [8, 9], whereas in the experiments performed with quasi 2D resonators, the deviations are reported to be stronger than predicted by mesoscopic theories and are described as freak waves [12]. In a study conducted with visible light using stacks of glass slides, deviations from Rayleigh statistics was observed in the crossover of 1D to quasi-1D regime [13] and in another study conducted with near-infrared light through a 2D system, a deviation from Rayleigh statistics was observed with a g of 0.28 [14]. The only study where deviations from Rayleigh statistics are reported in 3D random photonic samples in the optical regime is the recent study by Strudley *et al.* [5] where a large deviation from Rayleigh statistics is observed in waves transmitted through strongly scattering random photonic GaP nanowire ensembles. The statistics are described by mesoscopic transport theory with a record low g of 3.6.

Until now deviations from Rayleigh statistics have not been reported in the optical regime for 3D, isotropically scattering samples, such as random photonic media composed of ZnO nanoparticles. In Chapter 6, we have reported observations of correlations in the transmission matrices of the same samples, indicating they are strongly scattering. In this chapter, we report an independent confirmation of the strong scattering in ZnO random media, based on speckle intensity statistics. We observe deviations from Rayleigh statistics in the intensity distributions for the first time in an isotropic, three-dimensional, light scattering sample, and model the observed distributions with a mesoscopic theory to retrieve g.

7.2. Experiment

The main elements for an experiment designed to study intensity statistics in waves transmitted through disordered media are a monochromatic light source, high numerical aperture (NA) objectives and a camera. The experiment was performed with minor modifications to the setup that was previously used by Strudley *et al.* [5] to measure the speckle intensity statistics of light transmitted through strongly scattering random photonic GaP nanowire ensembles.

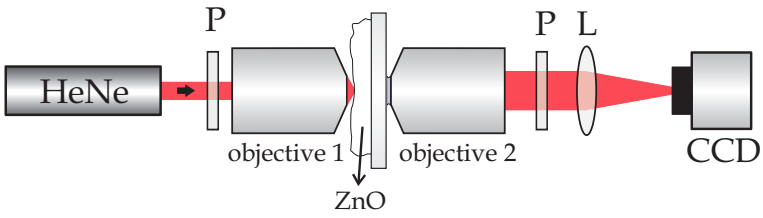

Figure 7.1.: Experimental setup. HeNe: laser. ZnO: sample. Objective 1: 100× 0.9-NA objective. Objective 2: 100× 1.3-NA oil immersion objective. L: 200 mm focal length lens. P: polarizer. CCD: camera sensor.

In Fig. 7.1, we show the experimental setup. Light from a Helium-Neon laser with a wavelength of 632.8 nm and output power of 5 mW is focused on the incident surface of the sample using a 0.9-NA microscope objective. Light transmitted through the sample is collected with a 100× 1.3-NA oil immersion objective, where the ZnO-glass interface is imaged on to the CCD sensor plane using a tube lens with 200 mm focal length. We detect light in a cross-polarized configuration. Both the ZnO sample[1] and the illumination objective are placed on computer-controlled translation stages.

In the experiment, the illumination objective is first placed at the working distance so that a tight focus is created on the sample surface. In this "in-focus" configuration, 1000 images are captured per dataset, moving the sample by 1 μm between the capturing of each image. In this way, the speckle patterns of any two consecutive images are completely uncorrelated. A total number of 6 datasets per sample are recorded for this configuration. Second, the illumination objective is retracted by 25 μm and the measurement is repeated with this "out-of-focus" configuration. The number of transmission eigenchannels that are excited by the incident field is large in the out-of-focus configuration and is small in the in-focus configuration. The measurements made in the out-of-focus configuration serve as reference measurements for the case of large g and negligible mesoscopic corrections, whereas the measurements performed in the in-focus configuration are expected to give rise to a low g configuration, and strong mesoscopic fluctuations.

7.3. Analysis and Results

For each dataset, all captured images are averaged as follows to get an average intensity envelope: An "area of interest" is determined that corresponds to the area inside the full width at half maximum of the average intensity envelope. We get the total transmitted intensity for each sample position (each captured image) by summing the total intensity in the corresponding image. A moving average is calculated by averaging the total transmitted intensity of sample positions within 10 μm. This interval of 10 μm is moved along the sample as the measurement proceeds and each captured image is divided by the moving average to account for fluctuations in the sample's total transmission due to a gradual nonuniformity in the thickness. A constant background is subtracted from all captured images. Finally, each image is cropped to the area of interest and divided pixel by pixel by the average intensity envelope to obtain $s_{ab} = T_{ab}/\langle T_{ab}\rangle$. This procedure also divides out the envelope in the intensity due to diffusion. We collect all of the intensities in the 6 datasets into a single histogram, to obtain $P(s_{ab})$ vs s_{ab}.

Mesoscopic correlations show up most prominently in the high-intensity tail of the distribution. There is an increased probability of observing high-intensity speckles in the case of strong mesoscopic correlations [8, 9].

In Fig. 7.2 we show the $P(s_{ab})$ vs s_{ab} histograms using the data captured in-

[1] We use two separate random photonic samples with thicknesses of 11±1 μm and 31±6 μm, which are the same samples as described in Chapter 6. The samples are referred to as the thin sample and the thick sample, respectively in the rest of this chapter.

focus and out-of-focus for (a) thin and (b) thick sample along with theoretical curves. From the plots, it is seen that the histograms of the data captured in-focus have higher counts at bins corresponding to high intensity speckle, as compared to the data captured out-of-focus. As the out-of-focus data are expected to exhibit Rayleigh statistics, this indicates that the in-focus data shows a deviation from the Rayleigh statistics. In Fig. 7.2, we also show the theoretical speckle intensity distribution for $g = 40$ and $g = \infty$, using the formula in Ref. [8]

$$P(s_{ab}) = e^{-\frac{s_{ab}}{c}} \left\{ 1 + \frac{1}{3g} \left(\left(\frac{s_{ab}}{c} \right)^2 - 4\frac{s_{ab}}{c} + 2 \right) \right\}. \tag{7.3}$$

Ideally, the contrast $c = 1$. The histograms of s_{ab} obtained in the out-of-focus configuration show good agreement with the Rayleigh distribution including a reduced contrast of c=0.95, which is attributed to the finite size of the CCD pixels and to aberrations in the optics. We use the out of focus data as a calibration measurement to fix the instrumental contrast parameter c.

The histogram of s_{ab} obtained in the in-focus configuration show good agreement with the mesoscopic probability density function Eq. 7.3 for $g = 40$ and the fixed value of $c = 0.95$. The value of g can be predicted from the known sample parameters using an expanding waveguide model developed by Scheffold and co-workers [6]. Using the previously measured values l_{tr}=0.7±0.2 μm and n_{eff}=1.4±0.1 [15], along with the estimated illumination spot width of $w =$ 0.45 μm, the expanding waveguide model predicts g between 20 and 48 for both samples. An estimate of the error margins on the parameter g is made by eye by plotting several theory curves with various g values and $c = 0.95$. A reasonable agreement is found between these theory curves and the experimental data for both samples with g in the range between 25 and 80, which agrees well with the prediction of the expanding waveguide model.

For a more precise determination of g we have modeled the experimental data with an analytical expression of the moments of the distribution developed by Kogan *et al.* [9]. We use the following procedure: The moments $\langle s_{ab}^N \rangle / N!$ of s_{ab} are calculated and normalized so that the first moment $\langle s_{ab} \rangle = 1$. The analytical expression is fitted to the first five moments of the data, using the contrast c and the dimensionless conductance g as the free parameters. The contrast obtained from the modeling of the out-of-focus data is used as a fixed parameter during modeling of the first five moments of the in-focus data and only g is a free parameter for this fit.

In Fig. 7.3, we show the moments of the intensity distribution of fields transmitted through the thin and thick samples. In both cases, the moments for the out of focus data decrease monotonously while the in-focus moments appear to decrease more slowly and then rise. The fits to the first 5 moments of the data in the out-of-focus configuration result in $g = \infty$ for both samples.[2] The contrast c is found to be $c = 0.946$ for the thin sample and $c = 0.949$ for the thick sample.

[2]The g values obtained from the fit are on the order of 10^5 with a standard errors on the order of 10^7, indicating that g obtained using this fitting procedure is very large and we can not distinguish between a Rayleigh distribution and the distribution observed in the out-of-focus experimental configuration.

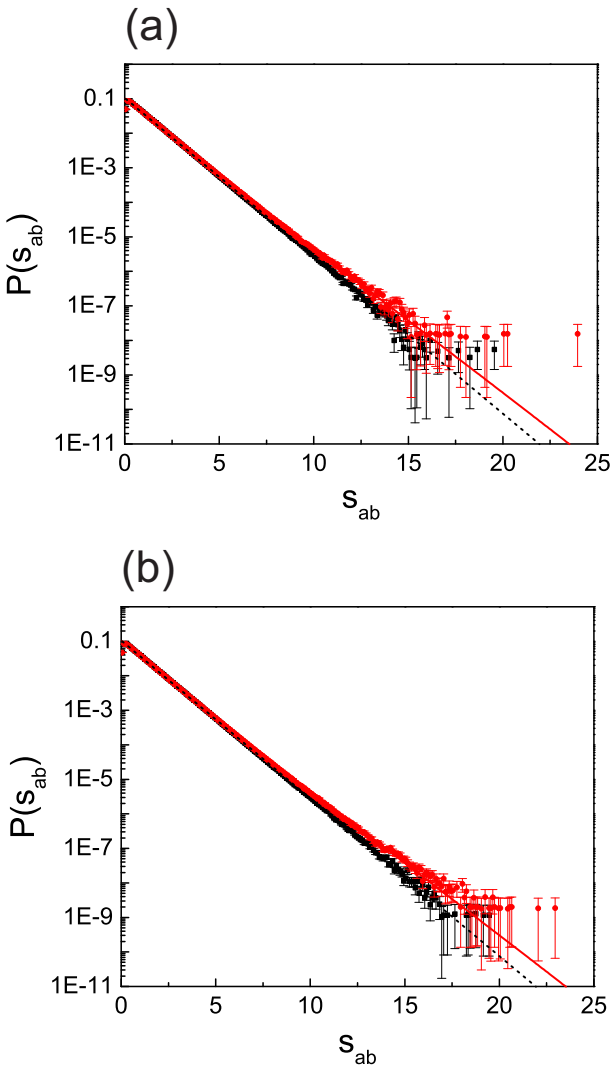

Figure 7.2.: Histogram of intensity distribution, $P(s_{ab})$ of fields transmitted through (a) the thin and (b) the thick sample. Red and black data points: Mean of normalized histograms of six different datasets captured with the in-focus and the out-of-focus configurations, respectively. Errorbars are the standard error of the normalized histograms. Dashed black line: Rayleigh statistics with reduced contrast of 0.95. Solid red line: $P(s_{ab})$ obtained using a mesoscopic theory [8], with g=40 and c=0.95.

It is seen that the fits to out-of focus data are in agreement with the first 10 moments obtained from the experiment. The same procedure repeated for the in-focus configuration results in $g = 35$ for the thin sample and in $g = 57$ for the

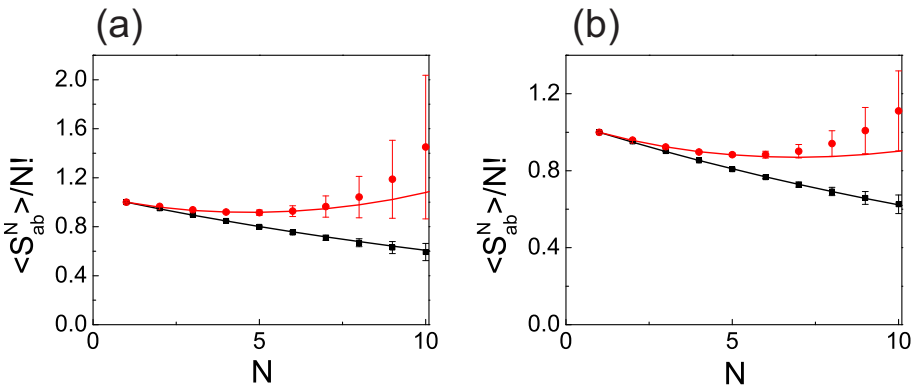

Figure 7.3.: First ten moments of the intensity distributions of fields transmitted through (a) thin and (b) thick sample. Red and black data points: Moments of the intensity distribution obtained from six different datasets measured experimentally with the in-focus and out-of-focus configurations, respectively. Solid black line: First ten moments of the distribution obtained from the mesoscopic theory [9] for (a) $g = \infty$ and $c = 0.946$ and (b) $g = \infty$ and $c = 0.949$. Solid red line: First ten moments of the distribution obtained from the mesoscopic theory [9] for (a) $g = 35.2$ and $c = 0.946$ and (b) $g = 56.7$ and $c = 0.949$, as fitted for the first 5 moments of the distribution.

thick sample, fixing the contrast levels to those obtained from the out-of-focus data. The standard errors obtained from the fits are on the order of 1. For both samples, we find that the direct fits to the theory curves are consistent with the experimental moment analysis. For both samples, a clear deviation between the moments of s_{ab} as captured for the in- and out-of-focus configurations is seen. This shows that the deviations from Rayleigh statistics also cause significant shifts of the moments.

7.4. Conclusions

In this chapter, we have presented speckle intensity statistics of 11±1 μm and 31±6 μm thick layers of ZnO nanoparticles. It was observed that the data collected in an out-of-focus configuration have an intensity distribution that agrees well with a Rayleigh distribution with a reduced contrast. On the other hand, the data collected in a configuration where a tight illumination focus is created on the sample surface display mesoscopic corrections that deviate from Rayleigh statistics. The in-focus intensity histograms agree with mesoscopic theory for a dimensionless conductance g between 25 and 80. Using an analysis of the moments of the distribution we obtain $g = 35$ and $g = 57$ for the 11 μm and 31 μm thick samples, respectively. These values agree well with predictions based on previously reported parameters of similar samples. This is the first observation of strong mesoscopic effects on the speckle intensity statistics of light transmitted

through 3D isotropically scattering samples.

Bibliography

[1] N. Garcia and A. Z. Genack, *Crossover to strong intensity correlation for microwave radiation in random media*, Phys. Rev. Lett. **63**, 1678 (1989). — p.115.

[2] J. F. de Boer, M. C. W. van Rossum, M. P. van Albada, T. M. Nieuwenhuizen, and A. Lagendijk, *Probability distribution of multiple scattered light measured in total transmission*, Phys. Rev. Lett. **73**, 2567 (1994). — p.115.

[3] M. Stoytchev and A. Z. Genack, *Measurement of the probability distribution of total transmission in random waveguides*, Phys. Rev. Lett. **79**, 309 (1997). — p.115.

[4] A. A. Chabanov, M. Stoytchev, and A. Z. Genack, *Statistical signatures of photon localization*, Nature **404**, 850 (2000). — p.115.

[5] T. Strudley, T. Zehender, C. Blejean, E. P. A. M. Bakkers, and O. L. Muskens, *Mesoscopic light transport by very strong collective multiple scattering in nanowire mats*, Nat. Photon. **7**, 413 (2013). — p.115, 116.

[6] F. Scheffold, W. Härtl, G. Maret, and E. Matijević, *Observation of long-range correlations in temporal intensity fluctuations of light*, Phys. Rev. B **56**, 10942 (1997). — p.115, 118.

[7] E. Akkermans and G. Montambaux, *Mesoscopic physics of electrons and photons* (Cambridge University Press, 2007). — p.115.

[8] T. M. Nieuwenhuizen and M. C. W. van Rossum, *Intensity distributions of waves transmitted through a multiple scattering medium*, Phys. Rev. Lett. **74**, 2674 (1995). — p.115, 116, 117, 118, 119.

[9] E. Kogan, M. Kaveh, R. Baumgartner, and R. Berkovits, *Statistics of waves propagating in a random medium*, Phys. Rev. B **48**, 9404 (1993). — p.115, 116, 117, 118, 120.

[10] J. F. de Boer, M. P. van Albada, and A. Lagendijk, *Transmission and intensity correlations in wave-propagation through random-media*, Phys. Rev. B **45**, 658 (1992). — p.115.

[11] J. W. Goodman, *Statistical optics* (Wiley, New York, 2000). — p.115.

[12] R. Höhmann, U. Kuhl, H.-J. Stöckmann, L. Kaplan, and E. J. Heller, *Freak waves in the linear regime: A microwave study*, Phys. Rev. Lett. **104**, 093901 (2010). — p.116.

[13] J. Park, S. Zhang, and A. Z. Genack, *Intensity statistics and photon localization beyond one dimension*, Phys. Rev. E **82**, 045101 (2010). — p.116.

[14] F. Riboli, P. Barthelemy, S. Vignolini, F. Intonti, A. De Rossi, S. Combrie, and D. S. Wiersma, *Anderson localization of near-visible light in two dimensions*, Opt. Lett. **36**, 127 (2011). — p.116.

[15] I. M. Vellekoop, E. G. van Putten, A. Lagendijk, and A. P. Mosk, *Demixing light paths inside disordered metamaterials*, Opt. Express **16**, 67 (2008). — p.118.

CHAPTER 8

Summary

In this thesis, we have described a study on light transport through strongly scattering 3D random photonic media. The main focus of the thesis is on transmission matrix measurements of such random photonic media. We have described our measurements and have interpreted the experimental results using numerical and analytical models based on random matrix theory of light transport. In particular we have studied experimentally the singular value densities of measured transmission matrices.

Ideally, singular values of a transmission matrix give the transmission coefficients of the transmission eigenchannels and have a bimodal density with maxima at singular values of 1 and 0, given by the DMPK theory [1–3]. In an experiment, only part of the transmission matrix can be measured, hence the singular value density is modified. In an extreme case, when very small part of the transmission matrix is measured, the singular value density assumes the shape as predicted by Marcenko-Pastur theory, which gives the singular value density of an uncorrelated random matrix.

The singular value histograms obtained from our measurements show strong deviations from Marcenko-Pastur theory predictions. This indicates that the transmission matrices that we measure have strong correlations. In other words, information on the sample is not lost from the measured transmission matrix.

We have made several very interesting observations regarding the singular values of the measured transmission matrices. First, we have observed that modeling our samples as waveguides with a diameter as the algebraic mean of the width of the probed and detected areas provides an accurate description of slab geometry samples. Second, we conclude that in order to observe correlations, the photonic strength of the sample must be high, besides, effective refractive index and geometry of the sample and experimental design play a very important role. While we observe correlations in the transmission matrices of both random photonic ZnO nanoparticle media and random photonic GaP nanowire ensembles, we observed stronger correlations in the transmission matrices measured with random photonic ZnO nanoparticle media as compared to the random photonic GaP nanowire ensembles. This is well-understood, since even though the GaP nanowire ensembles are reported to have higher photonic strength than the ZnO nanoparticle media, their effective refractive index is high as well, and the sample geometry restricts the experiment to a lower numerical aperture on incident side. Therefore, for studies directed towards observing mesoscopic effects in transmission matrices of 3D samples, samples need to be optimized to have as

high photonic strength as possible along with low effective refractive index and a sample geometry that allows good optical access in an experiment.

We demonstrate how to retrieve the dimensionless scattering strength kl_{tr} from the transmission matrix measurements performed with random photonic GaP nanowire ensembles. The retrieved value of kl_{tr} is in the same range as the values reported previously. This is the first time that optical transmission matrix measurements are applied for retrieving a sample property. We have successfully shown that sample-specific information can be retrieved using transmission matrix measurements and that transmission matrix measurements can provide an alternative way for sample characterization.

Intensity fluctuations are another type of correlations that are indicative of high photonic strength. We have measured the speckle intensity distribution of light transmitted through strongly scattering random photonic ZnO nanoparticle layers and observed deviations from Rayleigh statistics. This is the first observation of such deviations in isotropically scattering 3D random photonic media in the visible regime. The observations are in line with predictions of mesoscopic transport theories [4, 5] and are arising from the high photonic strength of random photonic ZnO nanoparticle media.

Being in a group interested in both understanding and controlling light transport through random photonic media, we carried out a study where we controlled light transport through a random photonic TiO_2 paint layer with wavefront shaping. In this study, we performed wavefront shaping with a binary amplitude modulation method, where we obtain a high intensity at a pre-determined target behind the paint layer by removing the destructively interfering portion of the incident light. The intensity in the target is theoretically limited to a fifth of the intensity that can be obtained using phase modulation methods, however, the binary amplitude modulation method has the advantage of being much faster and easier to implement experimentally.

Bibliography

[1] O. N. Dorokhov, *Transmission coefficient and the localization length of an electron in N bound disordered chains*, JETP Lett. **36**, 318 (1982). — p.123.

[2] O. N. Dorokhov, *On the coexistence of localized and extended electronic states in the metallic phase*, Solid State Commun. **51**, 381 (1984). — p.123.

[3] P. A. Mello, P. Pereyra, and N. Kumar, *Macroscopic approach to multichannel disordered conductors*, Ann. of Phys. **181**, 290 (1988). — p.123.

[4] E. Kogan, M. Kaveh, R. Baumgartner, and R. Berkovits, *Statistics of waves propagating in a random medium*, Phys. Rev. B **48**, 9404 (1993). — p.124.

[5] T. M. Nieuwenhuizen and M. C. W. van Rossum, *Intensity distributions of waves transmitted through a multiple scattering medium*, Phys. Rev. Lett. **74**, 2674 (1995). — p.124.

Nederlandse samenvatting

In dit proefschrift presenteren we een studie over lichttransport door sterk verstrooiende materialen. Licht dat op een dergelijk medium invalt ondergaat vele verstrooiingsgebeurtenissen voordat het weer uit het medium komt. Een groot deel van wat we elke dag om ons heen zien, bijvoorbeeld papier, verf, wolken, rook, huid zijn voorbeelden van verstrooiende media. Op dit moment kijkt u naar een heel mooi voorbeeld van een dergelijke medium, een vel papier. U ziet dat dit papier een mooie witte kleur heeft en helder lijkt, waardoor het aangenaam is om dit proefschrift te lezen. Als u nu probeert door dit papier heen te kijken ziet het er donkerder uit en kunt u niet zien wat er achter zit. In dit eenvoudige experiment zien we twee belangrijke verschijnselen. Ten eerste nemen we waar dat we niet kunnen zien door een meervoudig verstrooiend medium. Na het verlaten van het medium heeft het licht geen gelijkenis met het invallende licht. Ten tweede zien we dat een meervoudig verstrooiend medium meer licht reflecteert dan doorlaat.

De experimenten in dit proefschrift zijn uitgevoerd met een coherente lichtbron, namelijk een laser. Wanneer coherent licht door een verstrooiend medium schijnt, ontstaat er een golffront dat bekend staat als een spikkelpatroon, bestaande uit lichte en donkere vlekken als gevolg van interferentie. Het golffront dat wordt doorgelaten door het sample is heel anders dan het golffront dat invalt op het sample. Het lijkt erop dat er geen relatie is tussen de inkomende en doorgelaten golven maar die is er wel. Als we een identiek golffront op hetzelfde sample sturen is het doorgelaten golffront onveranderd. De relatie tussen de invallende en doorgelaten golven wordt bepaald door de optische transmissie matrix van het sample. Als deze matrix bekend is, dan weet men welke inkomende golf aanleiding geeft tot welke doorgelaten golf. Dan kan men met deze kennis een vooraf ontworpen golf naar het verstrooiende medium sturen, zodat het doorgelaten golffront de gewenste vorm heeft. Voor complexe media zoals wit papier blijkt evenwel dat de transmissie matrix een geweldig groot en ingewikkeld object is.

Volgens de theorie kan men het inkomende golffront zo ontwerpen dat al het licht door het verstrooiende materiaal, bijvoorbeeld dit papier, wordt doorgelaten. Evenzo kan men het golffront zo ontwerpen dat al het licht wordt gereflecteerd. Een willekeurige invallende golf is een superpositie van golven die volledig doorgelaten en golven die volledig gereflecteerd worden door het verstrooiende materiaal. De theorie voorspelt dat het aantal onafhankelijke golven die volledig doorgelaten worden veel kleiner is dan het aantal gereflecteerde golven. Dit leidt ertoe dat de doorgelaten golven superposities zijn van een klein aantal onafhanke-

lijke golven en daardoor zijn gecorreleerd. Men kan deze correlaties onderzoeken door de transmissie matrices van verstrooiende media te meten en bestuderen. Pas onlangs, hebben verschillende groepen metingen van redelijk gemeld grote delen van optische transmissie matrices van verstrooiende media. In de optische transmissie matrix metingen gemeld tot nu toe, zijn dergelijke correlaties niet waargenomen.

Een groot deel van dit proefschrift is gewijd aan het meten en analyseren van optische transmissie matrices van sterk verstrooiende materialen. De bestudeerde samples zijn sterk verstrooiend, wat betekent dat de gemiddelde afstand tussen twee verstrooiingsgebeurtenissen vergelijkbaar is met de golflengte van het licht in het verstrooiende medium. Als de verstrooiing sterker is, dan is het aantal orthogonale golven dat volledig doorgelaten wordt nog kleiner. Dit maakt de doorgelaten golven nog sterker gecorreleerd. Wanneer een voldoende groot deel van de transmissie matrix wordt gemeten, dan zijn deze correlaties zichtbaar te maken in een wiskundige representatie, namelijk het singuliere waarde histogram van de gemeten transmissie matrix. In hoofdstuk 5 en 6 beschrijven we respectievelijk de transmissie matrix metingen van verzamelingen van wanordelijke fotonische GaP nanodraadjes en wanordelijke fotonische ZnO nanodeeltjes. In beide hoofdstukken bestuderen we de singuliere waarde histogrammen van de gemeten matrices en zien dat deze histogrammen afwijken van die van niet-gecorreleerde matrices, wat aangeeft dat de doorgelaten golven gecorreleerd zijn. Bij ons weten is dit voor het allereerst dat zulke correlaties in de transmissie matrix elementen van licht zijn gerapporteerd. In hoofdstuk 5 demonstreren we ook dat we de verstrooiingssterkte van de verzamelingen van wanordelijke fotonische GaP nanodraadjes kunnen bepalen uit de gemeten transmissie matrix.

We beschrijven de experimentele procedure voor de transmissie matrix metingen in detail in hoofdstuk 4. Daar hebben we ook een analyse van de effecten van ruis, veroorzaakt door laserintensiteit fluctuaties, elektrische signalen en zo voort, op de singuliere waarde histogrammen.

In hoofdstuk 7 bestuderen we de intensiteitsschommelingen in het spikkelpatroon dat wordt doorgelaten door verzamelingen van wanordelijke fotonische ZnO nanodeeltjes. We merken op dat het gemeten spikkel intensiteitshistogram overeenstemt met de theorie over mesoscopisch transport en deze overeenstemming bevestigt dat het bestudeerde sample een klein aantal golven volledig doorlaat.

In hoofdstuk 3 beschrijven we een experiment waar we lichttransport door een verstrooiende TiO_2 verflaag controleren met golffrontmodulatie. Golffrontmodulatie is een methode die is ontwikkeld in onze groep en die actieve controle over licht transport door sterk verstrooiende materialen mogelijk maakt zonder initiële kennis van de transmissie matrix van het sample. Het wordt veel gebruikt zowel in onze groep als wereldwijd. In hoofdstuk 3 ontwikkelen we golffrontmodulatie met binaire amplitudemodulatie. Deze methode is gebaseerd op de waarneming dat sommige delen van de invallende golf op een gekozen positie destructief interfereren met de rest, en dus een negatieve bijdrage leveren. Met hulp van een algoritme blokkeren we het deel van de golf dat destructief interfereert met de rest. Daardoor krijgen we een heldere spot achter het verstrooiende sample.

Acknowledgments

Four years ago, I took the major decision to move to Enschede in The Netherlands to pursue a PhD degree. Main reason for starting my PhD in COPS was the type and quality of the research that was carried out here and the enthusiasm of the COPS members for science. I was attracted to the curiosity driven research, and I have not regretted my choice of pursuing my PhD in this group.

During these four years, I have learnt a lot from a scientific point of view and from a professional point of view. I have become an independent researcher. I owe this in particular to my daily supervisor and promotor Allard Mosk and my promotor Willem Vos. Allard, your enthusiasm for science is admirable and contagious. I truly respect the vast amount of knowledge you possess and your willingness to share it. You have a very good command on both theory and experiment and you successfully merge the two worlds. This enables you to easily interpret interesting observations. I will remember our long meetings with pleasure, I learnt a lot from these discussions, in addition they helped me improve my own thinking process as well. Willem, you are a great group leader. I admire how you understand each person individually and create coherence and harmony in the group while maintaining a professional attitude. Thank you for always reminding me to keep the big picture in mind and for helping me develop a critical attitude for my own research as well as research in general.

My development as a researcher took place in a group that is not just a collection of several individuals. We, at COPS, have a very special group spirit that is evolving continuously. I would like to acknowledge all past and present members of COPS and PS groups that created this group spirit: Ad, Allard, Amandev, Bas, Bergin, Bill, Cock, Danang, Diana, Elahe, Elbert, Emre, Femi, Georgios, Hannie, Hasan, Henri, Jacopo, Jin, Jochen, Karen, Kurt, Marcel, Marlon, Marscha, Merel, Mohamed, Nasser, Nilda, Paolo, Patrick, Pepijn, Rajesh, Ramy, Rob, Ronald, Sanli, Sergei, Simon, Sina, Thomas, Timmo, Tom, Vanessa, Willem T., Willem V. and Yonatan. I thank you all for helping me evolve as a researcher and for the good times I had in the group.

I owe a special thanks to the old and new wavefront shapers in the group. In particular, I would like to thank Elbert for teaching me the basics of wavefront shaping, for helping me during my introduction to light transport through disordered media and for the samples and software that I inherited from him. Even though Ivo had already left the group when I started, I would like to thank him for his amazing PhD research which is an inspiration to my own research and for the incredibly useful wavefront shaping software that he left: I am still making use of the ActiveX blocks that he created. I would like to thank Jacopo for being

the first address for most of my questions during the busy times of my PhD, as well as for the witty and sarcastic comments he often made during the coffee times. I also would like to thank Jacopo for reading most of my thesis chapters and providing feedback. I enjoyed supervising Thomas during his bachelor project on wavefront shaping with a MEMS-based projector. You were an excellent student, Thomas. Thanks for your good work and for your contribution to Chapter 3 of my thesis. Bas and Hasan, thank you both for our usual discussions and exchange of ideas and for being my paranimfen. In addition, I would like to thank Pepijn for organizing the Applied Nanophotonics meetings and stimulating discussions between the photonics groups in University of Twente, and for the interest he has shown in my work. Cock, the skillful technician of our group, thank you for all of the technical and recently also chemical advice that you provided. Karen, Marscha and Nilda helped greatly with the administrative matters, thanks for this. Nilda, I have to say I admire your dedication to fixing issues before they even materialize. Finally, I would like to thank Cock, Bas, Allard and Willem for their help during the writing of a proper samenvatting of my thesis.

I would like to thank Ad for his insights about science and scientists and his willingness to share these insights with us. His critical attitude during the presentations and his Survival Guide for Scientists have been inspiring me to give better presentations right from the start of my PhD. I would like to thank Ad as well as all Klaus Boller, Johannes de Boer, Otto Muskens and Hans-Jürgen Stöckmann for accepting to be in my committee and for carefully reading the manuscript of my thesis.

During my PhD, I benefited from collaborations and discussions with colleagues outside of our group as well. The Chapters 5 and 7 are carried out in collaboration with the group of Otto Muskens from University of Southampton. I would like to thank Tom Strudley and Otto Muskens for their contributions. Chapter 5 of my thesis would not have materialized without them kindly providing the random photonic GaP nanowire ensembles. The measurements of transmission matrices of the random photonic GaP nanowire ensembles, which are described in Chapter 5 were taken in University of Twente during the visit of Tom Strudley. The discussions we had during the analysis of the data were also very valuable. For Chapter 7, the measurements were taken and data was analysed during my visit to University of Southampton. I am very happy that we arranged these visits and that we managed to get great results in a short time. I would like to thank you for your scientific contributions and also for the hospitality that you and other colleagues in your group showed during my short visit to your group.

The chapter 6 of my thesis benefited from our communication with Arthur Goetschy and Douglas Stone from Yale University. We made use of the analytical theory they developed to take into account imperfect channel control during the recording of an optical transmission matrix. I would like to thank them for kindly providing the code enabling us to compare our experimental data to their analytical theory and also for the exchange of ideas.

Writing this thesis has required more focusing effort in the last couple of weeks before the deadline. This is due to the distraction caused by large scale Gezi Park public demonstrations that took place in Turkey at the time. I would like

to thank the people of Turkey for raising their voice in their own peaceful and witty style for more democracy. Thank you for giving me hope for the future and for making me proud of the people of my home country.

My old and new friends and Pisotti made life pleasant outside work. Thank you all for the good times in the Netherlands.

I would like to thank my family for their love and support. Anne, baba ve Burcu, hayatım boyunca bana gösterdiğiniz sevgi ve saygı için teşekkür ederim. Her ne kadar bu dört sene boyunca burada olamasanız da manevi desteğinizi esirgemediniz. Bu tezin var olmasında sizin de büyük payınız var. Burcuş, burada seni çok özlüyorum, gelecekte daha sık görüşebiliriz umarım. Kuzen Tuğba, buralarda benimle benzer kaderi paylaşıyorsun, sana da tezinde başarılar diliyorum. Büyükanne ve büyükbabalarıma da sevgileri için çok teşekkür ederim. Anneanne ve dede, sizin sayenizde hayatımın ilk yıllarını hep çok mutlu ve güzel bir şekilde hatırlayacağım. Hepinizi çok seviyorum.

Engin, benimle birlikte Hollanda'ya geldiğin, bu dört sene boyunca hep yanımda olduğun ve bazen saçma bulsan bile bütün sıkıntılarımı sabırla dinlediğin için teşekkür ederim. Özellikle bu tezi yazarken benim için yaptığın fedakarlıklar ve yardımlar çok büyük. Sen olmasaydın bu tez çok daha zor şartlar altında yazılırdı. Şimdi darısı senin başına, seneye senin de güzel bir tezin olacak. Hep yanımda olduğun için teşekkür ederim.

Duygu